ISTANBUL TECHNICAL UNIVERSITY ★ GRADUATE SCHOOL

JEFFERY–HAMEL FLOW OF A SECOND-GRADE BLOOD-BASED TERNARY NANOFLUID IN A POROUS MEDIUM WITH SLIP AND TEMPERATURE JUMP EFFECTS

M.Sc. THESIS

Tunahan GÜNAY

Department of Aeronautics and Astronautics Engineering

Aeronautics and Astronautics Engineering Programme

JUNE 2025

ISTANBUL TECHNICAL UNIVERSITY ★ GRADUATE SCHOOL

JEFFERY–HAMEL FLOW OF A SECOND-GRADE BLOOD-BASED TERNARY NANOFLUID IN A POROUS MEDIUM WITH SLIP AND TEMPERATURE JUMP EFFECTS

M.Sc. THESIS

Tunahan GÜNAY
(511221141)

Department of Aeronautics and Astronautics Engineering

Aeronautics and Astronautics Engineering Programme

Thesis Advisor : Asst. Prof. Dr. Duygu ERDEM

JUNE 2025

İSTANBUL TEKNİK ÜNİVERSİTESİ ★ LİSANSÜSTÜ EĞİTİM ENSTİTÜSÜ

KAYMA VE SICAKLIK SIÇRAMASI ETKİLERİYLE GÖZENEKLİ ORTAMDA İKİNCİ DERECE KAN BAZLI ÜÇLÜ NANOAKIŞKANIN JEFFERY–HAMEL AKIŞI

YÜKSEK LİSANS TEZİ

Tunahan GÜNAY
(511221141)

Uçak ve Uzay Mühendisligi Anabilim Dalı

Uçak ve Uzay Mühendisligi Programı

Tez Danışmanı : Dr. Öğr. Üyesi Duygu ERDEM

HAZİRAN 2025

Tunahan GÜNAY, a M.Sc. student of ITU Graduate School student ID 511221141, successfully defended the thesis entitled "JEFFERY–HAMEL FLOW OF A SECOND-GRADE BLOOD-BASED TERNARY NANOFLUID IN A POROUS MEDIUM WITH SLIP AND TEMPERATURE JUMP EFFECTS", which he prepared after fulfilling the requirements specified in the associated legislations, before the jury whose signatures are below.

Thesis Advisor :	**Asst. Prof. Dr. Duygu ERDEM** Istanbul Technical University	.....
Jury Members :	**Assoc. Prof. Dr. Özge ÖZDEMİR** Istanbul Technical University	.....
	Assoc. Prof. Dr. Gamze GEDİZ İLİŞ Gebze Technical University	.....

Date of Submission : 14 May 2025
Date of Defense : 03 June 2025

To my family and my beloved partner,

FOREWORD

First of all, I would like to thank my advisor, Dr. Duygu ERDEM, for her valuable guidance throughout my master's thesis. Her background in fluid flow problems helped me understand the essential parts of my research and fix the problems that I was facing. I am also highly indebted to her support and patience in times of pressure and difficulties. I also wish to thank Prof. Dr. Ahmet Ziyaettin ŞAHİN, whom I met during my master's studies. He guided me patiently and helped me throughout my studies. His experience and advice motivated me to go further and improve my work. With the assistance of these two valuable professors, I was able to form useful conclusions in my research and move steadily towards my objectives.

I would like to thank my mother, Ayşe GÜNAY, and my father, Şenol GÜNAY, for emotionally and economically supporting me at all times. I love them so much. They made me successful with their love and care, and I got stronger during hard times. In the last seven years, I have had many hard times. But at last, I was successful in very significant things. I also want to thank my brother, Batuhan GÜNAY. He supported me the most during this time and is a very special person to me, and I am truly grateful to him.

Finally, I would like to express my gratitude to my partner for his strong support, understanding, and complete belief in me. Her love and encouragement have made everything feel more meaningful and possible over the last two years. She never left my side, even though we went through a lot together. She has my undying love. I am grateful for everything. You have my love.

June 2025

Tunahan GÜNAY
(Aeronautical Engineer)

TABLE OF CONTENTS

Page

FOREWORD ..... **ix**
TABLE OF CONTENTS ..... **xi**
ABBREVIATIONS ..... **xiii**
SYMBOLS ..... **xv**
LIST OF TABLES ..... **xvii**
LIST OF FIGURES ..... **xix**
SUMMARY ..... **xxiii**
ÖZET ..... **xxvii**
1. INTRODUCTION **1**
1.1 Literature Review 2
1.2 Motivation 11
1.3 Outline of the Thesis 12
2. PARTIAL DIFFERENTIAL EQUATIONS FOR PHYSICAL MODEL **15**
2.1 Partial Differential Equations for Continuity, Momentum, and Energy Equations 16
2.2 Partial Differential Equations for Boundary Conditions 17
2.3 Partial Differential Equations for Engineering Parameters 18
2.4 Thermophysical Properties of TNF 19
3. CONVERSION OF PARTIAL DIFFERENTIAL EQUATIONS **23**
3.1 Conversion of Momentum Equations 24
3.2 Conversion of Energy Equation 26
3.3 Conversion of Boundary Conditions 28
3.4 Conversion of Engineering Parameters 28
4. NUMERICAL SOLUTION AND CODE VALIDATION **29**
4.1 Numerical Method 29
4.2 Code Validation 31
5. RESULTS AND DISCUSSION **35**
5.1 Investigation of Velocity and Temperature Distributions 35
5.2 Investigation of Skin Friction Coefficient and Nusselt Number 56
6. CONCLUSIONS AND RECOMMENDATIONS **63**
REFERENCES **67**
CURRICULUM VITAE **77**

ABBREVIATIONS

BVP	**:** Boundary Value Problem
EG	**:** Ethylene Glycol
HAM	**:** Homotopy Analysis Method
HNF	**:** Hybrid Nanofluid
IVP	**:** Initial Value Problem
MHD	**:** Magnetohydrodynamics
MNF	**:** Mono Nanofluid
MWCNT	**:** Multi-Walled Carbon Nanotube
NF	**:** Nanofluid
ODE	**:** Ordinary Differential Equation
PDE	**:** Partial Differential Equation
SWCNT	**:** Single-Walled Carbon Nanotube
TNF	**:** Ternary Nanofluid

SYMBOLS

B_0 : Magnetic field
C_f : Skin friction coefficient
C_p : Specific heat capacity
$C_{\mathbf{pd}}$: Constant drag coefficient
C_w : Wall-temperature constant
De : Deborah number
$\mathbf{Dr_1}$: Darcy parameter
$\mathbf{Dr_2}$: Inertia parameter
Ec : Eckert number
f : Dimensionless velocity
F_{max} : Centerline rate of movement
g : Dimensionless temperature
Ha : Hartmann number
$\mathbf{J_T}$: Temperature jump coefficient
$\mathbf{j_t}$: Dimensionless temperature jump coefficient
k : Thermal conductivity
$k^*_{\mathbf{thnf}}$: Mean absorption coefficient of TNF
P : Pressure
Pr : Prandtl number
$\mathbf{Pr_e}$: Permeability of the porous medium
$\mathbf{Pr_o}$: Porosity of the porous medium
q_w : Heat flux of the surface
r, θ, **z** : Cylindrical coordinates
Rd : Radiation parameter
Re : Reynolds number
R_1 : Dynamic viscosity ratio
R_2 : Density ratio
R_3 : Heat capacity ratio
R_4 : Thermal conductivity ratio
R_5 : Electrical conductivity ratio
$\mathbf{S_v}$: Slip-velocity coefficient
$\mathbf{s_p}$: Nanoparticle shape parameter
$\mathbf{s_v}$: Dimensionless slip-velocity coefficient
T : Temperature
T : Total
T_w : Temperature at the wall
u : Velocity component
U : Maximum velocity
α : Angle between the wall and centerline

α_1 : Second-grade fluid parameter
η : Dimensionless angle
Φ : Volume fraction of nanoparticle
ρ : Density
μ : Dynamic viscosity
ν : Kinematic viscosity
σ : Electrical conductivity
σ^* : Stefan-Boltzmann constant
τ_w : Shear stress of the surface

LIST OF TABLES

Page

Table 2.1 : Thermophysical properties of Al_2O_3-TiO_2-Ag/blood ternary nanofluid [89-91]. **20**

Table 2.2 : Thermophysical characteristics of Al_2O_3, TiO_2, Ag nanoparticles, and blood (base fluid) [29, 50, 91]..... **20**

Table 2.3 : Shape factor of solid nanoparticles [92]. **21**

Table 4.1 : The $f''(0)$ values obtained in the present study and those reported by Turkyilmazoglu [41], by excluding nanoparticles at various α angles and Reynolds numbers..... **33**

LIST OF FIGURES

Page

Figure 1.1 : Various nanoparticles and base fluids utilized in the production of nanofluids [2]. **2**
Figure 1.2 : The thermal conductivity of Fe_3O_4 nanofluids at various temperatures and volume concentrations [15]. **3**
Figure 1.3 : The enhancement in the thermal conductivity of the nanofluid with different base fluids relative to the pure fluid at various temperatures. [18]. **4**
Figure 1.4 : The ternary nanofluid samples produced at different concentrations [19]. **5**
Figure 1.5 : The graphical abstract of the study [21]. **6**
Figure 1.6 : An outline of the green synthesis method for Ag nanoparticles [25]. .. **7**
Figure 1.7 : The mechanism by which Al_2O_3 nanoparticles interact with and penetrate bacterial membranes [28]. **8**
Figure 1.8 : The physical configuration of nanofluid flow subjected to a magnetic field in converging and diverging channels [35]. **9**
Figure 1.9 : The shear-thinning properties of whole blood at different haematocrit levels and the nearly Newtonian behavior of plasma [52]. **10**
Figure 1.10 : The variation of viscosity with shear rate for various non-Newtonian models [55]. **11**
Figure 1.11 : The physical model of the study [66]. **12**
Figure 2.1 : Nanofluid flow through converging/diverging porous channels under thermal radiation and magnetic media effects. **15**
Figure 4.1 : A comparison of the present $g(\eta)$ values with those reported in the study conducted by Dogonchi and Ganji [72], considering different radiation and stretching/shrinking parameters. **32**
Figure 4.1a : The $g(\eta)$ values for radiation parameters of 0 and 0.3, and for shrinking/stretching parameters of –0.5 and 0.5. ..... **32**
Figure 4.1b : The $g(\eta)$ values for radiation parameters of 0.6 and 1, and for shrinking/stretching parameters of –0.5 and 0.5. ..... **32**
Figure 5.1 : Impact of different channel inclination angles on the velocity distributions under low and high Reynolds number conditions in converging and diverging geometries. **37**
Figure 5.1a : Effect on velocity profile at low Reynolds number. **37**
Figure 5.1b : Effect on velocity profile at high Reynolds number. **37**
Figure 5.2 : Impact of different channel inclination angles on the temperature profiles under low and high Reynolds number conditions in converging and diverging geometries. **38**
Figure 5.2a : Effect on temperature profile at low Reynolds number. **38**
Figure 5.2b : Effect on temperature profile at high Reynolds number. **38**

Figure 5.3 : Impact of Dr_1 parameter on the velocity distributions under low and high Reynolds number conditions in converging and diverging geometries. **39**
Figure 5.3a : Effect on velocity profile at low Reynolds number. **39**
Figure 5.3b : Effect on velocity profile at high Reynolds number. **39**
Figure 5.4 : Impact of Dr_1 parameter on the temperature profiles under low and high Reynolds number conditions in converging and diverging geometries. **41**
Figure 5.4a : Effect on temperature profile at low Reynolds number. **41**
Figure 5.4b : Effect on temperature profile at high Reynolds number. **41**
Figure 5.5 : Impact of Dr_2 parameter on the velocity distributions under low and high Reynolds number conditions in converging and diverging geometries. **42**
Figure 5.5a : Effect on velocity profile at low Reynolds number. **42**
Figure 5.5b : Effect on velocity profile at high Reynolds number. **42**
Figure 5.6 : Impact of Dr_2 parameter on the temperature profiles under low and high Reynolds number conditions in converging and diverging geometries. **44**
Figure 5.6a : Effect on temperature profile at low Reynolds number. **44**
Figure 5.6b : Effect on temperature profile at high Reynolds number. **44**
Figure 5.7 : Impact of Deborah number on the velocity distributions under low and high Reynolds number conditions in converging and diverging geometries. **45**
Figure 5.7a : Effect on velocity profile at low Reynolds number. **45**
Figure 5.7b : Effect on velocity profile at high Reynolds number. **45**
Figure 5.8 : Impact of Deborah number on the temperature profiles under low and high Reynolds number conditions in converging and diverging geometries. **47**
Figure 5.8a : Effect on temperature profile at low Reynolds number. **47**
Figure 5.8b : Effect on temperature profile at high Reynolds number. **47**
Figure 5.9 : Impact of s_v coefficient on the velocity distributions under low and high Reynolds number conditions in converging and diverging geometries. **48**
Figure 5.9a : Effect on velocity profile at low Reynolds number. **48**
Figure 5.9b : Effect on velocity profile at high Reynolds number. **48**
Figure 5.10 : Impact of s_v coefficient on the temperature profiles under low and high Reynolds number conditions in converging and diverging geometries. **49**
Figure 5.10a: Effect on temperature profile at low Reynolds number. **49**
Figure 5.10b: Effect on temperature profile at high Reynolds number. **49**
Figure 5.11 : Impact of s_p on the velocity distributions under low and high Reynolds number conditions in converging and diverging geometries. **50**
Figure 5.11a: Effect on velocity profile at low Reynolds number. **50**
Figure 5.11b: Effect on velocity profile at high Reynolds number. **50**
Figure 5.12 : Impact of s_p on the temperature profiles under low and high Reynolds number conditions in converging and diverging geometries. **52**
Figure 5.12a: Effect on temperature profile at low Reynolds number. **52**
Figure 5.12b: Effect on temperature profile at high Reynolds number. **52**

Figure 5.13 : Impact of Rd parameter on the temperature profiles under low and high Reynolds number conditions in converging and diverging geometries. **53**
Figure 5.13a: Effect on temperature profile at low Reynolds number. **53**
Figure 5.13b: Effect on temperature profile at high Reynolds number. **53**
Figure 5.14 : Impact of Br number on the temperature profiles under low and high Reynolds number conditions in converging and diverging geometries. **54**
Figure 5.14a: Effect on temperature profile at low Reynolds number. **54**
Figure 5.14b: Effect on temperature profile at high Reynolds number. **54**
Figure 5.15 : Impact of j_t coefficient on the temperature profiles under low and high Reynolds number conditions in converging and diverging geometries. **55**
Figure 5.15a: Effect on temperature profile at low Reynolds number. **55**
Figure 5.15b: Effect on temperature profile at high Reynolds number. **55**
Figure 5.16 : Variation in C_f and Nu as functions of Reynolds number with constant parameter settings. **58**
Figure 5.17 : Variation in C_f and Nu as functions of Hartmann number with constant parameter settings. **58**
Figure 5.18 : Variation in C_f and Nu as functions of Dr_1 parameter with constant parameter settings. **59**
Figure 5.19 : Variation in C_f and Nu as functions of Dr_2 parameter with constant parameter settings. **59**
Figure 5.20 : Variation in C_f and Nu as functions of s_v parameter with constant parameter settings. **60**
Figure 5.21 : Variation in C_f and Nu as functions of j_t parameter with constant parameter settings. **60**
Figure 5.22 : Variation in C_f and Nu as functions of s_p with constant parameter settings. **61**
Figure 5.23 : Variation in C_f and Nu as functions of Φ_T with constant parameter settings. **61**

JEFFERY–HAMEL FLOW OF A SECOND-GRADE BLOOD-BASED TERNARY NANOFLUID IN A POROUS MEDIUM WITH SLIP AND TEMPERATURE JUMP EFFECTS

SUMMARY

Ternary hybrid nanofluids (TNFs) have gained growing interest in recent years because of their potential to enhance heat transfer and fluid flow behavior in a wide range of engineering and biomedical applications. In particular, blood-based TNFs with biocompatible nanoparticles (Al_2O_3, TiO_2, and Ag) can be tailored for drug delivery, cancer hyperthermia, and anti-microbial therapy. This study discusses steady, incompressible blood flow with a ternary nanoparticle suspension with the second-grade non-Newtonian model in converging/diverging channels. The second-grade non-Newtonian model has been employed because it is applicable in both small and large vessels. The channels are embedded in a non-Darcy porous medium and are further exposed to a transverse magnetic field. Velocity slip and temperature jump effects at the walls are also considered since such boundary conditions apply to flow in microchannels, biological tissues, or low-friction engineered surfaces. The overall objective of this research is to investigate how the combined impacts of porosity, magnetism, slip-velocity, temperature jump, and the existence of TNFs alter velocity and temperature profiles, as well as significant engineering parameters like skin friction coefficient and Nusselt number. The research aims to contribute to the design of improved biomedical fluid therapies and engineered channels for optimized heat and momentum transfer.

Two rigid plates are symmetrically inclined about a centerline, which creates a channel of half-opening angle (α) that can either be converging or diverging. The channels are placed in the porous medium in this study. The base fluid, blood, which is a second-grade non-Newtonian fluid, is used to examine the viscoelastic behavior of the fluid. The blood is blended with Al_2O_3, TiO_2, and Ag nanoparticles to form a TNF with superior thermophysical properties. An external magnetic field is implemented crosswise to the direction of flow, creating MHD conditions for effective control of the flow and accurate placement of the nanoparticles. Also, the different dimensionless parameters such as the Reynolds number (Re), Hartmann number (Ha), the Darcy (Dr_1) parameter, Forchheimer (Dr_2) parameter, and the Deborah number (De) represent the influence of inertial, magnetic, porous, and elastic effects, as well as the mechanisms governing the flow regime under varying operating conditions.

Slip-velocity is included through a coefficient S_v, enabling partial fluid slip on walls. Temperature jump is regulated through a coefficient J_T, enabling discontinuity in near-wall temperature gradients, particularly useful in applications involving engineered surfaces. Heat radiation is included through the Rosseland approximation, which is applicable for high-temperature or radiative situations, where targeted cell killing is facilitated by local heating. Governing equations include continuity,

momentum, and energy equations. Momentum equations include second-grade fluid elasticity (via α_1), Darcy–Forchheimer coefficients, and a magnetic term for MHD. Energy transport accounts for viscous dissipation, radiative heat transfer, and magnetic media, with the thermal conductivity accounting for nanoparticles' shape factors. Dynamic viscosity is greater than in clean blood because there are nanoparticles and second-grade elasticity. Further, particle shape factors ranging from spherical to blade can greatly affect gross heat transfer performance by changing conductivity routes.

A similarity transformation reduces the obtained partial differential equations to coupled ordinary differential equations in dimensionless form, with boundary conditions handling both centerline and channel walls (slip/jump conditions). MATLAB's bvp4c solver, which uses a finite difference collocation scheme, is used to obtain velocity and temperature profiles. Initial guesses are based on limited scenarios, and convergence tests ensure that mesh refinement does not alter the results. Validation comparisons with popular established Jeffrey–Hamel flow and porous-flow benchmarks confirm the accuracy and reliability of the numerical process, allowing for extensive parametric studies for possible applications in optimized drug delivery, cancer hyperthermia, or enhanced thermal management in miniature fluidic devices.

Our parametric study revealed that at very low Reynolds numbers (Re = 1), diverging and converging channels exhibit nearly identical velocity profiles with slight acceleration when the channel half-angle is raised. Diverging channels exhibit a more detailed velocity profile as Re is raised to 50 for large Darcy and Forchheimer values, whereas converging channels have reduced flow due to the increased porous-medium drag. Non-Newtonian flow caused by the Deborah number creates small but noticeable changes in both temperature and velocity, especially for high Re. Temperature profiles also rely quite strongly on Re, with low-Re flows creating much larger thermal values and hiding geometrical differences between converging and diverging shapes. Larger Darcy or Forchheimer parameters in diverging channels raise temperatures due to increased dissipation, but the influence is the reverse in converging channels. Increased slip coefficients decrease wall shear but can increase or decrease peak temperatures depending on Re, and a high-temperature jump coefficient creates more rapidly rising thermal gradients, which enhance heat transfer. The nanoparticle shape factor has little effect on velocity but a considerable effect on temperature, with increased shape factors contributing greater thermal conductivity. Simultaneously, radiation parameters reduce overall temperatures through losses, and the Brinkman number rises due to increased dissipation-related heating. Simultaneously, increased magnetic fields and nanoparticle volume fractions increase wall shear and heat transfer, which indicates a potential method of flow and thermal control in convergent/divergent channels.

Our computational study shows that Forchheimer and Darcy parameters do not greatly change velocity and temperature fields in converging and diverging channels: higher values improve the flow rate and raise the temperature in diverging channels, but induce an opposite trend in converging channels. Relatively small second-grade (non-Newtonian) effects provide several percent divergence from velocity profiles for low to high Reynolds numbers, therefore demonstrating fluid elasticity effects for both geometries. Slip-velocity boundary conditions reduce skin friction significantly, whereas wall temperature jumps enhance heat transfer significantly by improving the local thermal gradient. The particle geometry has a major influence on temperature but not on velocity; the thermal conductivity increases with increasing shape factors.

The rise in the magnetic field increases wall friction and heat transfer, providing a basic method of controlling fluid flow and temperature profiles. These results highlight globally the need to consider, at the same time, porous media properties, elasticity of non-Newtonian fluid, slip/jump boundaries, and nanoparticle properties to maximize thermal and hydrodynamic performance in convergent/divergent channels.

KAYMA VE SICAKLIK SIÇRAMASI ETKİLERİYLE GÖZENEKLİ ORTAMDA İKİNCİ DERECE KAN BAZLI ÜÇLÜ NANOAKIŞKANIN JEFFERY–HAMEL AKIŞI

ÖZET

Üçlü hybrid nanoakışkanlar (TNF'ler), mühendislik ve biyomedikal uygulamalarda ısı transferi ve akış davranışını iyileştirme potansiyelleri nedeniyle son yıllarda artan ilgi görmektedir. Özellikle, biyouyumlu nanoparçacıklar (Al_2O_3, TiO_2 ve Ag) içeren kan bazlı TNF'ler, ilaç taşınımı, kanser hipertermisi ve antimikrobiyal tedavi için uyarlanabilir. Bu çalışma, yakınsayan/ıraksayan kanallarda ikinci dereceden Newtonyen olmayan model ile üçlü nanoparçacık içeren, kararlı, sıkıştırılamaz kan akışını ele almaktadır. İkinci dereceden Newtonyen olmayan model, hem küçük hem de büyük damarlarda uygulanabilir olduğu için kullanılmıştır. Kanallar, Darcy olmayan gözenekli ortama gömülüdür ve enine manyetik alana maruz bırakılmıştır. Mikrokanallardaki, biyolojik dokulardaki veya düşük sürtünmeli mühendislik yüzeylerindeki akış için geçerli olduğundan, duvarlardaki hız kayması ve sıcaklık sıçraması etkileri de dikkate alınmıştır. Bu çalışmanın temel amacı, gözeneklilik, manyetizma, kayma hızı, sıcaklık sıçraması ve TNF'lerin varlığının birleşik etkilerinin hız ve sıcaklık profillerini ve ayrıca cidar sürtünme katsayısı ile Nusselt sayısı gibi önemli mühendislik parametrelerini nasıl değiştirdiğini incelemektir. Araştırma, optimize edilmiş ısı ve momentum transferi için geliştirilmiş biyomedikal akış terapileri ve mühendislik kanallarının tasarımına katkı sağlamayı hedeflemektedir.

İki rijit plaka, bir merkez çizgisi etrafında simetrik olarak eğimlidir ve bu da yakınsayan veya ıraksayan olabilen yarı açılı (α) bir kanal oluşturur. Kanallar bu çalışmada gözenekli ortama yerleştirilmiştir. Newtonyen olmayan ikinci dereceden bir akışkan modeli, akışkanın (kan) viskoelastik davranışını incelemek için kullanılmıştır. Kan, üstün termofiziksel özelliklere sahip bir TNF oluşturmak için Al_2O_3, TiO_2 ve Ag nanoparçacıkları ile karıştırılmıştır. Akış yönüne dik olarak uygulanan harici manyetik alan, akışın etkili kontrolü ve nanoparçacıkların hassas yerleşimi için MHD koşulları oluşturur. Ayrıca, Reynolds sayısı (Re), Hartmann sayısı (Ha), Darcy (Dr_1) parametresi, Forchheimer (Dr_2) parametresi ve Deborah sayısı (De) gibi boyutsuz parametreler, atalet, manyetik, gözenekli ve elastik etkilerin yanı sıra değişen çalışma koşulları altında akış rejimini yöneten mekanizmaları temsil eder.

Kayma hızı, S_v katsayısı ile dahil edilerek duvarlarda kısmi akış kaymasına izin verilir. Sıcaklık sıçraması, J_T katsayısı ile düzenlenir ve özellikle mühendislik yüzeylerini içeren uygulamalarda duvar yakınındaki sıcaklık gradyanlarında süreksizliğe olanak tanır. Isı radyasyonu, yüksek sıcaklık veya radyatif durumlar için uygun olan ve lokal ısıtma ile hedeflenen hücre öldürmenin sağlandığı belirli biyomedikal uygulamalarda geçerliliğini koruyan Rosseland yaklaşımı ile dahil edilmiştir. Yönetim denklemleri arasında süreklilik, momentum ve enerji denklemleri bulunur. Momentum denklemleri, ikinci dereceden akışkan elastikiyetini (α_1), Darcy–Forchheimer katsayılarını ve

MHD için manyetik bir terimi içerir. Enerji denklemi, viskoz dissipasyon, radyatif ısı transferi ve manyetik ortamı hesaba katar ve termal iletkenlik nanoparçacıkların şekil faktörlerini içerir. Dinamik viskozite, saf kandan daha yüksektir çünkü nanoparçacıklar mevcuttur. Ayrıca, küreselden bıçak şekline kadar değişen parçacık şekil faktörleri, iletkenlik yollarını değiştirerek toplam ısı transfer performansını önemli ölçüde etkileyebilir.

Bir benzerlik dönüşümü, elde edilen kısmi diferansiyel denklemleri boyutsuz formda birleştirilmiş adi diferansiyel denklemlere indirger ve sınır koşulları hem merkez çizgisini hem de kanal duvarlarını (kayma/sıçrama koşulları) ele alır. Fiziksel parametrelerin etkisini incelemek amacıyla elde edilen adi diferansiyel denklemler, Re ve Ha sayıları gibi boyutsuz sayılara bağlı olarak ifade edilir. Ayrıca, nanoparçacıkların akış üzerindeki etkilerini gözlemleyebilmek için boyutsuz sayılar baz akışkana, yani kana göre tanımlanır. Adi diferansiyel denklemler baz akışkana göre yazıldığında, denklemde nanoakışkan ile baz akışkan arasındaki ilişkiyi gösteren oranlar ortaya çıkar. Bu oranlar, tablolarda verilen korelasyonlar aracılığıyla hesaplanır. Aynı işlem sınır koşulları için de geçerlidir. Hız ve sıcaklık profillerini elde etmek için, sonlu fark kolokasyon şeması kullanan MATLAB'ın bvp4c çözücüsü kullanılmıştır. Başlangıç tahminleri sınırlı senaryolara dayanır ve yakınsama testleri, ağ iyileştirmesinin sonuçları değiştirmediğini garanti eder. Yaygın olarak kabul görmüş Jeffrey–Hamel akışı ve gözenekli akış kıyaslamaları ile doğrulama karşılaştırmaları, sayısal sürecin doğruluğunu ve güvenilirliğini teyit eder ve optimize ilaç taşınımı, kanser hipertermisi veya minyatür akışkan cihazlarda gelişmiş termal yönetim için kapsamlı parametrik çalışmalara olanak tanır.

Farklı fiziksel parametrelerin etkileri incelenirken, öncelikle bazı sabit referans değerler belirlenmiştir. Mühendislik parametreleri, hız ve sıcaklık dağılımları analiz edilirken, incelenen parametre farklı değerlerde ele alınmış, diğer tüm fiziksel parametreler sabit tutulmuştur. Fiziksel parametrelerin cidar sürtünme katsayısı ve Nusselt sayısı üzerindeki etkisini detaylı analiz edebilmek için parametreler daha geniş bir aralıkta incelenmiştir. Parametrik çalışmamız, çok düşük Reynolds sayılarında (Re = 1), ıraksayan ve yakınsayan kanalların, kanal yarı açısı arttıkça hafif bir hızlanma ile neredeyse özdeş hız profilleri sergilediğini ortaya koymuştur. Büyük Darcy ve Forchheimer değerleri için Re 50'ye yükseltildiğinde, ıraksayan kanallar daha detaylı bir hız profili sergilerken, yakınsayan kanallarda gözenekli ortam sürtünmesinin artması nedeniyle akış azalır. Düşük Reynolds sayılarında, daralan ve genişleyen kanallarda benzer hız profillerinin elde edilmesinin nedeni, bu kanal tiplerinin karakteristik etkilerini düşük Reynolds sayılarında yeterince gösterememeleridir. Ancak Reynolds sayısı arttıkça, kanallar kendi karakteristik özelliklerini daha belirgin bir şekilde göstermeye başlar ve bu nedenle iki kanal tipi için farklı hız ve sıcaklık profilleri elde edilir. Deborah sayısından kaynaklanan Newtonyen olmayan akış etkisi, özellikle düşük Reynolds sayılarında hem sıcaklık hem de hız dağılımlarında küçük ancak belirgin değişikliklere neden olmaktadır. Düşük Reynolds sayısında, Deborah sayısının etkisi sıcaklık değerlerinde maksimum %9'luk bir sapmaya yol açarken, yüksek Reynolds sayısında bu sapma yalnızca %0.5 düzeyindedir. Bu sonuçlara göre, daralan ve genişleyen kanal akışlarında yüksek Reynolds sayılarında Newtonyen akışkan yaklaşımının kullanılması uygun kabul edilebilir. Ancak, düşük Reynolds sayılarında Newtonyen yaklaşımın tercih edilmesi ciddi hatalara neden olabilir. Bu nedenle, söz konusu Reynolds sayılarında farklı Newtonyen olmayan

akışkan modellerinin kullanılması gerekmektedir. Sıcaklık profilleri de Re'ye oldukça bağlıdır ve düşük-Re akışları, yakınsayan ve ıraksayan şekiller arasındaki geometrik farklılıkları gizleyerek çok daha yüksek termal değerler oluşturur. Iraksayan kanallarda artan Darcy veya Forchheimer parametreleri, artan dissipasyon nedeniyle sıcaklıkları yükseltir, ancak etki yakınsayan kanallarda tersinedir. Duvardaki kayma durumu akışkanın akmasına karşı olan direnci kırar ve akışkanın duvara yakın bölgede daha rahat akmasını sağlar. Kayma olmayan sınır şartı altında, duvarda akma gerçekleşmediği için akışa karşı daha fazla direnç oluşur. Bu nedenle, en yüksek cidar sürtünmesi bu durumda meydana gelir. Artan kayma katsayıları, duvar kayma gerilimini azaltır ancak Re'ye bağlı olarak pik sıcaklıkları artırabilir veya azaltabilir ve yüksek sıcaklık sıçrama katsayısı, ısı transferini artıran daha hızlı yükselen termal gradyanlar oluşturur. Nanoparçacık geometrisinin ısı iletkenliği üzerinde yüksek bir etkisi olduğu için, sıcaklık dağılımı üzerindeki etkisi 5 farklı geometri ile incelendi. Ek olarak, nanoparçacık geometrisi, momentum denklemi içinde yer alan manyetik terimdeki elektrik iletkenliğiyle ilişkilidir. Bu nedenle, nanoparçacık geometrisinin hız dağılımı üzerindeki etkisi de incelendi. Farklı geometriler için farklı şekil faktörleri kullanıldı. Nanoparçacık şekil faktörünün hız üzerinde küçük ancak sıcaklık üzerinde önemli bir etkisi vardır; artan şekil faktörleri daha yüksek termal iletkenliğe katkıda bulunur. Nanoparçacık alanının (veya hacim oranının) artması, ısıl iletkenliği ve dinamik viskoziteyi artırır. Bu artışa bağlı olarak, cidar sürtünme katsayısı ile daralan ve genişleyen kanallarda gerçekleşen ısı transferi de artar. Aynı zamanda, radyasyon parametreleri kayıplar yoluyla toplam sıcaklıkları düşürür ve Brinkman sayısı, dissipasyon kaynaklı ısınmanın artması nedeniyle sıcaklığı yükseltir. Eşzamanlı olarak, artan manyetik alanlar ve nanoparçacık hacim oranları, duvar kayma gerilimini ve ısı transferini artırır, bu da yakınsak/ıraksak kanallarda akış ve termal kontrol için potansiyel bir yöntem olduğunu gösterir.

Hesaplamalı çalışmamız, Forchheimer ve Darcy parametrelerinin yakınsayan ve ıraksayan kanallardaki hız ve sıcaklık alanlarını büyük ölçüde değiştirmediğini göstermiştir: daha yüksek değerler, ıraksayan kanallarda akış hızını ve sıcaklığı artırır, ancak yakınsayan kanallarda tersi bir eğilim oluşturur. Nispeten küçük ikinci dereceden (Newtonyen olmayan) etkiler, düşükten yüksek Reynolds sayılarına kadar hız profillerinde birkaç yüzdelik sapma sağlar, bu nedenle her iki geometri için akışkan elastikiyet etkilerini gösterir. Kayma hızı sınır koşulları, cidar sürtünme katsayısını önemli ölçüde azaltırken, duvar sıcaklık sıçraması yerel termal gradyanı iyileştirerek ısı transferini önemli ölçüde artırır. Parçacık geometrisi, sıcaklık üzerinde büyük bir etkiye sahiptir ancak hız üzerinde etkisi yoktur; termal iletkenlik, şekil faktörleri arttıkça yükselir. Manyetik alandaki artış, duvar sürtünmesini ve ısı transferini artırarak akışkan akışı ve sıcaklık profillerinin kontrolü için temel bir yöntem sunar. Bu sonuçlar, yakınsak/ıraksak kanallarda termal ve hidrodinamik performansı maksimize etmek için aynı anda gözenekli ortam özelliklerinin, Newtonyen olmayan akışkanın elastikiyetinin, kayma/sıçrama sınırlarının ve nanoparçacık özelliklerinin dikkate alınması gerektiğini vurgulamaktadır.

1. INTRODUCTION

Thermophysical properties of liquids play a major role in optimizing system efficiency in various industrial and engineering systems, such as thermal engineering, biomedical engineering, drug delivery, and so on. The majority of the traditional fluids do not have sufficient thermal conductivity, specific heat, and other thermal properties necessary to support high heat transfer rates of such processes. Several approaches have been pursued to optimize these properties over time. Either by changing flow conditions or by increasing the fluid thermal conductivity, passive heat transfer augmentation is feasible. The concept of nanofluids was first introduced by Choi and Eastman [1], demonstrating that the suspension of particles (smaller than 100 nm in diameter) in base fluids like water, oils, or EG with or without additives was capable of dramatically altering thermal properties. They demonstrated that the suspension of 1-5% volume concentration of solid oxide particles could increase thermal conductivity by a maximum of 20%. Bacha et al. [2] have prepared a comprehensive review on nanofluids, covering their synthesis and applications. Figure 1.1 shows some of the nanoparticles and base fluids used in nanofluid production. In nanofluid flow research, two main models are commonly used: These are the single-phase models [3–5], in which the nanoparticle-fluid mixture is considered as a homogenous medium with uniform properties, and the two-phase models [6–8], in which nanoparticles and the base fluid are treated separately with regard to their different interactions. A comparative study published by Bianco et al. [9] examined laminar flow in water-based Al_2O_3 nanofluids, working under constant heat flux conditions using both approaches. Differences were notable, especially at higher nanoparticle concentrations (e.g., 11% volume fraction) between the findings of the two models. Also, Göktepe et al. [10] showed differences regarding convective heat transfer in a heated tube with nanofluids. Nanofluids are used for different applications with these models [11–13].

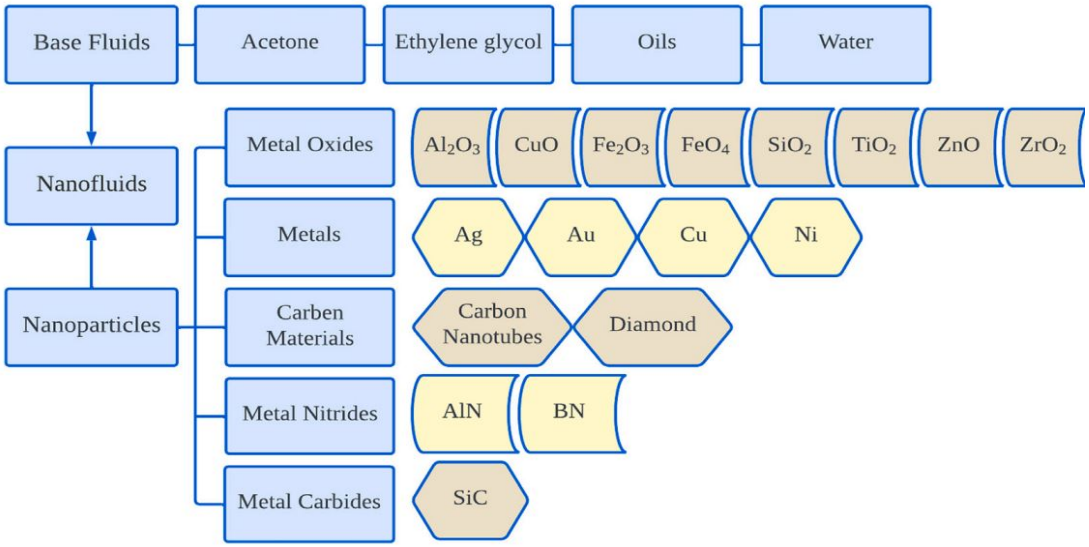


Figure 1.1 : Various nanoparticles and base fluids utilized in the production of nanofluids [2].

1.1 Literature Review

Drawing on the pioneering research of Choi and Eastman [1], the recent two decades have witnessed enormous research on mono-nanofluids (MNFs) and hybrid nanofluids (HNFs) with particular focus on nanoparticle variations and levels of concentration that influence their properties. Liu et al. [14] applied the chemical reduction method to produce water-based Cu NF without surfactant at volume concentrations below 0.2%. According to their findings, the utilization of Cu nanoparticles with 0.1% volume concentration improved the thermal conductivity by 23.8% compared to pure water. In another subsequent study, Syam Sundar et al. [15] used the Fe_3O_4 nanoparticles, which are synthesized with the usage of the chemical precipitation method, to produce distilled water-based NF at various volume concentrations ranging from 0 to 2% and different temperatures ranging from 20 to 60 °C. Maxwell and Einstein models were also implemented to predict the thermal conductivity and viscosity of NF. Figure 1.2 shows the thermal conductivity of Fe_3O_4 nanofluids at various temperatures and volume concentrations. They found that improvement in the thermal conductivity was 48% relative to distilled water at 2% concentration and 60 °C temperature, and the outcomes of the experiment are fairly well-aligned with the given models. Kakavandi and Akbari [16] investigated the thermal conductivity and stability of MWCNTs-SiC HNF using binary base fluids with different concentrations in the range of 0.05–0.75% and various temperatures ranging from 25 to 50 °C. They observed that thermal conductivity improved with increasing nanoparticle volume fraction. Leong et al. [17]

comprehensively reviewed the synthesis, thermal conductivity property, and stability problems of HNFs. In a recent study, Nazir et al. [18] employed the thermal plasma technique to prepare ZnO-MgO HNF by using various base fluids (coconut oil, engine oil, distilled water, and pristine coolant). Figure 1.3 shows the increase in thermal conductivity compared to the pure fluid at different temperature values and for different base fluids. The maximum improvement in the thermal conductivity, ranging from 9.2 to 19.04% was observed with the utilization of pristine coolant base fluid at temperatures in the range of 20-60 °C.

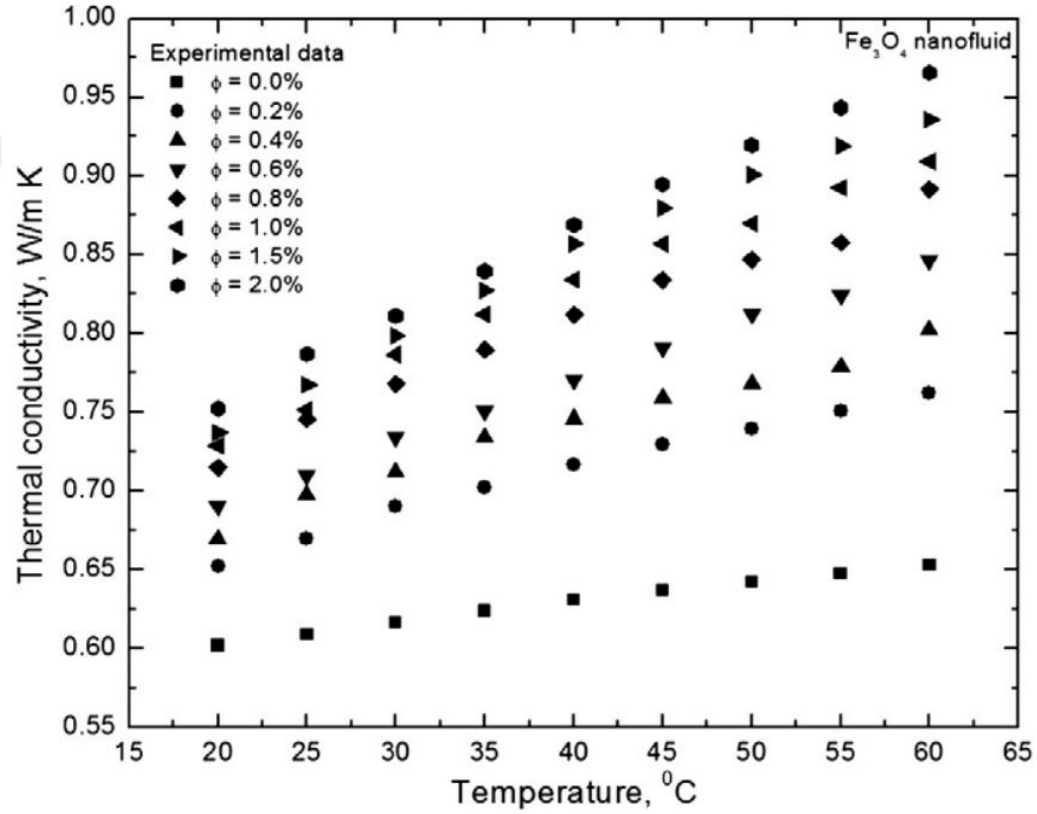


Figure 1.2 : The thermal conductivity of Fe_3O_4 nanofluids at various temperatures and volume concentrations [15].

A very recent area of research emerged in the last five years on a synergistic blending of different nanoparticles in creating high-performance nanofluids. Specifically, the use of three distinct nanoparticles to create hybrid nanofluids has gained attention. These are often referred to as ternary nanofluids (TNFs). Compared to mono and binary nanofluids, TNFs can demonstrate superior thermophysical characteristics due to the synergistic interactions between the different nanoparticles. Boroomandpour et al. [19] investigated the thermal conductivity of TNF created by dispersing MWCNTs, TiO_2, and SiO_2 nanoparticles in a water-EG solution (80:20), and compared these results with

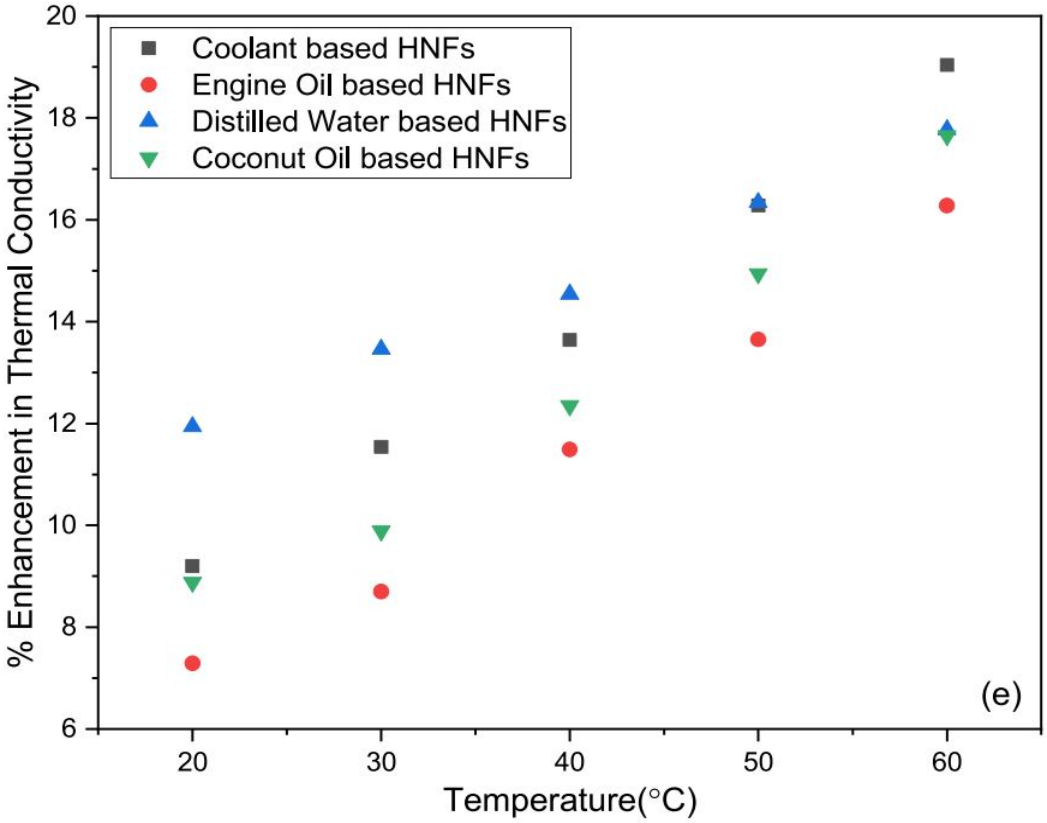


Figure 1.3 : The enhancement in the thermal conductivity of the nanofluid with different base fluids relative to the pure fluid at various temperatures. [18].

those of binary and mono nanofluids. Figure 1.4 presents ternary nanofluid samples prepared with varying concentrations. Adun et al. [20] experimentally researched the thermal conductivity and viscosity of Al_2O_3-ZnO-Fe_3O_4 TNF using three different mixture ratios (1:1:1, 1:2:1, and 1:1:2) and various volume fractions ranging from 0.5% to 1.25% with a step of 0.25%. The maximum enhancement of 36.018% in thermal conductivity was obtained with a 1:1:1 mixture ratio at 1.25% fraction and 65 °C. In a new study, Mousavi et al. [21] examined the thermal and rheological characteristics of CuO-$CaCO_3$-SiO_2/water HNF at various temperatures ranging from 15 °C to 60 °C and various volume fractions ranging from 0.1 vol% to 0.5 vol%. Figure 1.5 provides a summary of the study. A maximum improvement of 78.6% was observed for a 60:30:10 volume mixing ratio at 0.5 vol% and 15 °C.

Emerging as a transforming invention in modern medical science, blood-based nanofluids show amazing promise in a variety of therapeutic and diagnostic uses. Made from nanoparticles in blood plasma or other biological fluids, these advanced fluids are changing oncology, haematology, and infectious disease control treatments. By means of various therapeutic uses, especially when injected via nanoparticles, blood-based

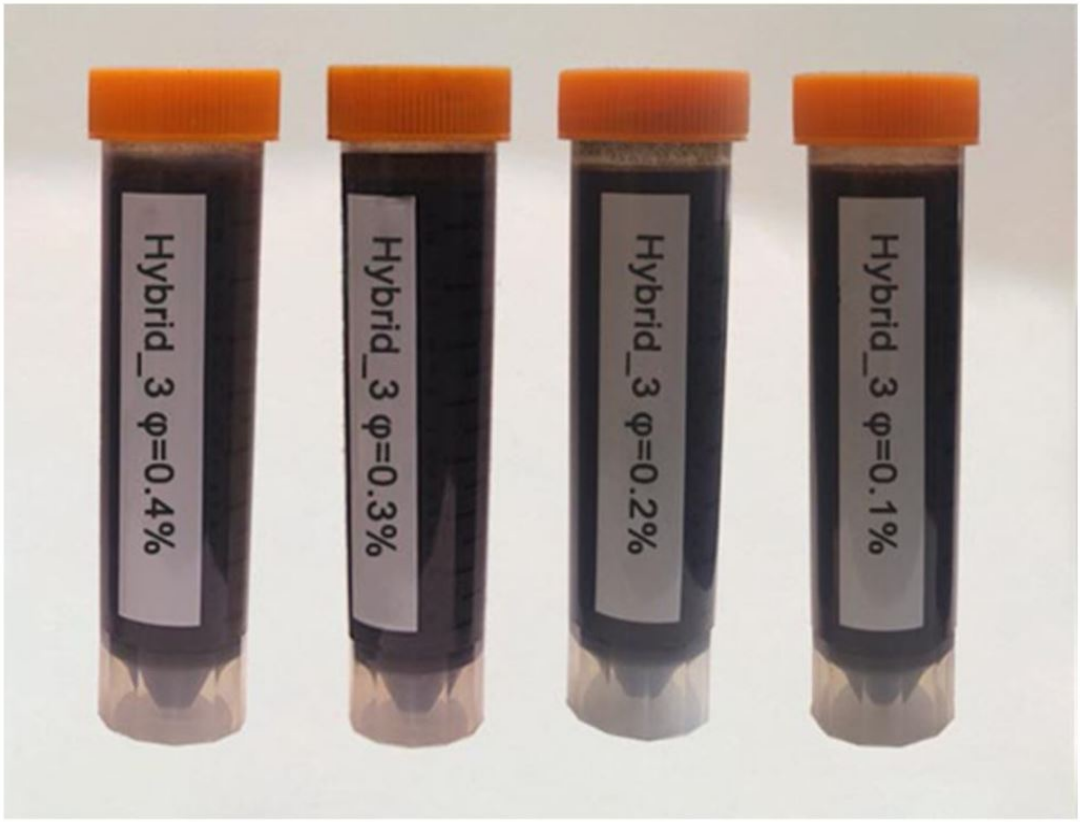


Figure 1.4 : The ternary nanofluid samples produced at different concentrations [19].

nanofluids are transforming contemporary medical practice [22]. In hyperthermia cancer therapy, anaemia treatment, tissue diagnostics, surgical applications, and antimicrobial interventions, these advanced formulations show amazing efficacy [22–24]. Among the most exciting nanoparticles, TiO_2, Al_2O_3, and Ag stand out for their remarkable physicochemical qualities. Because of their special optical and electrochemical properties, silver nanoparticles (Ag NPs) have grown especially useful in biotechnological and diagnostic uses [25]. Figure 1.6 shows an overview of the green synthesis process for Ag nanoparticles. Ag NPs show synergistic effects when combined with traditional treatments such as antibiotics or anti-inflammatory medications, thus improving therapeutic results. Ag NPs are particularly interesting candidates for focused cancer treatments since they have shown selective toxicity towards cancerous cells while sparing healthy ones [26]. A study by Sriram et al. [27] showed that Ag NPs helped normal body weight recover by 65% by lowering tumor-related ascitic fluid in mice. Their antimicrobial action is also very important for tissue healing and wound healing, which makes them great ingredients in sophisticated wound care products. Al_2O_3 nanoparticles produced via green synthesis exhibit high biocompatibility, allowing easier interaction with bacterial membranes [28]. Figure

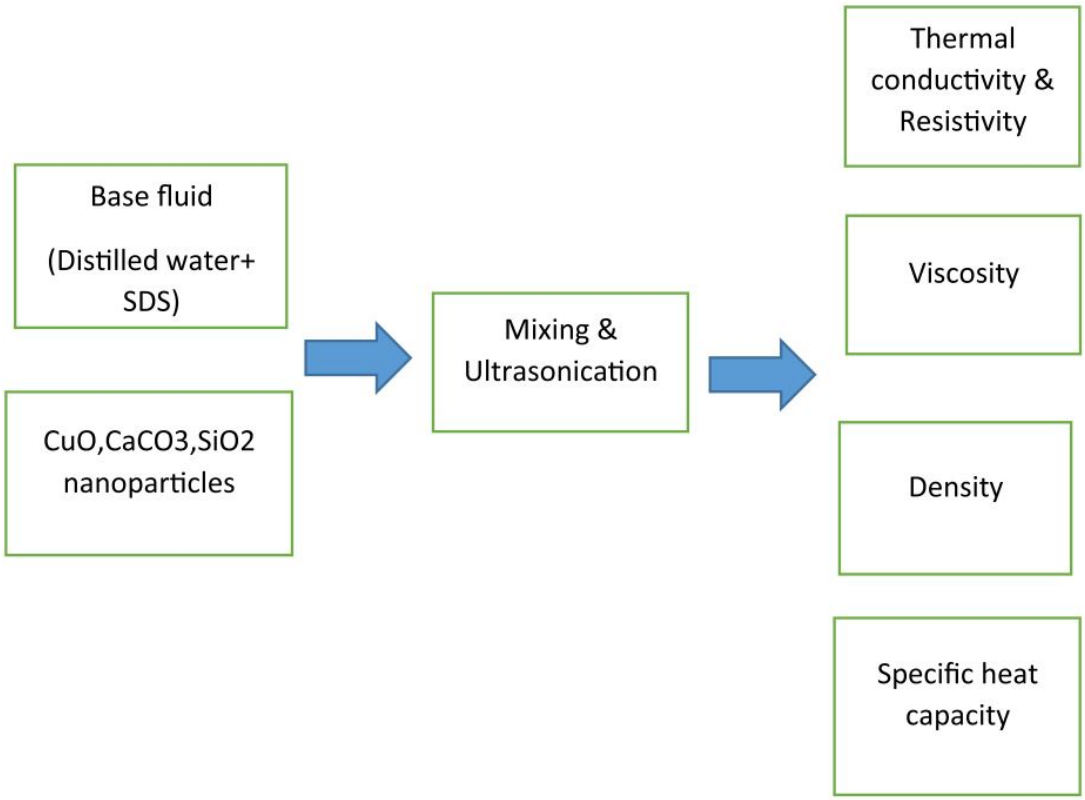


Figure 1.5 : The graphical abstract of the study [21].

1.7 shows the process by which green Al_2O_3 nanoparticles interact with and penetrate bacterial membranes. Upon penetration, these nanoparticles release Al^{3+} ions and reactive oxygen species that interfere with cellular respiration, denature vital proteins, damage genetic material, oxidize lipids, and ultimately lead to membrane disruption and bacterial death. Renowned for its brilliant white pigment, titanium dioxide (TiO_2) also provides interesting characteristics, including non-toxicity, photocatalytic activity, and fluorescence [29]. These qualities help to explain its potential in systems of cancer protection. TiO_2 is also extensively used in environmental restoration. Analogous antibacterial efficacy is shown by TiO_2, SiO_2, and ZnO_2 nanoparticles.

Converging/diverging channel flow, or Jeffrey-Hamel flow, has become a significant research area since the time that was studied by Jeffery [30] and Hamel [31], who initially investigated Newtonian viscous flow. The classic problem has been of interest due to its numerous engineering applications. The Jeffrey-Hamel model were extended to cope with complex thermal and multi-physics effects by several scientists [32–35]. Figure 1.8 illustrates the physical model of nanofluid flow under the influence of a magnetic field in converging/diverging channels. The extension of the Jeffrey-Hamel flow to study heat transfer in problems was started by Millsaps and Pohlhausen [36],

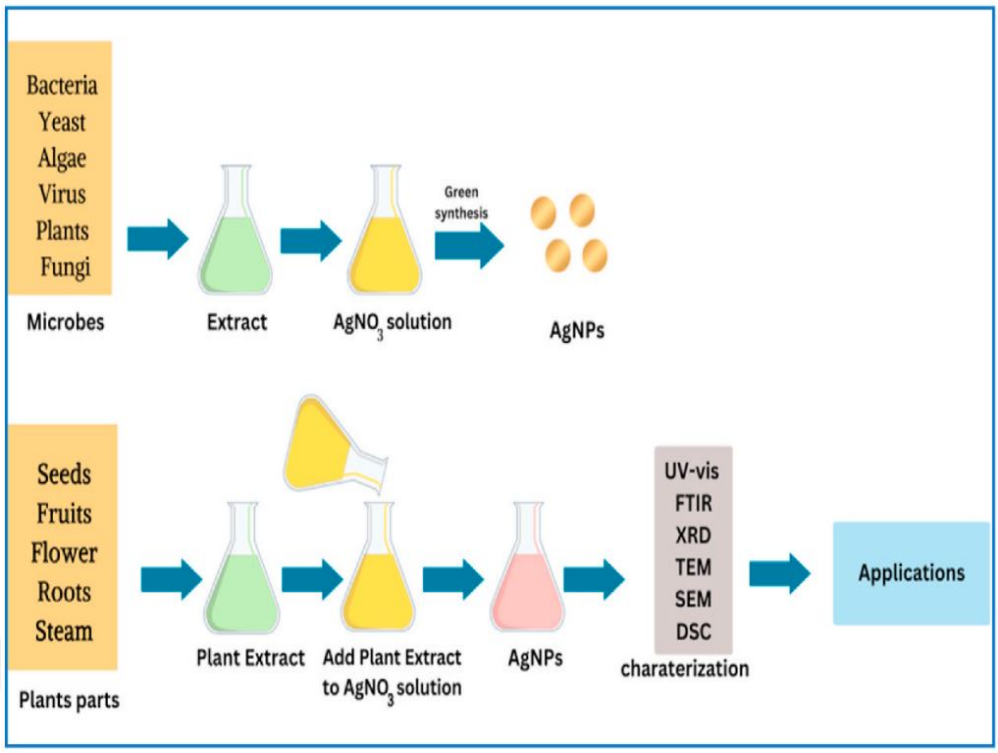


Figure 1.6 : An outline of the green synthesis method for Ag nanoparticles [25].

where exact numerical temperature distributions were provided for steady, laminar, incompressible flows in convergent-divergent channels. Subsequent investigations have examined hydrodynamic stability as well as associated physical processes, as studied by Eagles [37] and Uribe et al. [38].

With the advancing computational methods, Moghimi et al. [39] numerically solved the MHD Jeffrey-Hamel flow problem. Moradi et al. [40] applied analytical (DTM) and numerical (RK4) schemes for solutions of nanofluid flow with various nanoparticles (Al_2O_3, Cu, TiO_2). Other modifications of the original problem were performed by Turkyilmazoglu [41] with stretching/shrinking wall influences. Thereafter, Gerdroodbary et al. [42] explained the influence of thermal radiation using the Rosseland approximation and concluded that the increased parameters of radiation enhanced the temperature distributions. The problem of Jeffrey-Hamel remains to be solved using different analytical and numerical procedures, testifying to its significance in fluid mechanics studies. New extensions that are now being developed are nanofluids, MHD forces, and thermal radiation, demonstrating the dynamism of the model in addressing the contemporary challenges of engineering.

The use of slip boundary conditions for Jeffrey-Hamel flow has created new horizons for the simulation of fluid dynamics for microscale and bio-inspired devices. It

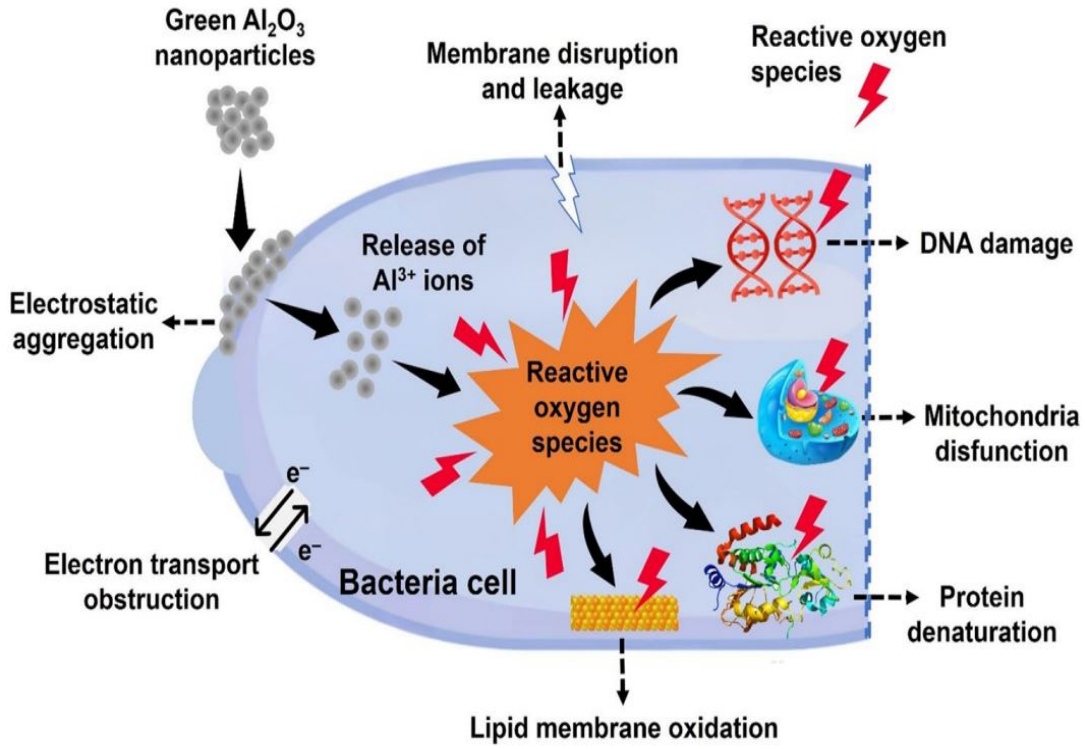


Figure 1.7 : The mechanism by which Al_2O_3 nanoparticles interact with and penetrate bacterial membranes [28].

was Dorrepaal [43] who initially investigated how velocity slip affects the flow pattern between non-parallel plates. This pioneering work was extended by Al-Nimr et al. [44], who employed first and second-order velocity slip conditions, extensively analyzing the manner in which the Knudsen number varies velocity profiles and wall slip effects. Other studies accounted for slip effects in nanofluid flows. Mohyud-Din et al. [45] researched Ag/water and Cu/water nanofluid flows under velocity and thermal slip conditions and solved the resulting nonlinear PDEs analytically. Similarly, Khan et al. [46] researched SWCNT and MWCNT nanofluid flows in diverging/converging channels with slip conditions. Shukla et al. [47] researched entropy generation in HNFs accounting for slip effects. Magnetohydrodynamic (MHD) effects have also been utilized in the modeling of many physical scenarios in Jeffrey-Hamel flow. Sheikholeslami et al. [48] utilized the Adomian Decomposition Method in the study of nanofluid flow under strong magnetic fields and proved that higher Hartmann numbers decrease backflow at greater Reynolds numbers or channel angles. Hatami and Ganji [49] also investigated MHD nanofluid dynamics through WRMs and the Runge-Kutta method in converging/diverging channels. Apart from fluid dynamics, these concepts have biomedical applications, primarily in bio-magnetic fluids like blood. Because they have a high surface area-to-volume

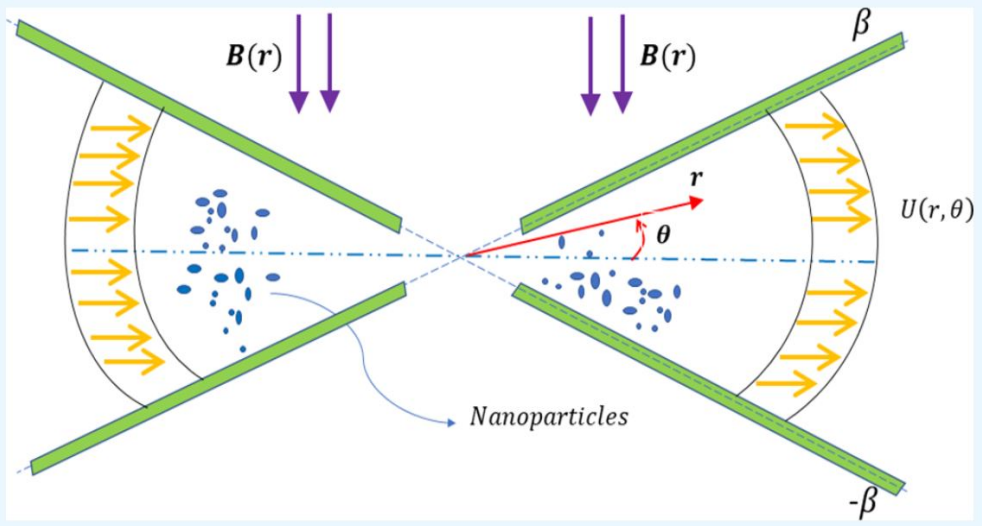


Figure 1.8 : The physical configuration of nanofluid flow subjected to a magnetic field in converging and diverging channels [35].

ratio, nanoparticles are employed in targeted drug delivery, cancer hyperthermia, and for biosensor enhancement [50, 51]. Blood is of complex rheological character, exhibiting non-Newtonian behavior under low shear rates and approaching Newtonian at high shear rates [52–56]. Blood viscosity also varies depending on the haematocrit level. Figure 1.9 shows how blood viscosity changes with shear rate at different haematocrit values. Various non-Newtonian models are used to simulate this behavior. Figure 1.10 presents the shear rate–viscosity relationship for different non-Newtonian models. This dualistic aspect influences medical interventions as well as fluid dynamics modeling, referring to the interdisciplinary merit of slip and MHD effects in Jeffrey-Hamel flow.

Fluid flow through porous media is a topic of growing interest due to its wide-ranging applications [57–59]. The complexity of such flows arises from interactions between the fluid, porous structure, and solid matrix. Darcy's law, first proposed by Darcy [60], provided an early model for such flow but was later extended by Forchheimer [61], who introduced a nonlinear velocity term, known as the Forchheimer term, as identified by Muskat [62]. This extended Darcy–Forchheimer model has since been applied to diverse fluid scenarios [33, 63–65]. Scientists are interested in studying non-Newtonian fluids, referred to as viscous complex fluids, due to their physical characteristics and widespread utilization in technological and industrial processes [66, 67]. The correlation between the shear stress and shear strain rate is nonlinear in the non-Newtonian fluids. Previous studies have demonstrated that

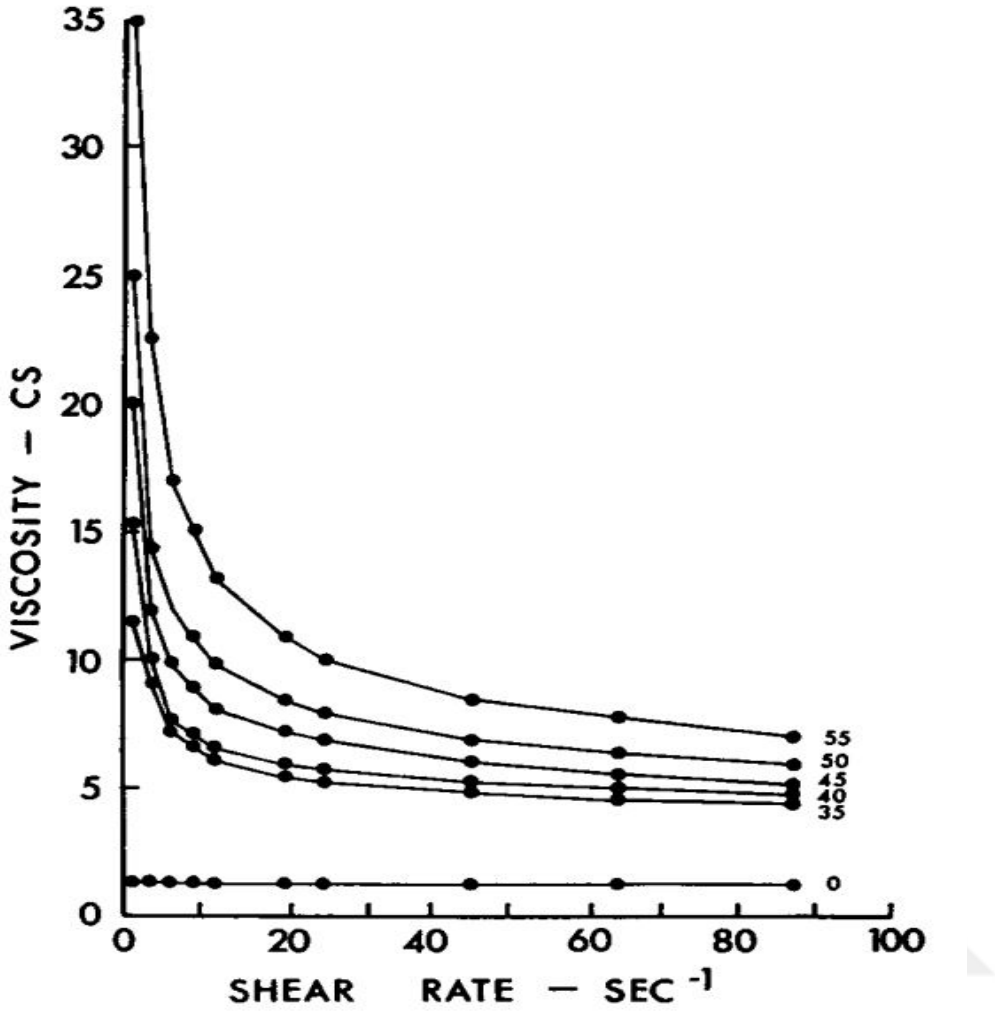


Figure 1.9 : The shear-thinning properties of whole blood at different haematocrit levels and the nearly Newtonian behavior of plasma [52].

numerous biological fluids have non-Newtonian behavior. Azmi et al. [66] utilized the Au/blood Casson non-Newtonian NF to analyze the unsteady flow with natural convective effects in a cylinder representing an artery. Figure 1.11 depicts the physical configuration of the study. Due to its benefits for biomedical (COVID-19 and cancer therapy) applications, Arif et al. [68] used a Casson non-Newtonian TNF, consisting of spherical Fe_3O_4, platelet-shaped Zn, and cylindrical Au nanoparticles in blood, in the Couette flow. For example, second-grade and hybrid nanofluids have been used to study thermo-diffusion, entropy generation, and heat transfer enhancement in convergent/divergent channels [69, 70]. Different non-Newtonian models have been used to simulate blood flow. A recent study by Gunay et al. [71] used a Newtonian approximation combined with TNF to analyze the effects in larger arteries, while also investigating the influence of various physical parameters in a converging/diverging channel.

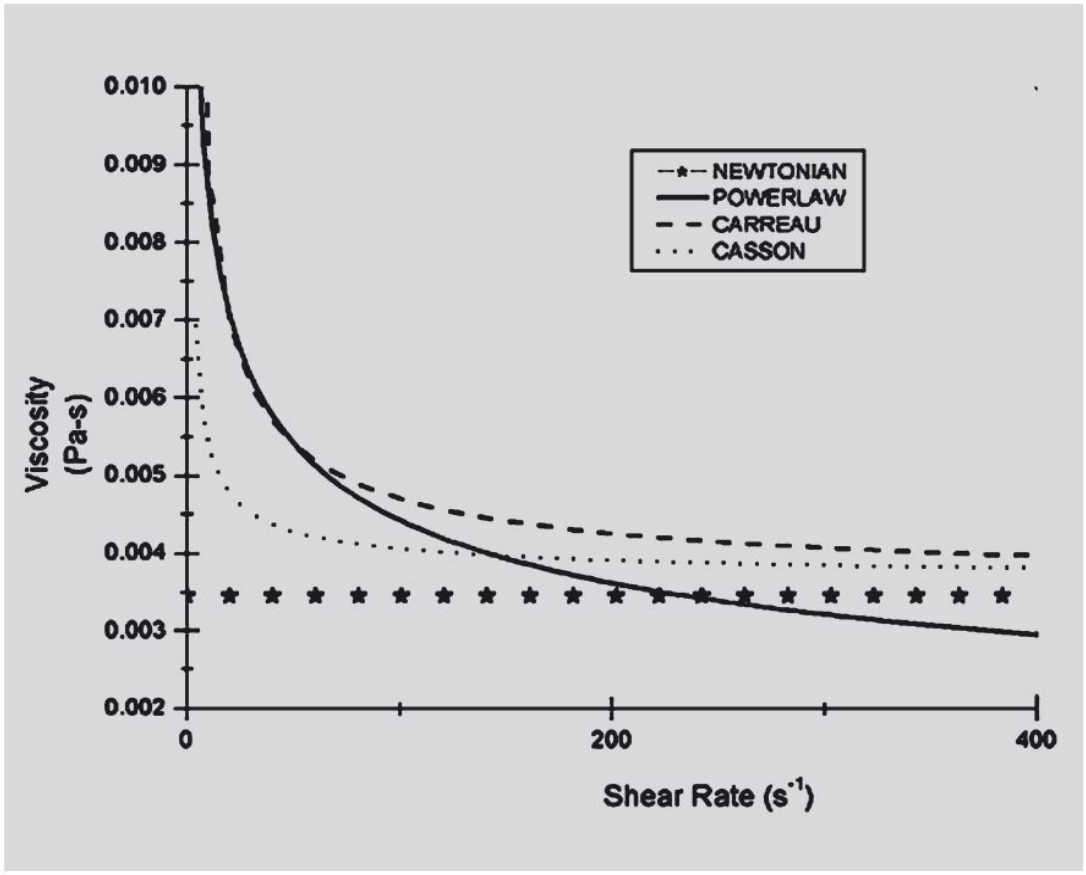


Figure 1.10 : The variation of viscosity with shear rate for various non-Newtonian models [55].

1.2 Motivation

This research introduces a new investigation of Jeffrey-Hamel flow with second-grade non-Newtonian fluid through a non-Darcian porous medium based on blood as the base fluid. In contrast to existing research, our investigation involves four crucial phenomena: thermal radiation, magnetic field, velocity slip, and temperature jump boundary conditions, utilizing medically relevant Al_2O_3-Ag-TiO_2 nanoparticles with recognized healing effects in oncology and drug delivery in converging/diverging channels embedded in porous media. Moreover, a second-grade non-Newtonian model was employed to understand the effects of physical parameters in small arteries. Different shape factors have been used to investigate how the geometries of different nanoparticles can affect flow behaviors and heat transfer processes. To study the interactive effects of all these physical variables, the problem has been mathematically represented under the existing conditions. Through convenient similarity transformations, the complex governing equations are reduced to a coupled system of nonlinear ODEs, which are then solved using MATLAB's bvp4c solver that

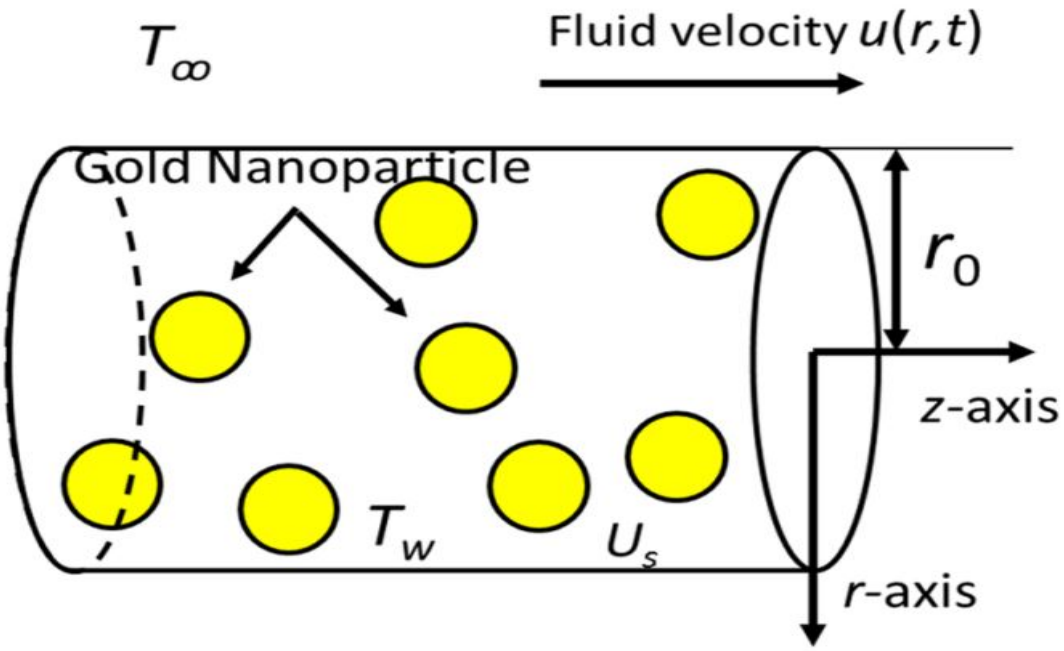


Figure 1.11 : The physical model of the study [66].

uses the finite difference collocation method and adaptive mesh refinement scheme for improved accuracy in the solution. The obtained results were validated by comparing them with previous studies. Besides other Jeffrey-Hamel studies, additional parameters have been investigated in this paper. The influence of varying physical and thermal parameters on the flow velocity, temperature profile, and engineering parameters was thoroughly examined utilizing graphical plots as well as tabulated results. The study presents fundamental information about how second-grade blood-based TNF flow works under combined magnetic-thermal-radiative impacts in converging/diverging channels and how varied physical and thermal parameters influence it. Furthermore, this work presents a clear description of the effect of wall slip and jump-temperature on Jeffrey-Hamel flow dynamics with TNF.

1.3 Outline of the Thesis

The structure of the thesis is explained. In Chapter 2, assumptions are made to model the physical model, and based on these assumptions, the partial differential equations (PDEs) governing continuity, momentum, and energy equations are formulated. Since the nanofluid is used, formulas are introduced to define the thermophysical properties of the nanofluid within the PDEs. In Chapter 3, the PDEs are reduced to ordinary differential equations (ODEs) through similarity variables to solve the problem. In

Chapter 4, the resulting ODEs are solved using the bvp4c function, which implements the finite difference collocation method, and the accuracy of the code is checked by comparison of the results obtained with those in the literature. Chapter 5 displays the effects of dimensionless parameters and some coefficients defining the physical configuration on velocity and temperature profiles, and on engineering parameters. The conclusion at the end summarizes the key parameters and indicates the main findings of the research.

2. PARTIAL DIFFERENTIAL EQUATIONS FOR PHYSICAL MODEL

In the present research work, steady, two-dimensional, incompressible flow of the viscous fluid is considered with a source and sink at the interface of two rigid inclined surfaces. It is a physical model of blood flow through a second-grade non-Newtonian nanofluid model, in which the thermal radiation and magnetic field effects are considered within the non-Darcy porous medium. The flow is in symmetric converging and diverging channels along the centerline, and the channel half-angle is designated by α. The analysis is conducted in the cylindrical coordinate system; the flow velocity has one component in the radial direction and is a function of r and θ and is independent of z. The slip-velocity and temperature jump conditions are implemented as boundary conditions at the walls. The blood flow with the suspension of Al_2O_3, TiO_2 and Ag nanoparticles in the fluid was investigated using the second-grade nanofluid model. Figure 2.1 illustrates the physical model of the problem under consideration.

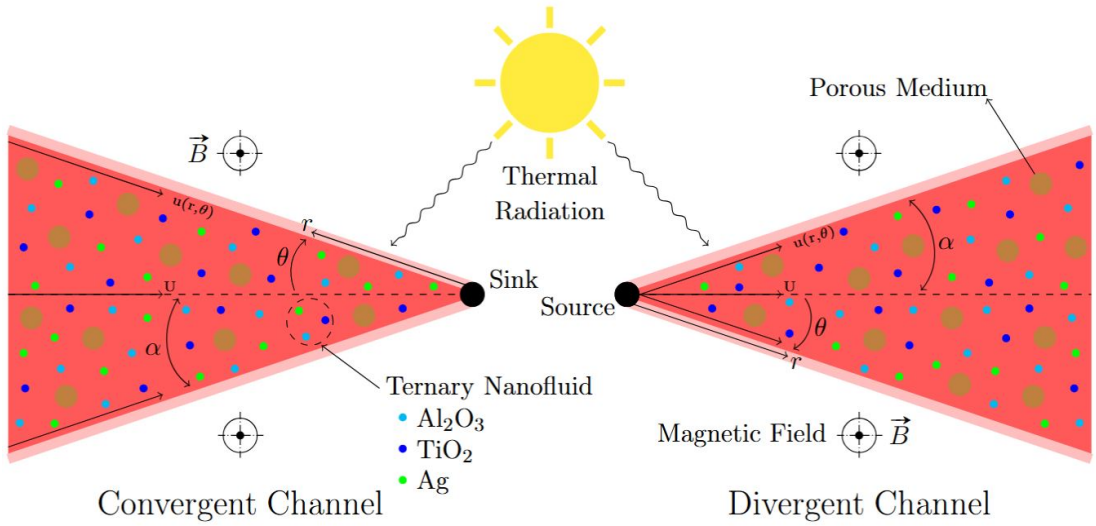


Figure 2.1 : Nanofluid flow through converging/diverging porous channels under thermal radiation and magnetic media effects.

2.1 Partial Differential Equations for Continuity, Momentum, and Energy Equations

The continuity, momentum, and energy equations are obtained based on the assumptions mentioned [33, 47, 49, 72, 73]. Assumptions are incorporated into equations using different terms.

$$\frac{\rho_{\text{tnf}}}{r}\frac{\partial(ru_r)}{\partial r}=0 \tag{2.1}$$

$$\begin{aligned} u_r\frac{\partial u_r}{\partial r} &= \frac{-1}{\rho_{\text{tnf}}}\frac{\partial P}{\partial r}+\frac{\mu_{\text{tnf}}}{\rho_{\text{tnf}}}\left(2\frac{\partial^2 u_r}{\partial r^2}+\frac{2}{r}\frac{\partial u_r}{\partial r}+\frac{1}{r^2}\frac{\partial^2 u_r}{\partial\theta^2}-\frac{2u_r}{r^2}\right)\\ &-\frac{\alpha_1}{\rho_{\text{tnf}}}\left(\frac{2u_r}{r}\frac{\partial^2 u_r}{\partial r^2}+2\frac{\partial u_r}{\partial r}\frac{\partial^2 u_r}{\partial r^2}-\frac{2}{r^3}\left(\frac{\partial u_r}{\partial\theta}\right)^2+2u_r\frac{\partial^3 u_r}{\partial r^3}-\frac{1}{r^2}\frac{\partial u_r}{\partial\theta}\frac{\partial^2 u_r}{\partial r\partial\theta}\right)\\ &-\frac{\alpha_1}{\rho_{\text{tnf}}}\left(\frac{1}{r^2}\frac{\partial^2 u_r}{\partial r\partial\theta}+\frac{\partial u_r}{\partial r}\frac{\partial^2 u_r}{\partial\theta^2}-\frac{2u_r}{r^3}\frac{\partial^2 u_r}{\partial\theta^2}+\frac{u_r}{r^2}\frac{\partial^3 u_r}{\partial r^2\partial\theta}+\frac{2u_r^2}{r^3}-\frac{2u_r}{r^2}\frac{\partial u_r}{\partial r}\right)\\ &-\frac{\sigma_{\text{tnf}}}{\rho_{\text{tnf}}}\frac{B_0^2}{r^2}u_r-\frac{\mu_{\text{tnf}}\text{Pr}_\text{o}}{\rho_{\text{tnf}}\text{Pr}_\text{e}}u_r-\frac{C_{\text{pd}}\text{Pr}_\text{o}}{\sqrt{\text{Pr}_\text{e}}}u_r^2 \end{aligned} \tag{2.2}$$

$$\begin{aligned} 0 &= -\frac{1}{r\rho_{\text{tnf}}}\frac{\partial P}{\partial\theta}+\frac{2}{r^2}\frac{\mu_{\text{tnf}}}{\rho_{\text{tnf}}}\frac{\partial u_r}{\partial\theta}\\ &-\frac{\alpha_1}{r^2\rho_{\text{tnf}}}\frac{\partial}{\partial r}\left(r^2\left(\frac{1}{r}\frac{\partial u_r}{\partial\theta}\frac{\partial u_r}{\partial r}+\frac{2}{r^2}\frac{\partial u_r}{\partial\theta}\frac{\partial u_r}{\partial r}-\frac{2u_r}{r^2}\frac{\partial u_r}{\partial\theta}+\frac{\partial^2 u_r}{\partial\theta^2}+\frac{u_r}{r}\frac{\partial^2 u_r}{\partial r\partial\theta}\right)\right)\\ &-\frac{\alpha_1}{r\rho_{\text{tnf}}}\frac{\partial}{\partial\theta}\left(\frac{1}{r^2}\left(\frac{\partial u_r}{\partial\theta}\right)^2-\frac{2u_r^2}{r^2}+\frac{2u_r}{r^2}\frac{\partial u_r}{\partial r}\right) \end{aligned} \tag{2.3}$$

$$\begin{aligned} u_r\frac{\partial T}{\partial r} &= \frac{k_{\text{tnf}}}{(\rho C_P)_{\text{tnf}}}\left(\frac{\partial^2 T}{\partial r^2}+\frac{1}{r}\frac{\partial T}{\partial r}+\frac{1}{r^2}\frac{\partial^2 T}{\partial\theta^2}\right)\\ &+\frac{\mu_{\text{tnf}}}{(\rho C_P)_{\text{tnf}}}\left(2\left(\left(\frac{\partial u_r}{\partial r}\right)^2+\left(\frac{u_r}{r}\right)^2\right)+\left(\frac{1}{r}\frac{\partial u_r}{\partial\theta}\right)^2\right)\\ &-\frac{1}{(\rho C_P)_{\text{tnf}}r}\frac{\partial}{\partial r}\left(rq_{r,rad}\right)-\frac{1}{(\rho C_P)_{\text{tnf}}r^2}\frac{\partial}{\partial\theta}\left(q_{\theta,\text{ rad.}}\right)\\ &+\frac{1}{(\rho C_P)_{\text{tnf}}}\frac{\sigma_{\text{tnf}}}{r^2}B_0^2u_r^2-2\frac{1}{(\rho C_P)_{\text{tnf}}}\frac{\alpha_1}{r^3}\left(u_r\left(\frac{\partial u_r}{\partial r}\right)^2+4u_r^3\right) \end{aligned} \tag{2.4}$$

In the momentum equation in the r direction (equation (2.2)), Pr_o represents the porous medium porosity, Pr_e represents the porous medium permeability, and C_{pd} denotes the constant drag coefficient.

The Rosseland approximation is employed in the energy equation to observe the impact of thermal radiation. Rosseland approximation is a heat transport and energy transfer modeling method used in problems of high-opacity material where radiation

absorption and emission dominate [74–76]. It provides an expression for the net radiative heat flux. This expression is written as follows.

$$q_{\mathrm{r}} = -\frac{4}{3a_{\mathrm{R}}}\,\mathrm{grad}\,(e_{\mathrm{b}}) \tag{2.5}$$

Here, a_{R} represents the Rosseland mean spectral absorption coefficient. e_{b} denotes the blackbody emissive power. This term can be written based on the absolute temperature (T) using the Stefan-Boltzmann radiation law: $e_{\mathrm{b}} = \sigma^* T^4$.

$$q_{r,rad} = -\left(4\sigma^*/3{k_{\mathrm{tnf}}}^*\right)\frac{\partial T^4}{\partial r} \tag{2.6}$$

$$q_{\theta,rad} = -\left(4\sigma^*/3{k_{\mathrm{tnf}}}^*\right)\frac{\partial T^4}{\partial \theta} \tag{2.7}$$

σ^* represents the Stefan-Boltzmann constant. Since TNF is the fluid, a_{R} is replaced in the equation (2.5) with ${k_{\mathrm{tnf}}}^*$. The mean absorption coefficient is expressed by ${k_{\mathrm{tnf}}}^*$. In cases, when the wall temperature T_w is just slightly different from the freestream temperature (T_∞), the T^4 term can be expressed as a linear function of temperature. This process can be performed using the Taylor series. The T^4 term is written by using the Taylor series. We thus simplify the expression by extending T^4 about T_∞, ignoring the high-order terms.

$$T^4 \cong 4T_\infty^3 T - 3T_\infty^4 \tag{2.8}$$

The Rosseland approach has both mathematical and physical advantages since it can be coupled with Fourier's second law of conduction. Polar coordinates are used in the present study, and hence, the heat flux in the θ and r directions is considered. As indicated earlier, the properties must be given in terms of the TNF. Following all these procedures, the following energy equation is obtained.

$$\begin{aligned} u_r\frac{\partial T}{\partial r} &= \frac{k_{\mathrm{tnf}}}{(\rho C_P)_{\mathrm{tnf}}}\left(\frac{\partial^2 T}{\partial r^2} + \frac{1}{r}\frac{\partial T}{\partial r} + \frac{1}{r^2}\frac{\partial^2 T}{\partial \theta^2}\right) \\ &+ \frac{\mu_{\mathrm{tnf}}}{(\rho C_P)_{\mathrm{tnf}}}\left(4\left(\frac{\partial u_r}{\partial r}\right)^2 + \frac{1}{r^2}\left(\frac{\partial u_r}{\partial \theta}\right)^2\right) + \frac{16\sigma^* T_\infty^3}{3{k_{\mathrm{tnf}}}^*(\rho C_P)_{\mathrm{tnf}}}\left(\frac{\partial^2 T}{\partial r^2} + \frac{1}{r}\frac{\partial T}{\partial r}\right) \\ &+ \frac{16\sigma^* T_\infty^3}{3{k_{\mathrm{tnf}}}^*(\rho C_P)_{\mathrm{tnf}}}\left(\frac{\partial^2 T}{\partial^2 \theta}\right) + \frac{1}{(\rho C_P)_{\mathrm{tnf}}}\frac{\sigma_{\mathrm{tnf}}}{r^2}B_0^2 u_r^2 \end{aligned} \tag{2.9}$$

2.2 Partial Differential Equations for Boundary Conditions

There are several solutions for the Jeffrey-Hamel flow [77]. However, in the classical solution, the centerline symmetry condition is considered in the solution of the flow.

In the classical Jeffrey-Hamel solution, the maximum velocity value occurs at the center of the channel, where the derivative of velocity is also zero. Also, the highest temperature is at the center of the channel when considering the temperature profile. According to this fact, the boundary conditions on the centerline for the classical Jeffrey-Hamel flow are established below.

$$\frac{\partial u}{\partial \theta} = 0, \quad \frac{\partial T}{\partial \theta} = 0, \quad u = \mathrm{U}, \quad \text{at } \theta = 0 \tag{2.10}$$

In the classic Jeffrey-Hamel problem, the velocity at the wall is zero due to the no-slip condition, and the temperature boundary condition at the wall is equal to the wall temperature. However, a non-Newtonian model has been used for blood. Experimental data reveal that flow slip occurs in non-Newtonian fluids and significantly influences the flow [78].

In addition, due to its effectiveness in processes such as drug delivery and tumor therapy, slip boundary conditions have been used at the wall [79]. Although some studies incorporate the viscosity term in investigating slip-velocity at the wall, others neglect its effect [80–82]. In the present study, since TNF is employed and the effect of nanoparticles on viscosity has to be considered, equations containing the viscosity term have been employed. Based on the assumptions made, the boundary conditions at the wall are as follows.

$$u = -\mathrm{S_v}\nu_{\mathrm{tnf}}\frac{\partial u}{\partial \theta}, \quad T = T_w = \frac{C_w}{r^2} - \mathrm{J_T}\frac{\partial T}{\partial \theta} \quad \text{at} \quad \theta = \alpha \tag{2.11}$$

U, C_w, $\mathrm{S_v}$, and $\mathrm{J_T}$ parameters utilized in the equations (2.10) and (2.11) represent velocity at the center of the channel, temperature at the walls, slip-velocity parameter, and temperature jump parameter, respectively.

2.3 Partial Differential Equations for Engineering Parameters

Engineering parameters that include C_f and Nu are calculated to investigate the effectiveness of physical conditions and TNF [33].

$$C_f = \frac{\tau_w}{\rho_{\mathrm{f}}\mathrm{U}^2}, \quad \text{where } \tau_w = \frac{\mu_{\mathrm{tnf}}}{r}\frac{\partial u}{\partial \theta}\bigg|_{\theta=\alpha}. \tag{2.12}$$

$$\mathrm{Nu} = \frac{r^3 q_w}{k_{\mathrm{f}}(C_w)}, \quad \text{where } q_w = -\left(k_{\mathrm{tnf}} + \frac{16\sigma^* T_\infty^3}{3k^*_{\mathrm{tnf}}}\right) \frac{1}{r}\frac{\partial T}{\partial \theta}\bigg|_{\theta=\alpha}. \tag{2.13}$$

2.4 Thermophysical Properties of TNF

Maxwell established an Effective Medium Theory (EMT) based formula for the thermal conductivity of composite mixes [83]. The models derived based on Maxwell's model have been used in numerous numerical studies involving mono and hybrid nanofluids [84, 85]. Unlike the previously mentioned models, in recent years, empirical correlations have been developed for mono, hybrid, and ternary nanofluids [86–88]. In the present study, the Hamilton-Crosser model was applied to account for the effect of the nanofluid's shape factor. By considering the interfacial thermal resistance between nanoparticles and the base fluid, the Hamilton-Crosser model helps to estimate the effective thermal conductivity of nanofluids [89–91]. The thermal conductivity formula based on the Hamilton-Crosser model and the other thermophysical properties of TNF are given in Table 2.1. The term Φ in the formulas represents the volume fraction.

Since a non-Newtonian model was used to simulate the flow in convergent and divergent arteries, the properties of blood were used as the base fluid with properties of nanoparticles [29, 50, 91]. The thermophysical properties of the particles and blood are provided in Table 2.2. The concentration of nanoparticles in the blood should be within a specific range to avoid toxic effects. Appropriate volume fractions were selected based on studies in the literature that used Al_2O_3, TiO_2, and Ag nanoparticles [29, 50, 91].

In the work of Timofeeva et al. [92], the fluid thermal conductivity was analyzed for platelets, blades, bricks, cylinders, and spheres. In this work, these geometries were also considered. The s_p term in the equations represents the shape of the nanoparticles and differs for different shapes. The s_p value for different nanoparticle shapes is presented in Table 2.3.

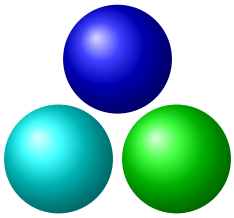
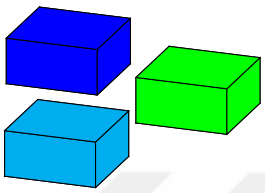
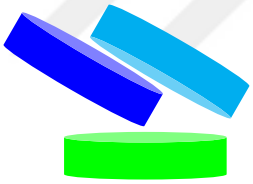
Table 2.1 : Thermophysical properties of Al_2O_3-TiO_2-Ag/blood ternary nanofluid [89-91].

Properties	Ternary Nanofluid
Dynamic viscosity	$\frac{\mu_{\text{tnf}}}{\mu_{\text{f}}} = (1-\Phi_1)^{-2.5}(1-\Phi_2)^{-2.5}(1-\Phi_3)^{-2.5}$
Density	$\rho_{\text{tnf}} = (1-\Phi_3)\Big\{(1-\Phi_2)\Big[(1-\Phi_1)\rho_f + \Phi_1\rho_1\Big] + \Phi_2\rho_2\Big\} + \Phi_3\rho_3$
Kinematic Viscosity	$\nu_{\text{tnf}} = \frac{\mu_{\text{tnf}}}{\rho_{\text{tnf}}}$
Heat capacity	$(\rho C_P)_{\text{tnf}} = (1-\Phi_3)\Big\{(1-\Phi_2)[(1-\Phi_1)(\rho C_P)_{\text{f}} + \Phi_1(\rho C_P)_1] + \Phi_2(\rho C_P)_2\Big\} + \Phi_3(\rho C_P)_3$
Thermal conductivity	$\frac{k_{\text{tnf}}}{k_{\text{hnf}}} = \frac{k_3 + (s_{\text{p}}-1)k_{\text{hnf}} - (s_{\text{p}}-1)\Phi_3(k_{\text{hnf}}-k_3)}{k_3 + (s_{\text{p}}-1)k_{\text{hnf}} + \Phi_3(k_{\text{hnf}}-k_3)}$ $\frac{k_{\text{hnf}}}{k_{\text{nf}}} = \frac{k_2 + (s_{\text{p}}-1)k_{\text{nf}} - (s_{\text{p}}-1)\Phi_2(k_{\text{nf}}-k_2)}{k_2 + (s_{\text{p}}-1)k_{\text{nf}} + \Phi_2(k_{\text{nf}}-k_2)}$ $\frac{k_{\text{nf}}}{k_{\text{f}}} = \frac{k_1 + (s_{\text{p}}-1)k_{\text{f}} - (s_{\text{p}}-1)\Phi_1(k_{\text{f}}-k_1)}{k_1 + (s_{\text{p}}-1)k_{\text{f}} + \Phi_1(k_{\text{f}}-k_1)}$
Electrical conductivity	$\frac{\sigma_{\text{tnf}}}{\sigma_{\text{hnf}}} = \frac{\sigma_3 + (s_{\text{p}}-1)\sigma_{\text{hnf}} - (s_{\text{p}}-1)\Phi_3(\sigma_{\text{hnf}}-\sigma_3)}{\sigma_3 + (s_{\text{p}}-1)\sigma_{\text{hnf}} + \Phi_3(\sigma_{\text{hnf}}-\sigma_3)}$ $\frac{\sigma_{\text{hnf}}}{\sigma_{\text{nf}}} = \frac{\sigma_2 + (s_{\text{p}}-1)\sigma_{\text{nf}} - (s_{\text{p}}-1)\Phi_2(\sigma_{\text{nf}}-\sigma_2)}{\sigma_2 + (s_{\text{p}}-1)\sigma_{\text{nf}} + \Phi_2(\sigma_{\text{nf}}-\sigma_2)}$ $\frac{\sigma_{\text{nf}}}{\sigma_{\text{f}}} = \frac{\sigma_1 + (s_{\text{p}}-1)\sigma_{\text{f}} - (s_{\text{p}}-1)\Phi_1(\sigma_{\text{f}}-\sigma_1)}{\sigma_1 + (s_{\text{p}}-1)\sigma_{\text{f}} + \Phi_1(\sigma_{\text{f}}-\sigma_1)}$

Table 2.2 : Thermophysical characteristics of Al_2O_3, TiO_2, Ag nanoparticles, and blood (base fluid) [29, 50, 91].

Properties	$\rho\,(\text{kg}/m^3)$	C_p(J/kgK)	k(W/m°C)	$\sigma(S/m)$
Blood	1063	3594	0.492	0.8
Al_2O_3	3970	765	40	36.9×10^6
TiO_2	4250	686.2	8.9538	2.4×10^6
Ag	10500	235	429	63×10^6

Table 2.3 : Shape factor of solid nanoparticles [92].

Nanoparticles type	Shape	Sphericity (ψ)	Shape Parameter ($s_p = 3/\psi$)
Spheres		1	3
Bricks		0.81	3.7
Cylinders		0.62	4.9
Platelets		0.52	5.7
Blades		0.36	8.6

3. CONVERSION OF PARTIAL DIFFERENTIAL EQUATIONS

Similarity variables are used to convert PDEs into ODEs. First, the continuity equation is utilized to derive an equation for velocity.

$$F(\theta) = ru_r \tag{3.1}$$

The PDEs for the energy and momentum equations are converted into dimensionless ODEs using similarity variables. Velocity and temperature values are examined using dimensionless similarity variables. Moreover, they are expressed as functions of the dimensionless angle. In non-dimensionalization used in the derivation of the dimensionless velocity, the value F_{max} is utilized. The F_{max} is maximum since the centerline velocity is maximum and is the rate of movement at the centerline. The parameter C_w in the non-dimensionalization of temperature is related to the wall temperature. From these facts, the similarity variables required for transformation are given as follows [33, 47, 49, 72, 73, 82].

$$\eta = \frac{\theta}{\alpha}, \quad f(\eta) = \frac{F(\theta)}{r\mathrm{U}} = \frac{F(\theta)}{F_{max}}, \quad g(\eta) = r^2\frac{T}{C_w} \tag{3.2}$$

Partial derivatives must be expressed in terms of dimensionless velocity and temperature to simplify PDEs to ODEs. Partial derivatives in terms of velocity are initially reduced to $F(\theta)$ and then expressed in terms of $f(\eta)$. Partial derivatives in terms of temperature values are expressed directly in terms of $g(\eta)$. Partial derivatives used for velocity terms are expressed in terms of $F(\theta)$ as given below:

$$\begin{aligned} &\frac{\partial u_r}{\partial r} = -\frac{F(\theta)}{r^2}, \frac{\partial u_r}{\partial \theta} = \frac{F'(\theta)}{r}, \frac{\partial^2 u_r}{\partial r^2} = 2\frac{F(\theta)}{r^3}, \frac{\partial^2 u_r}{\partial \theta^2} = \frac{F''(\theta)}{r}, \\ &\frac{\partial^2 u_r}{\partial \theta \partial r} = -\frac{F'(\theta)}{r^2}, \frac{\partial^3 u_r}{\partial \theta^3} = \frac{F'''(\theta)}{r}, \frac{\partial^3 u_r}{\partial \theta \partial r^2} = 2\frac{F'(\theta)}{r^3} \end{aligned} \tag{3.3}$$

The following equations are used to transform $F(\theta)$ into $f(\eta)$. In this process, the similarity variables from equation (3.2) are utilized.

$$\begin{aligned} &\mathrm{U}rf(\eta) = F(\theta),\ \frac{\mathrm{U}r}{\alpha}f'(\eta) = F'(\theta),\\ &\frac{\mathrm{U}r}{\alpha^2}f''(\eta) = F''(\theta),\ \frac{\mathrm{U}r}{\alpha^3}f'''(\eta) = F'''(\theta) \end{aligned} \tag{3.4}$$

In the next step, with the aid of similarity variables, the partial derivatives used for temperature terms are expressed in terms of $g(\eta)$ as follows:

$$\begin{aligned} &\frac{\partial T}{\partial r} = -\frac{2C_w}{r^3}g(\eta),\quad \frac{\partial^2 T}{\partial r^2} = \frac{6C_w}{r^4}g(\eta),\\ &\frac{\partial T}{\partial \theta} = \frac{C_w}{r^2\alpha}g'(\eta),\quad \frac{\partial^2 T}{\partial \theta^2} = \frac{C_w}{r^2\alpha^2}g''(\eta) \end{aligned} \tag{3.5}$$

The non-dimensional numbers that are presented in the reduced ODEs are expressed as follows [33, 69, 70, 72, 81, 82].

$$\begin{aligned} &\mathrm{Dr}_1 = \frac{r\nu_f \mathrm{Pr_o}}{\mathrm{Pr_e U}},\quad \mathrm{Dr}_2 = \frac{rC_{\mathrm{pd}}\mathrm{Pr_o}}{\sqrt{\mathrm{Pr_e}}},\quad \mathrm{De} = \frac{-\alpha_1 \mathrm{U}}{r\mu_f},\\ &\mathrm{Ec} = \frac{\alpha F_{max}^2}{C_w (C_P)_{\mathrm{f}}},\quad \mathrm{Ha} = r\sqrt{\frac{\sigma_{\mathrm{f}} B_0^2}{\rho_{\mathrm{f}}\nu_{\mathrm{f}}}},\quad \mathrm{Pr} = \frac{F_{max}(\rho C_P)_{\mathrm{f}}}{k_{\mathrm{f}}}\\ &\mathrm{Re} = \frac{F_{max}\alpha}{\nu_{\mathrm{f}}},\quad \mathrm{Rd} = \frac{16\sigma^* T_\infty^3}{3k_{\mathrm{nf}}^* k_{\mathrm{tnf}}},\quad \mathrm{s_v} = \frac{\mathrm{S_v}\nu_{\mathrm{f}}}{\alpha},\quad \mathrm{j_t} = \frac{\mathrm{J_T}}{\alpha} \end{aligned} \tag{3.6}$$

The R coefficients in the reduced ODEs are calculated utilizing the formulas in Table 2.1 and are written below.

$$R_1 = \frac{\mu_{\mathrm{tnf}}}{\mu_{\mathrm{f}}},\quad R_2 = \frac{\rho_{\mathrm{tnf}}}{\rho_{\mathrm{f}}},\quad R_3 = \frac{(\rho C_p)_{\mathrm{tnf}}}{(\rho C_p)_{\mathrm{f}}},\quad R_4 = \frac{k_{\mathrm{tnf}}}{k_{\mathrm{f}}},\quad R_5 = \frac{\sigma_{\mathrm{tnf}}}{\sigma_{\mathrm{f}}} \tag{3.7}$$

3.1 Conversion of Momentum Equations

To begin the transformation, the momentum equations in the r and θ directions are written using the correlations of $F(\theta)$ from equation (3.3), as follows:

$$\begin{aligned} \frac{1}{\rho_{\mathrm{tnf}}}\frac{\partial P}{\partial r} = &\frac{F^2}{r^3} + \frac{\mu_{\mathrm{tnf}}}{\rho_{\mathrm{tnf}}}\frac{F''}{r^3} - \frac{\alpha_1}{\rho_{\mathrm{tnf}} r^5}\left[8F^2 + 2F'^2 + 4FF''\right]\\ &- \frac{\sigma_{\mathrm{tnf}}}{\rho_{\mathrm{tnf}}}B_0^2\frac{F}{r^3} - \frac{\mu_{\mathrm{tnf}}\mathrm{Pr_o}}{\rho_{\mathrm{tnf}}\mathrm{Pr_e}}\frac{F}{r} - \frac{C_{\mathrm{pd}}\mathrm{Pr_o}}{\sqrt{\mathrm{Pr_e}}}\frac{F^2}{r^2} \end{aligned} \tag{3.8}$$

$$\frac{1}{\rho_{\mathrm{tnf}}}\frac{\partial P}{\partial \theta} = \frac{2\nu_{\mathrm{tnf}}F'}{r^2} + \frac{2\alpha_1}{\rho_{\mathrm{tnf}} r^4}\left[F'F''\right] \tag{3.9}$$

The derivative of equation (3.8) with respect to θ and the derivative of equation (3.9) with respect to r are taken.

$$\begin{aligned}\frac{1}{\rho_{\text{tnf}}}\frac{\partial P}{\partial r\partial\theta} &= \frac{2FF'}{r^3}+\frac{\mu_{\text{tnf}}}{\rho_{\text{tnf}}}\frac{F'''}{r^3}-\frac{\alpha_1}{\rho_{\text{tnf}}r^5}\left[16FF'+4F'F''+4F'F''+4FF'''\right]\\ &-\frac{\sigma_{\text{tnf}}}{\rho_{\text{tnf}}}B_0^2\frac{F'}{r^3}-\frac{\mu_{\text{tnf}}\text{Pr}_{\text{o}}}{\rho_{\text{tnf}}\text{Pr}_{\text{e}}}\frac{F'}{r}-\frac{C_{\text{pd}}\text{Pr}_{\text{o}}}{\sqrt{\text{Pr}_{\text{e}}}}\frac{2FF'}{r^2}\end{aligned} \tag{3.10}$$

$$\frac{1}{\rho_{\text{tnf}}}\frac{\partial P}{\partial\theta\partial r} = -\frac{4\nu_{\text{tnf}}F'}{r^3}-\frac{8\alpha_1}{\rho_{\text{tnf}}r^5}\left[F'F''\right] \tag{3.11}$$

To eliminate the pressure terms, a cross-differentiation process is applied. Then, the two equations are combined as shown below.

$$\begin{aligned}&\frac{2}{r^3}F'F+4\frac{\mu_{\text{tnf}}}{\rho_{\text{tnf}}}\frac{1}{r^3}F'+\frac{\mu_{\text{tnf}}}{\rho_{\text{tnf}}}\frac{1}{r^3}F'''-\frac{\sigma_{\text{tnf}}}{\rho_{\text{tnf}}}\frac{B_0^2}{r^3}F'\\ &-\frac{\mu_{\text{tnf}}\text{Pr}_{\text{o}}}{\rho_{\text{tnf}}\text{Pr}_{\text{e}}}\frac{F'}{r}-\frac{C_{\text{pd}}\text{Pr}_{\text{o}}}{\sqrt{\text{Pr}_{\text{e}}}}\frac{2FF'}{r^2}-\frac{\alpha_1}{\rho_{\text{tnf}}r^5}\left[16FF'+4FF'''\right]=0\end{aligned} \tag{3.12}$$

Equation (3.12) is first multiplied by r^3 and then divided by $\mu_{\text{tnf}}/\rho_{\text{tnf}}$. Finally, the terms are appropriately arranged, and the following equation is obtained.

$$\begin{aligned}&F'''+2\frac{\rho_{\text{tnf}}}{\mu_{\text{tnf}}}F'F+4F'-\frac{\sigma_{\text{tnf}}}{\mu_{\text{tnf}}}B_0^2F'-\frac{\text{Pr}_{\text{o}}}{\text{Pr}_{\text{e}}}F'r^2\\ &-2\frac{\rho_{\text{tnf}}}{\mu_{\text{tnf}}}\frac{C_{\text{pd}}\text{Pr}_{\text{o}}}{\sqrt{\text{Pr}_{\text{e}}}}FF'r-\frac{\alpha_1}{\mu_{\text{tnf}}r^2}\left[16FF'+4FF'''\right]=0\end{aligned} \tag{3.13}$$

Using the correlations between the terms $f(\eta)$ and $F(\theta)$ in equation (3.4), the equation is obtained in terms of $f(\eta)$ as given below.

$$\begin{aligned}&\frac{\text{U}r}{\alpha^3}f'''+2\frac{\rho_{\text{tnf}}}{\mu_{\text{tnf}}}\frac{\text{U}r}{\alpha}\text{U}rf'f+4\frac{\text{U}r}{\alpha}f'\\ &-\frac{\text{U}r}{\alpha}\frac{\sigma_{\text{tnf}}}{\mu_{\text{tnf}}}B_0^2f'-\frac{\text{Pr}_{\text{o}}}{\text{Pr}_{\text{e}}}\frac{\text{U}r}{\alpha}r^2f'-2\frac{\rho_{\text{tnf}}}{\mu_{\text{tnf}}}\frac{C_{\text{pd}}\text{Pr}_{\text{o}}}{\sqrt{\text{Pr}_{\text{e}}}}\text{U}r\frac{\text{U}r}{\alpha}rff'\\ &-\frac{\alpha_1}{\mu_{\text{tnf}}r^2}\left[16\text{U}r\frac{\text{U}r}{\alpha}ff'+4\text{U}r\frac{\text{U}r}{\alpha^3}ff'''\right]=0\end{aligned} \tag{3.14}$$

Equation (3.14) is multiplied by $a^3/\text{U}r$. Then, the ratios between the blood and TNF nanofluid properties are written in the equation to express the fluid properties relative to the base fluid. Finally, the coefficients are written in accordance with the dimensionless numbers, and the following equation is obtained.

$$
\begin{aligned}
&f''' + 2\frac{\frac{\rho_{\text{tnf}}}{\rho_f}}{\frac{\mu_{\text{tnf}}}{\mu_f}}\frac{\rho_f \mathrm{U} r\alpha}{\mu_f}\alpha f' f + 4\alpha^2 f' - \alpha^2 \frac{\frac{\sigma_{\text{tnf}}}{\sigma_f}}{\frac{\mu_{\text{tnf}}}{\mu_f}}\frac{\sigma_f}{\mu_f}B_0^2 f' \\
&- \frac{\mathrm{Pr_o}}{\mathrm{Pr_e}}\frac{\nu_f r}{\mathrm{U}}\frac{\mathrm{U}\alpha r}{\nu_f}\alpha f' - 2\frac{\frac{\rho_{\text{tnf}}}{\rho_f}}{\frac{\mu_{\text{tnf}}}{\mu_f}}\frac{\rho_f \mathrm{U} r\alpha}{\mu_f}\frac{C_{\text{pd}}\mathrm{Pr_o} r}{\sqrt{\mathrm{Pr_e}}}\alpha f f' \\
&- 4\frac{1}{\frac{\mu_{\text{tnf}}}{\mu_f}}\frac{\alpha_1 \mathrm{U}}{\mu_f r}\left[4\alpha^2 f f' + f f'''\right] = 0
\end{aligned}
\tag{3.15}
$$

The thermophysical properties within the coefficients and specific parameters are expressed using dimensionless numbers, and the ratios between the base fluid and TNF are replaced by R parameters.

$$
\begin{aligned}
&f''' + 2\frac{R_2}{R_1}\alpha\,\mathrm{Re}\, f' f + 4\alpha^2 f' - \alpha^2\frac{R_5}{R_1}\mathrm{Ha}^2 f' - \mathrm{Dr_1}\,\mathrm{Re}\,\alpha f' \\
&- 2\frac{R_1}{R_2}\mathrm{Re}\,\mathrm{Dr_2}\,\alpha f f' - 4\frac{1}{R_1}\mathrm{De}\left[4\alpha^2 f f' + f f'''\right] = 0
\end{aligned}
\tag{3.16}
$$

3.2 Conversion of Energy Equation

Similarly, the energy equation is written using the correlations for $f(\theta)$ and $g(\theta)$ given in equation (3.2).

$$
\begin{aligned}
-\frac{F}{r}\frac{2C_w}{r^3}g = &\frac{k_{\text{tnf}}}{(\rho C_p)_{\text{tnf}}}\left(\frac{6C_w}{r^4}g - \frac{1}{r}\frac{2C_w}{r^3}g + \frac{1}{r^2}\frac{C_w}{r^2\alpha^2}g''\right) \\
&+ \frac{\mu_{\text{tnf}}}{(\rho C_p)_{\text{tnf}}}\left(2\frac{F^2}{r^4} + 2\frac{F^2}{r^4} + \frac{(F')^2}{r^4}\right) \\
&+ \frac{16\sigma^* T_\infty^3}{3k_{\text{tnf}}^*(\rho C_p)_{\text{tnf}}}\left(\frac{6C_w}{r^4}g - \frac{1}{r}\frac{2C_w}{r^3}g\right) \\
&+ \frac{16\sigma^* T_\infty^3}{3k_{\text{tnf}}^*(\rho C_p)_{\text{tnf}}}\left(\frac{1}{r^2}\frac{C_w}{r^2\alpha^2}g''\right) \\
&+ \frac{1}{(\rho C_p)_{\text{tnf}}}\frac{\sigma_{\text{tnf}}}{r^4}B_0^2 F^2 - \frac{1}{(\rho C_p)_{\text{tnf}}}2\frac{\alpha_1}{r^3}\left(\frac{F}{r}\frac{F'^2}{r^2} + 4\frac{F^3}{r^3}\right)
\end{aligned}
\tag{3.17}
$$

Equation (3.17) is multiplied by r^4, and after the necessary simplifications, the equation given below is obtained.

$$
\begin{aligned}
-2C_w F g = &\frac{k_{\text{tnf}}}{(\rho C_p)_{\text{tnf}}}\left(4C_w g + \frac{C_w}{\alpha^2}g''\right) + \frac{\mu_{\text{tnf}}}{(\rho C_p)_{\text{tnf}}}\left(4F^2 + (F')^2\right) \\
&+ \frac{16\sigma^* T_\infty^3}{3k_{\text{tnf}}^*(\rho C_p)_{\text{tnf}}}(4C_w g) + \frac{16\sigma^* T_\infty^3}{3k_{\text{tnf}}^*(\rho C_p)_{\text{tnf}}}\left(\frac{C_w}{\alpha^2}g''\right) \\
&+ \frac{\sigma_{\text{tnf}}}{(\rho C_p)_{\text{tnf}}}B_0^2 F^2 - \frac{1}{(\rho C_p)_{\text{tnf}}}2\frac{\alpha_1}{r^2}\left(F F'^2 + 4F^3\right)
\end{aligned}
\tag{3.18}
$$

The correlations between the terms $f(\eta)$ and $F(\theta)$ in equation (3.4) are used to obtain dimensionless velocity terms inside the energy equation. After this operation, the term $-2C_w \mathrm{U} rfg$ is moved to the right-hand side of the equation, and the following equation is derived.

$$\begin{aligned}
&\frac{k_{\mathrm{tnf}}}{(\rho C_p)_{\mathrm{tnf}}}\left(4C_w g+\frac{C_w}{\alpha^2}g''\right)+\frac{\mu_{\mathrm{tnf}}}{(\rho C_p)_{\mathrm{tnf}}}\left(4(\mathrm{U}rf)^2+(\frac{\mathrm{U}r}{\alpha}f')^2\right)\\
&+2C_w \mathrm{U} rfg+\frac{16\sigma^* T_\infty^3}{3k_{\mathrm{tnf}^*}(\rho C_p)_{\mathrm{tnf}}}(4C_w g)+\frac{16\sigma^* T_\infty^3}{3k_{\mathrm{tnf}^*}(\rho C_p)_{\mathrm{tnf}}}\left(\frac{C_w}{\alpha^2}g''\right)\\
&+\frac{\sigma_{\mathrm{tnf}}}{(\rho C_p)_{\mathrm{tnf}}}B_0^2\mathrm{U}^2r^2f^2-2\alpha_1\frac{\mathrm{U}^3 r}{(\rho C_p)_{\mathrm{tnf}}}\left(f(\frac{f'}{\alpha})^2+4(f)^3\right)=0
\end{aligned} \tag{3.19}$$

In the next step, equation (3.19) is multiplied by $\frac{(\rho C_p)_{\mathrm{tnf}}}{k_{\mathrm{tnf}}}\frac{\alpha^2}{C_w}$, and with the necessary arrangements, the following equation is obtained.

$$\begin{aligned}
&g''+4\alpha^2 g+\frac{\mu_{\mathrm{tnf}}}{k_{\mathrm{tnf}}}\frac{F_{max}^2}{C_w}\left(4\alpha^2 f^2+(f')^2\right)+2\frac{(\rho C_p)_{\mathrm{tnf}}\alpha^2 F_{max}}{k_{\mathrm{tnf}}}fg\\
&+\frac{16\sigma^* T_\infty^3}{3k_{\mathrm{tnf}^*}k_{\mathrm{tnf}}}\left(4\alpha^2 g\right)+\frac{16\sigma^* T_\infty^3}{3k_{\mathrm{tnf}^*}k_{\mathrm{tnf}}}\left(g''\right)+\frac{\alpha^2}{C_w}\frac{\sigma_{\mathrm{tnf}}}{k_{\mathrm{tnf}}}B_0^2F_{max}^2f^2\\
&-2\frac{\mathrm{U}^3 r}{k_{\mathrm{tnf}}}\frac{\alpha_1}{C_w}\left(f(f')^2+4\alpha^2 f^3\right)=0
\end{aligned} \tag{3.20}$$

As made in the conversion of momentum equations, the ratios between the blood and TNF nanofluid properties must be written in the equation to express the fluid properties relative to the base fluid. Finally, the coefficients are written in accordance with the dimensionless numbers, and the following equation is derived.

$$\begin{aligned}
&g''+4\alpha^2 g+\frac{\frac{\mu_{\mathrm{tnf}}}{\mu_f}}{\frac{k_{\mathrm{tnf}}}{k_f}}\frac{\alpha F_{max}^2}{C_w(C_p)_f}\frac{(\rho C_p)_f F_{max}}{k_f}\frac{\mu_f}{F_{max}\rho_f\alpha}\left(4\alpha^2 f^2+(f')^2\right)\\
&+2\frac{\frac{(\rho C_p)_{\mathrm{tnf}}}{(\rho C_p)_f}}{\frac{k_{\mathrm{tnf}}}{k_f}}\frac{(\rho C_p)_f F_{max}}{k_f}\alpha^2 fg+\frac{16\sigma^* T_\infty^3}{3k_{\mathrm{tnf}^*}k_{\mathrm{tnf}}}\left(4\alpha^2 g\right)+\frac{16\sigma^* T_\infty^3}{3k_{\mathrm{tnf}^*}k_{\mathrm{tnf}}}\left(g''\right)\\
&+\frac{\frac{\sigma_{\mathrm{tnf}}}{\sigma_f}}{\frac{k_{\mathrm{tnf}}}{k_f}}\frac{\alpha F_{max}^2}{C_w(C_p)_f}\frac{(\rho C_p)_f F_{max}}{k_f}\frac{\sigma_f}{\mu_f}B_0^2\frac{\nu_f}{F_{max}\alpha}\alpha^2 f^2\\
&+2\frac{1}{\frac{k_{\mathrm{tnf}}}{k_f}}\frac{\frac{-\alpha_1\mathrm{U}}{r\mu_f}\frac{F_{max}(\rho C_P)_{\mathrm{f}}}{k_{\mathrm{f}}}\frac{\alpha F_{max}^2}{C_w(C_p)_{\mathrm{f}}}}{\frac{F_{max}\alpha}{\nu_f}}\left(f(f')^2+4\alpha^2 f^3\right)=0
\end{aligned} \tag{3.21}$$

Similar to the conversion of momentum equations, the thermophysical properties within the coefficients and specific parameters are expressed using dimensionless numbers, and the ratios between the base fluid and TNF are replaced by R parameters.

$$\begin{aligned} & g'' + 4\alpha^2 g + \frac{R_1}{R_4}\frac{\mathrm{PrEc}}{\mathrm{Re}}\left(4\alpha^2 f^2 + f'^2\right) + 2\frac{R_3}{R_4}\mathrm{Pr}\alpha^2 fg \\ & + \mathrm{Rd}\left(4\alpha^2 g\right) + \mathrm{Rd}\left(g''\right) + \frac{R_5}{R_4}\frac{\mathrm{EcPrHa}^2}{\mathrm{Re}}\alpha^2 f^2 \\ & + 2\frac{1}{R_4}\frac{\mathrm{DePrEc}}{\mathrm{Re}}\left(ff'^2 + 4\alpha^2 f^3\right) = 0 \end{aligned} \tag{3.22}$$

The final adjustments necessary for the numerical solution are made, and the ODE representing the energy equation is obtained as follows:

$$\begin{aligned} & (1+\mathrm{Rd})g'' + 2\alpha^2\left(\frac{R_3}{R_4}\mathrm{Pr}f + 2 + 2\mathrm{Rd}\right)g + \frac{R_1}{R_4}\frac{\mathrm{PrEc}}{\mathrm{Re}}(4\alpha^2 f^2 + f'^2) \\ & + \frac{R_5}{R_4}\frac{\mathrm{EcPrHa}^2}{\mathrm{Re}}\alpha^2 f^2 + 2\frac{1}{R_4}\frac{\mathrm{DePrEc}}{\mathrm{Re}}\left(ff'^2 + 4\alpha^2 f^3\right) = 0 \end{aligned} \tag{3.23}$$

3.3 Conversion of Boundary Conditions

Equations (3.6) and (3.7), and similarity parameters are also employed to transform the boundary conditions to the dimensionless format.

$$\begin{aligned} & f(0) = 1, \quad f'(0) = 0, \quad g'(0) = 0 \\ & f(1) = -\frac{R_1}{R_2}\mathrm{s_v} f'(1), \quad g(1) = 1 - \mathrm{j_t} g'(1) \end{aligned} \tag{3.24}$$

3.4 Conversion of Engineering Parameters

Utilizing equations (3.6) and (3.7), and similarity parameters, the parameters can be articulated in a non-dimensional format below.

$$C_f\,\mathrm{Re} = R_1 f'(1), \qquad \alpha\,\mathrm{Nu} = -R_4(1+\mathrm{Rd})g'(1) \tag{3.25}$$

4. NUMERICAL SOLUTION AND CODE VALIDATION

In this section, the numerical approach has been examined, and the validation of the code has been performed using several studies from the literature.

4.1 Numerical Method

bvp4c is a MATLAB solver for boundary value problems (BVPs) of ordinary differential equations (ODEs). It differs from initial value problem (IVP) solvers such as ode45 or ode15s, which are used when ODEs are solved for an initial condition. bvp4c is used when the solution must be satisfied for more than one point, and typically for the boundaries of a region. This renders bvp4c very useful in fields such as heat conduction, fluid mechanics, structural mechanics, and quantum mechanics, where physical behaviors are governed by differential equations with boundary constraints.

The bvp4c function is constructed based on collocation techniques and employs a finite difference technique to solve for an approximation of the solution. Specifically, it employs a three-stage Lobatto IIIa formula, an implicit high-accuracy Runge-Kutta method [93–95]. The Lobatto IIIa formula has been chosen because of its accuracy and stability properties of high order. The formula is also most appropriate for stiff problems and allows for a numerical solution that is accurate as well as smooth [96–98]. This method provides C1 continuity, and the solution is guaranteed to be well-behaved. Perhaps the greatest draw of bvp4c is its adaptive mesh refinement, which automatically alters the number and position of the mesh points to improve accuracy while maintaining computational efficiency.

The function bvp4c provides initial mesh points and solution estimates. It is a very good solver for stiff problems, i.e., when the solutions vary quickly or have steep gradients. The initial solution is compared to a higher-order approximation to estimate errors in mesh points. The error estimation method is based on a defect control approach, which offers reliability in the solution. Using this error estimate, the solver adaptively modifies the mesh: it introduces points in regions of large error and discards

points in regions where the solution is smooth. Mesh adaptation is crucial for boundary layer or singularity problems, where the standard approaches may break down. This adaptive approach ensures computational efficiency while preserving high accuracy. More points are added where the solution is changing more quickly, and fewer points are kept where the solution is smoother. The solver also uses a collocation approach to approximate the solution as piecewise polynomials. The solver generates accurate and smooth approximations to intermediate values between mesh points by high-order polyn interpolation. This interpolation renders the solution not only accurate at mesh points, but also continuous in the domain. This procedure is repeated until the solution is as accurate as desired. The convergence criteria are controlled by user-prescribed tolerances, allowing one to have flexible control over the accuracy of the solution. As discussed in the article by asdadsd et al., some of the advantages of bvp4c are adaptive mesh refinement for accuracy, robust treatment of singularities, and highly accurate solutions.

To find the solution to the problem, the PDEs describing the physical system, as equations (2.1)-(2.4), were first derived. These were then reduced to ODEs using similarity variables. To solve them numerically, the dimensionless higher-order ODEs and their boundary conditions must be in first-order form. This is such that a high-order ODE must be rewritten as a system of first-order ODEs. Because the boundary value problem solvers require an initial estimate of the solution, bvpinit is used to provide an initial mesh and an initial guess. It doesn't necessarily have to be an accurate guess, but it should be close enough in order to help bvp4c converge. In contrast to other available methods, such as HAM, Adomian decomposition method, and several other similar methods, the bvp4c method is more trustworthy [97]. We are using the bvp4c solver to solve the dimensionless nonlinear ODEs because its convergence rate is better than that of other methods. The initial guess for the bvp4c solver must satisfy the boundaries. With the boundary conditions, the ODE system, and the initial guess, bvp4c can now solve the problem. First, the conversion of ODEs that comprise the momentum and energy equations into first-order is completed.

$$\left.\begin{array}{c} f = y_1, \quad f' = y_2, \quad f'' = y_3, \quad f''' = y_3' \\ g = y_4, \quad g' = y_5, \quad g'' = y_5' \end{array}\right\} \tag{4.1}$$

$$
\begin{aligned}
y_3' =& (-4\alpha^2 y_2 - 2\frac{R_2}{R_1}\,\mathrm{Re}\,\alpha y_1 y_2 + \frac{R_5}{R_1}\,\mathrm{Ha}^2\,\alpha^2 y_2 + \mathrm{Dr}_1\,\mathrm{Re}\,\alpha y_2 \\
&+ 2\frac{R_2}{R_1}\,\mathrm{Dr}_2\,\mathrm{Re}\,\alpha y_1 y_2 - 16\frac{\mathrm{De}}{R_1}\alpha^2 y_1 y_2)/(1+4\frac{\mathrm{De}}{R_1}y_1)
\end{aligned} \tag{4.2}
$$

$$
\begin{aligned}
y_5' =& (-2\alpha^2\left(\frac{R_3}{R_4}\,\mathrm{Pr}\,y_1 + 2 + 2\mathrm{Rd}\right)y_4 - \frac{R_1}{R_4}\frac{\mathrm{PrEc}}{\mathrm{Re}}\left(4\alpha^2 y_1^2 + y_2^2\right) \\
&- \frac{R_5}{R_4}\frac{\mathrm{EcPrHa}^2}{\mathrm{Re}}\alpha^2 y_1^2 - \frac{2\,\mathrm{De}\,\mathrm{Pr}\,\mathrm{Ec}}{\mathrm{Re}\,R_4}\left(4\alpha^2 y_1^3 + y_1 y_2^2\right))/(1+\mathrm{Rd})
\end{aligned} \tag{4.3}
$$

Secondly, the process of converting the ODEs that define the boundary conditions into first-order form is completed.

$$
\begin{aligned}
&y_1(0) = 1, \quad y_2(0) = 0, \quad y_5(0) = 0 \\
&y_1(1) = -\frac{R_1}{R_2}\mathrm{s_v}\,y_2(1), \quad y_4(1) = 1 - \mathrm{j_t}\,y_5(1)
\end{aligned} \tag{4.4}
$$

4.2 Code Validation

Solutions for converging and diverging channels, which represent physical conditions, were obtained using the bvp4c technique. To validate the accuracy of the solutions, they were compared with the results of previous studies in the literature. Since the present study examines the effects of different physical conditions, the results obtained using the bvp4c code were compared with numerical studies that investigated similar effects. During these comparisons, the bvp4c code was executed under the same physical conditions as the reference studies. The validation of the bvp4c code was performed for three different cases. These include: (1) Jeffrey-Hamel flow with shrinking and stretching walls, which is not included in this study, (2) Jeffrey-Hamel flow considering the effects of thermal radiation, (3) Jeffrey-Hamel flow using blood as the base fluid.

Initially, the validation of the bvp4c code was analyzed for a study involving convergent/divergent channels with shrinking and stretching walls. Table 4.1 compares the $f''(0)$ values obtained from the previous study conducted by Turkyilmazoglu [41] with those calculated using the bvp4c code. Dogonchi and Ganji [72] investigated the effect of thermal radiation on nanofluid flow in a convergent/divergent channel with shrinking and stretching walls. The validation of the code is also performed for the thermal radiation case by using the results obtained by Dogonchi and Ganji [72]. Figure 4.1 presents the $g(\eta)$ obtained by Dogonchi and Ganji [72] and those obtained from the present study's code.

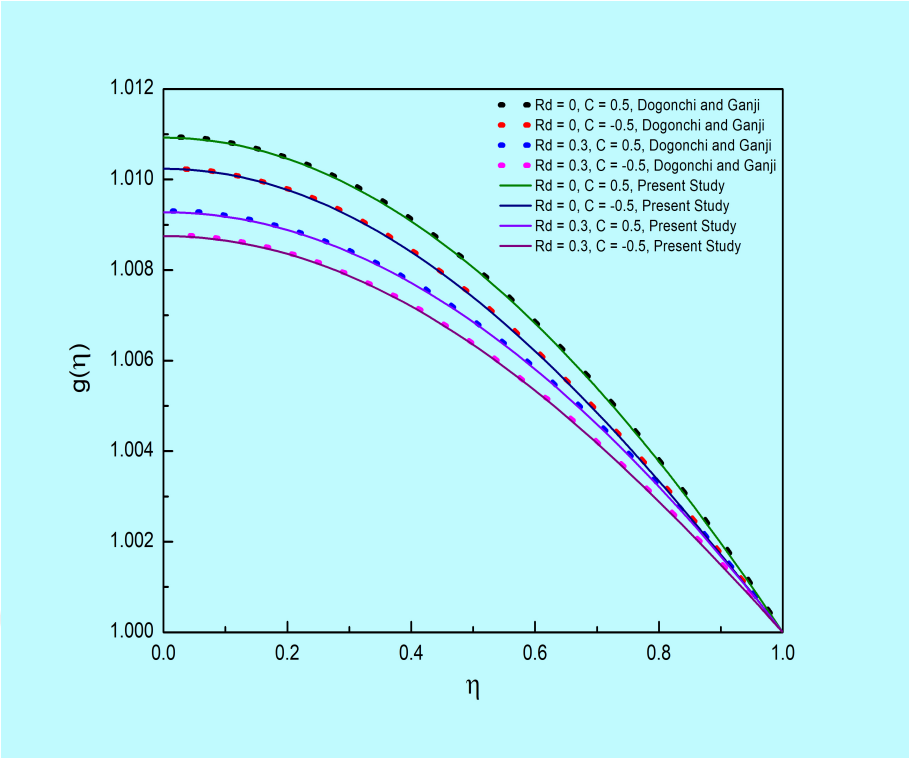


Figure 4.1a : The $g(\eta)$ values for radiation parameters of 0 and 0.3, and for shrinking/stretching parameters of –0.5 and 0.5.

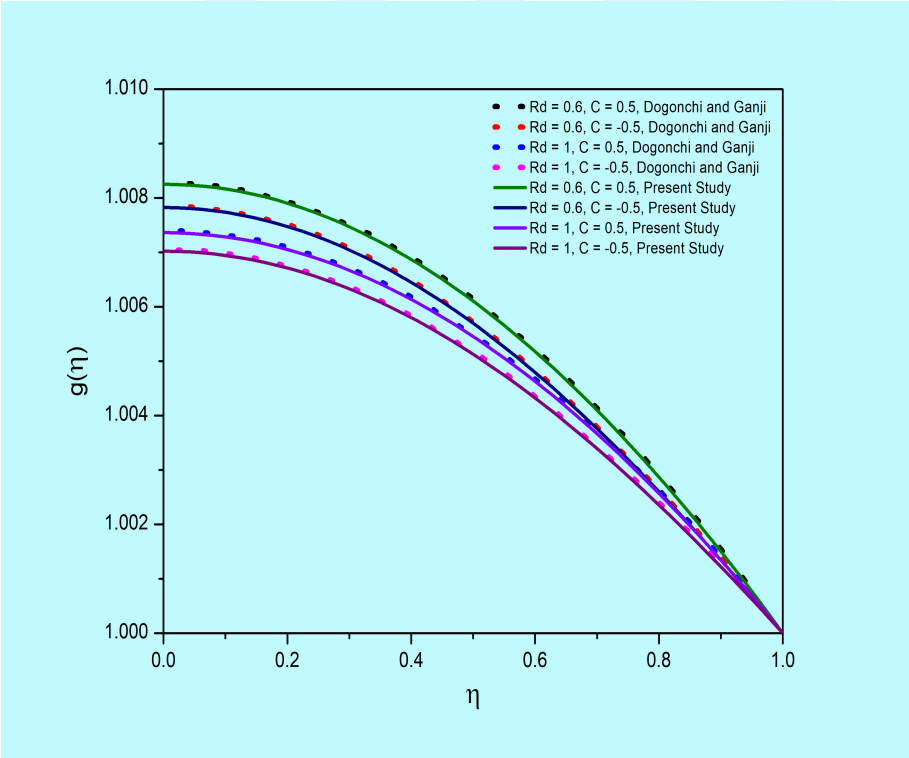


Figure 4.1b : The $g(\eta)$ values for radiation parameters of 0.6 and 1, and for shrinking/stretching parameters of –0.5 and 0.5.

Figure 4.1 : A comparison of the present $g(\eta)$ values with those reported in the study conducted by Dogonchi and Ganji [72], considering different radiation and stretching/shrinking parameters.

Table 4.1 : The $f''(0)$ values obtained in the present study and those reported by Turkyilmazoglu [41], by excluding nanoparticles at various α angles and Reynolds numbers.

	Re	Current Study	Turkyilmazoglu [41]
Divergent Channel	20	2.52719	2.52719
(α=+5°)	60	3.94214	3.94214
	100	5.86916	5.86916
Convergent Channel	30	1.41369	1.41369
(α=-5°)	70	0.89347	0.89347
	100	0.64017	0.64017

In the present study, blood was used as the base fluid to prepare the nanofluid. Dinarvand et al. [82] investigated the effect of Ag and TiO_2 nanoparticles on blood flow in convergent and divergent channels by calculating engineering parameters. Since the bvp4c code is not validated for blood flow cases, the results of Dinarvand et al. [82] are used for comparison. Taking into account the velocity slip and temperature jump boundary conditions, the computed value of $g(\eta)$ at Re = 30 and α = 5° was -0.319297854, while the corresponding value reported in the original study was -0.319297. Based on the comparisons for three cases, it is observed that the bvp4c code produces values close to those from previous studies, which indicates its high accuracy.

5. RESULTS AND DISCUSSION

In this research, the Jeffrey-Hamel flow in a non-Darcy porous medium with a magnetic medium, considering velocity slip and temperature jump at the wall, was investigated with nonlinear thermal radiation. The effects of the shape of nanoparticles on thermal conductivity and, consequently, heat transfer have been investigated. A second-grade non-Newtonian model has been utilized, as the base fluid is blood. The analysis has been carried out for low (Re = 1) and high (Re = 50) Reynolds numbers. The effects of various physical parameters, including the Deborah number, Hartmann number, Darcy parameter, Forchheimer parameter, slip velocity coefficient, jump-temperature parameter, Brinkmann number, shape parameter, inclination angle, and volume concentration, on the flow have been investigated.

5.1 Investigation of Velocity and Temperature Distributions

In this section, the effects of various dimensionless numbers and parameters on the velocity and temperature distributions are investigated. During these investigations, which are carried out based on the figures, the parameters studied varied while the other dimensionless numbers and parameters were kept constant. The constant values used are: $\alpha = \pm 5°$, De = 0.1, $\mathrm{Dr}_1 = 0.5$, $\mathrm{Dr}_2 = 0.5$, Ec = 0.1, Ha = 10, Pr = 21, Rd = 0.1, $s_p = 3$, $s_v = 0.1$, $j_t = 0.1$, $\Phi_1 = \Phi_2 = \Phi_3 = 0.02$. In the figures, the converging channel is represented by a dotted line ($\cdots$), and the diverging channel by a dashed line ($---$). First, the effect of the inclination angle on velocity distribution within the channel was analyzed for both high and low Reynolds numbers. During the investigation, three different channel angles ($\alpha = \pm 3°, \pm 5°, \pm 7°$) were used. Positive angles represent a diverging channel, while negative angles represent a converging channel. Figures 5.1a and 5.1b illustrate the effect of the inclination angle on velocity distribution for low and high Reynolds numbers, respectively. At low Reynolds numbers, changing the inclination angle has no significant impact on the velocity distribution in either converging or diverging channels. For both channel types, as the absolute inclination angle increases, velocity values increase marginally. In the high

Reynolds number case, it was observed that the inclination angle has little effect on the velocity distribution in the diverging channel flow. However, in the converging flow type at high Reynolds numbers, velocity increases as the inclination angle increases.

Figures 5.2a and 5.2b illustrate the effect of the inclination angle on temperature distribution for low and high Reynolds numbers, respectively. Unlike velocity distributions in converging/diverging channels, the temperature distribution in both channels is affected by the inclination angle. As defined in the boundary conditions at the centerline, the peak value of temperature occurs at the channel center. This temperature value increases as the absolute inclination angle increases. Channel type (converging or diverging) for temperature distribution does not have any effect at low Reynolds numbers. Like low Reynolds numbers, the inclination angle also significantly affects temperature distribution for high Reynolds numbers. Furthermore, the temperature values at low Reynolds numbers are higher than the temperature values at high Reynolds numbers. However, unlike low Reynolds conditions, there is a difference in temperature distribution between the converging and diverging channels when the Reynolds number is high. Temperature values in the converging channel are slightly higher than temperature values in the diverging channel. Further, with a rise in the absolute inclination angle, the temperature values also increase.

While considering the effect of the porous medium, the impacts of two parameters are analyzed separately, keeping one parameter constant while examining the other. The effects of the Darcy term and the non-Darcy Forchheimer parameter are taken into account, and their influence on velocity and temperature profiles is investigated.

Figure 5.3a illustrates the impact of four different Darcy parameters on velocity distributions at low Reynolds numbers. From the figure, it can be seen that for the low Reynolds case, the velocity distributions do not depend on the Darcy parameter for both the diverging and converging channels, and the velocity profiles are the same in all the cases. As observed from the velocity profiles of previous parameters, the influence of the Reynolds number is clear from Figure 5.3. The large influence of the Reynolds number on the velocity distributions is also established in other research in the literature. In the high Reynolds case, momentum transfer increases with an increasing Darcy parameter. As a result, velocity values also rise due to the enhanced momentum transfer in the divergent channel. Examining the non-dimensional parameters in

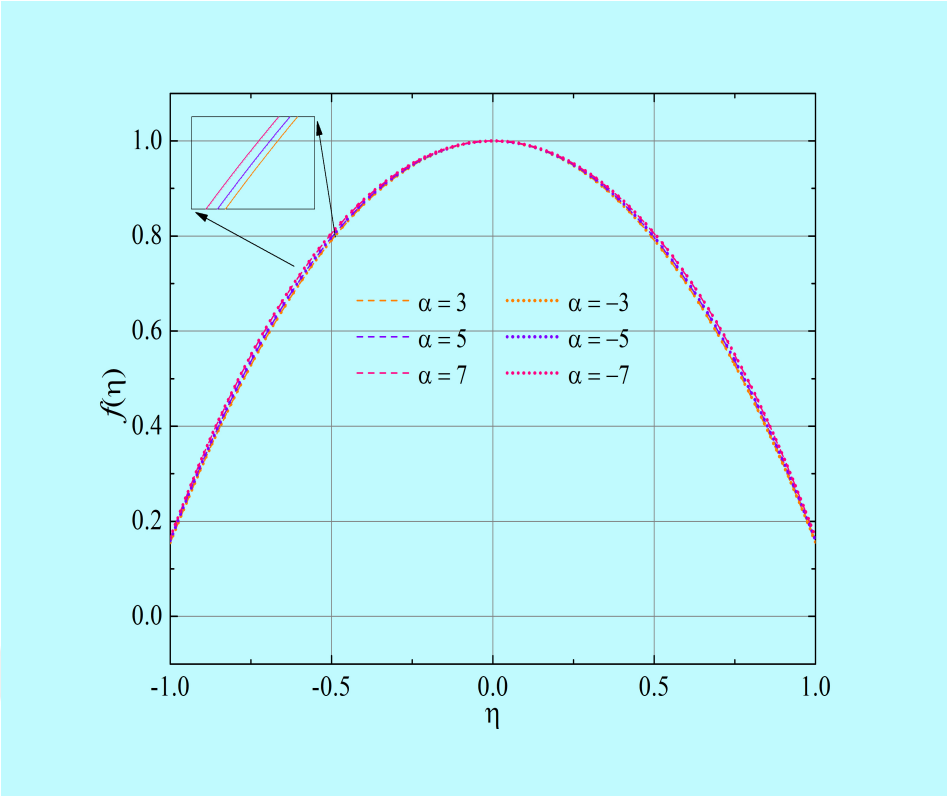


Figure 5.1a : Effect on velocity profile at low Reynolds number.

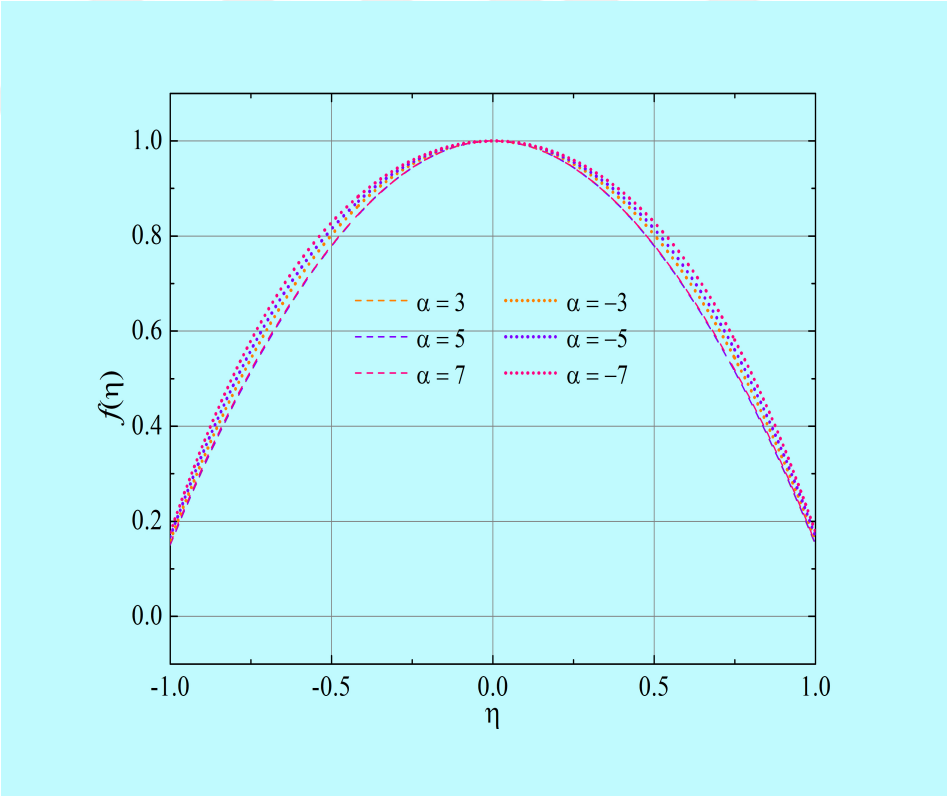


Figure 5.1b : Effect on velocity profile at high Reynolds number.

Figure 5.1 : Impact of different channel inclination angles on the velocity distributions under low and high Reynolds number conditions in converging and diverging geometries.

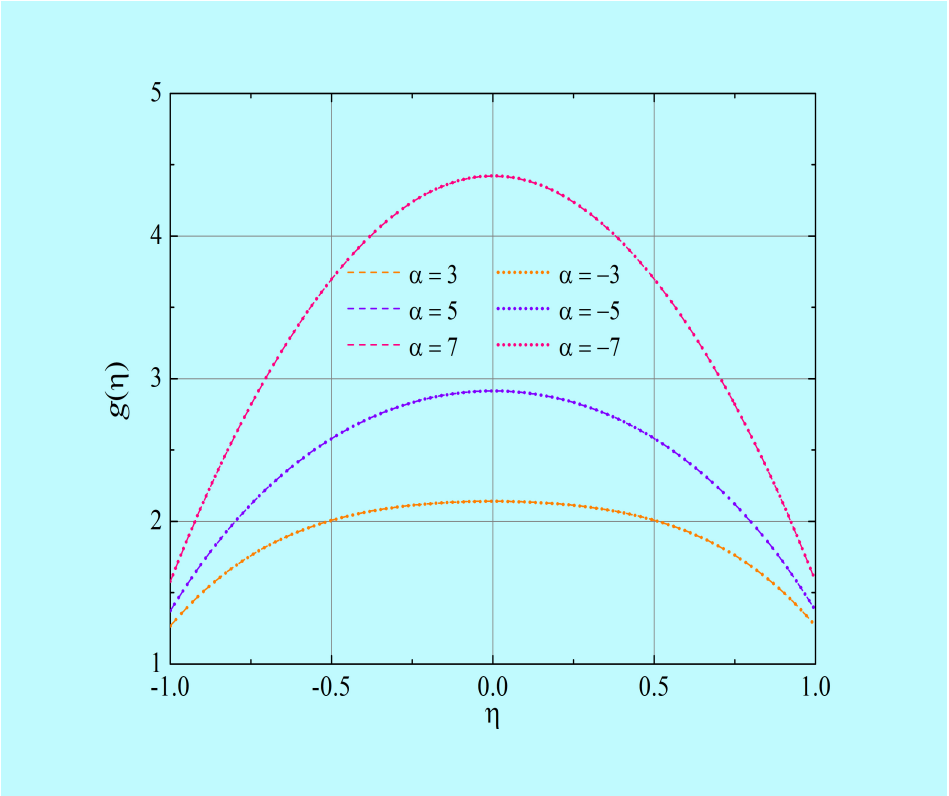


Figure 5.2a : Effect on temperature profile at low Reynolds number.

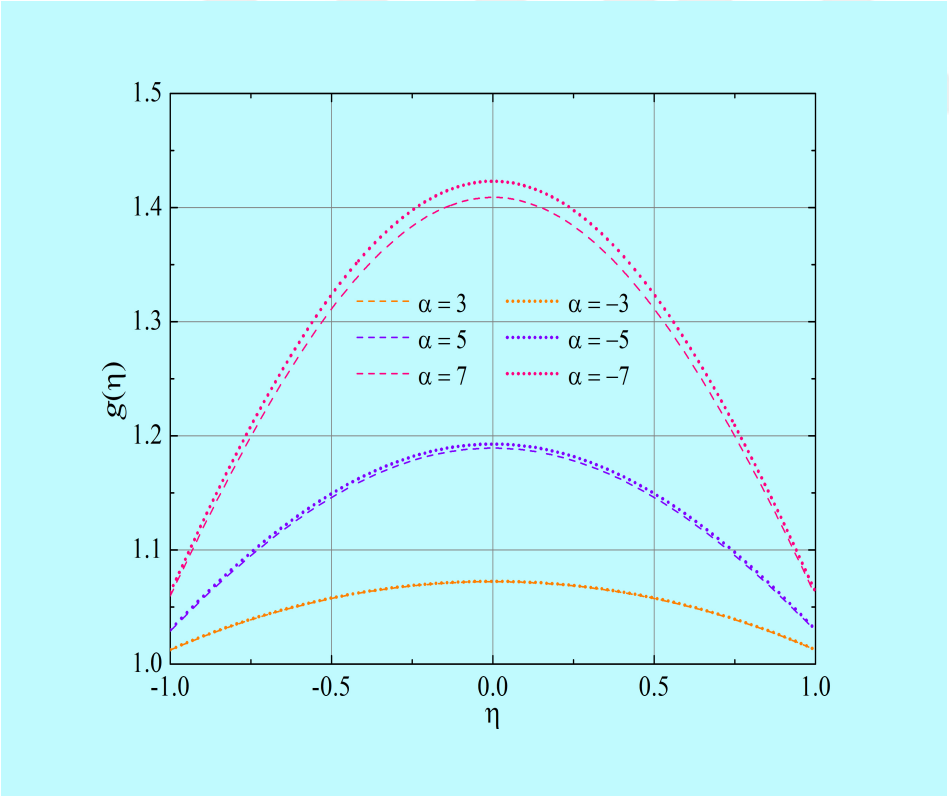


Figure 5.2b : Effect on temperature profile at high Reynolds number.

Figure 5.2 : Impact of different channel inclination angles on the temperature profiles under low and high Reynolds number conditions in converging and diverging geometries.

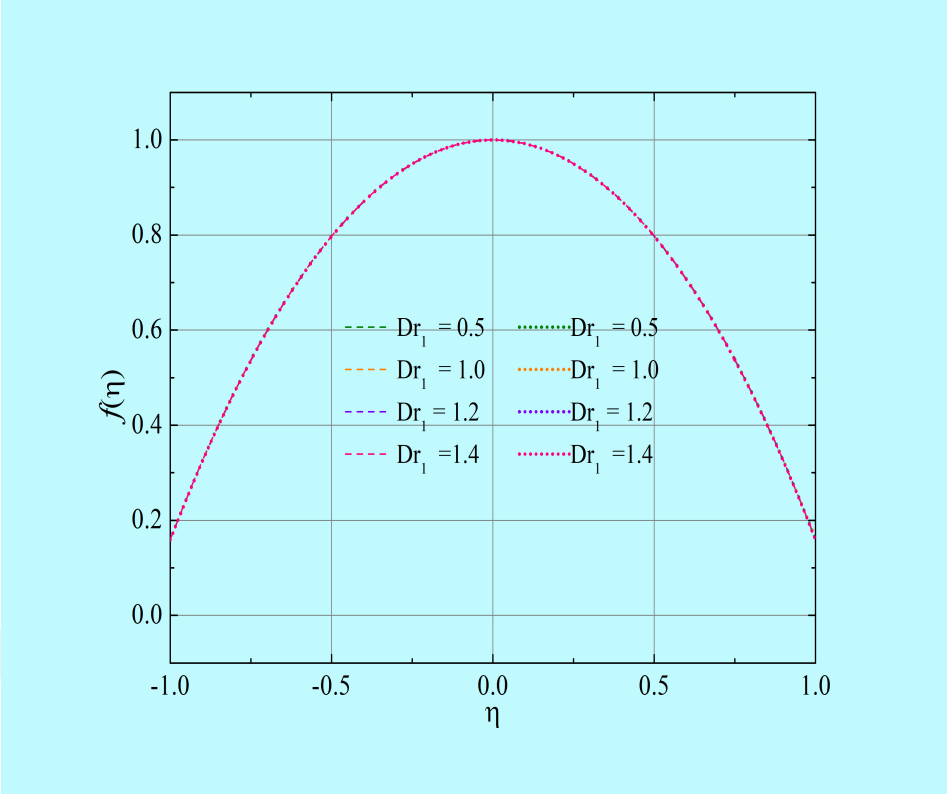


Figure 5.3a : Effect on velocity profile at low Reynolds number.

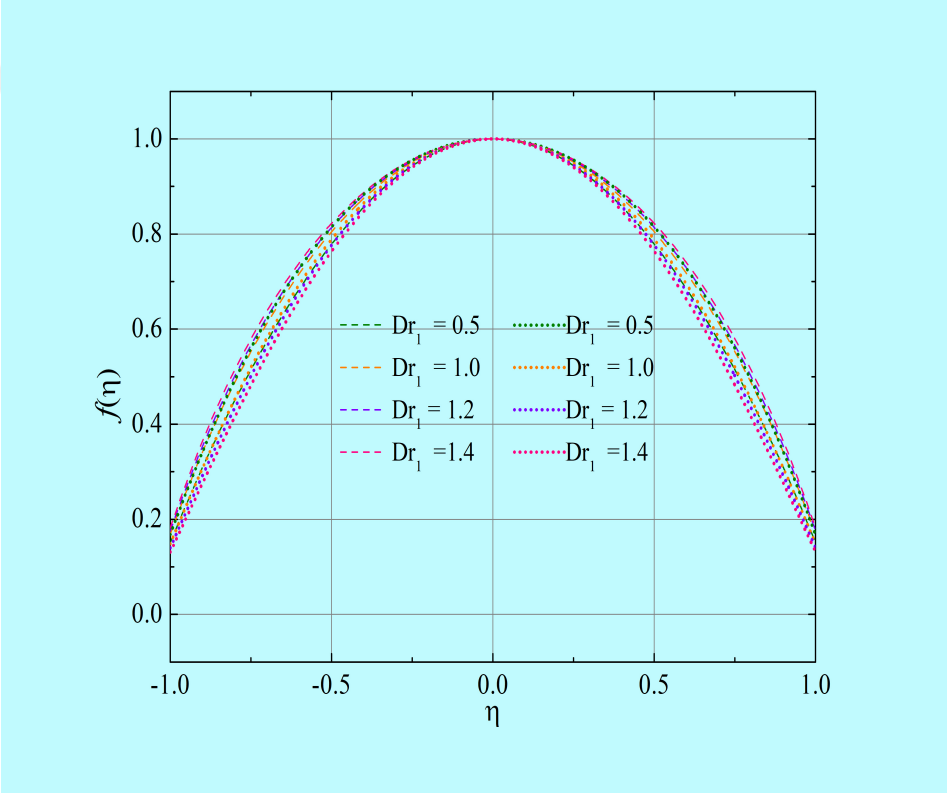


Figure 5.3b : Effect on velocity profile at high Reynolds number.

Figure 5.3 : Impact of Dr_1 parameter on the velocity distributions under low and high Reynolds number conditions in converging and diverging geometries.

equation 3.6, it is observed that the Darcy parameter is directly proportional to the porosity of the porous medium and inversely proportional to its permeability. The ratio of porosity to permeability is a crucial factor influencing the flow. In a diverging channel, with the increase in this ratio, the near-wall flow rate also increases. Moreover, momentum transfer in the tangential direction increases. As a result of these increases, a more fuller velocity profile is obtained. An increase in the permeability of the porous medium reduces the resistance to flow, while its decrease enhances the resistance to flow. Conversely, in the convergent channel, velocity values decrease as the Darcy parameter grows in the high Reynolds case. Because the flow resistance generated by the porous medium is effective, the velocity values decrease. The fluctuations of the velocity profile may be studied by considering the pressure gradient in the channel. In the converging channel, there exists a negative pressure gradient. The Darcy parameter reduces the absolute negative pressure gradient because it produces a positive pressure gradient. The effect slows down the velocity in the converging channel. The opposite effect is felt in the diverging channel. In the diverging channel, where there is a positive pressure gradient, the Darcy parameter reduces the positive pressure gradient. As a result, the velocity accelerates. Compared to low Reynolds numbers, the influence of the Darcy parameter is observed in both channel types differently.

Figures 5.4a and 5.4b illustrate the effect of the Darcy parameter on temperature distribution for low and high Reynolds numbers, respectively. As in its effect on the velocity profile, in the case of low Reynolds numbers, the Darcy parameter has no effect on the values of temperature for converging/diverging channels. In the case of high Reynolds numbers, there is an effect of the Darcy parameter on the values of temperature. However, it is evident that the impact of the Darcy parameter on temperature is very minimal. The increase in the Darcy parameter yields different outcomes for the two types of channels. For the convergent channel, temperature decreases as the Darcy parameter increases. For the divergent channel, temperature increases with an increasing Darcy parameter. This effect on the temperature difference due to the Darcy parameter is observed near the channel center, while near the walls, the difference is roughly zero. The changes in the temperature are due to the dissipation effects. The higher velocity gradients produce more pronounced dissipation effects, and these enhance the temperature value.

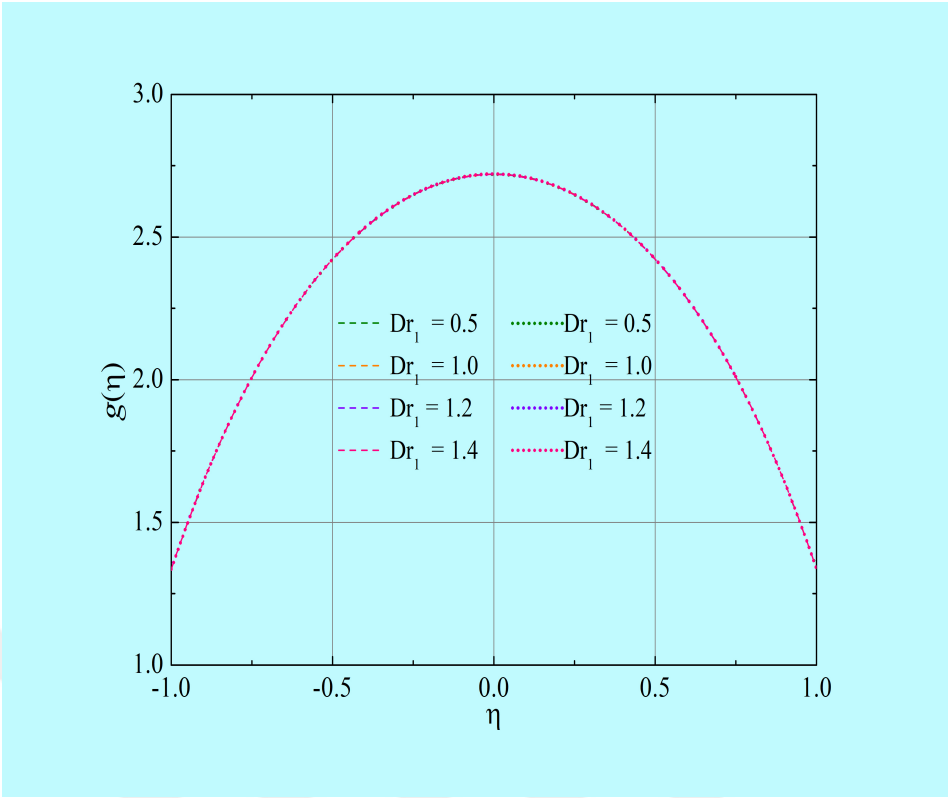


Figure 5.4a : Effect on temperature profile at low Reynolds number.

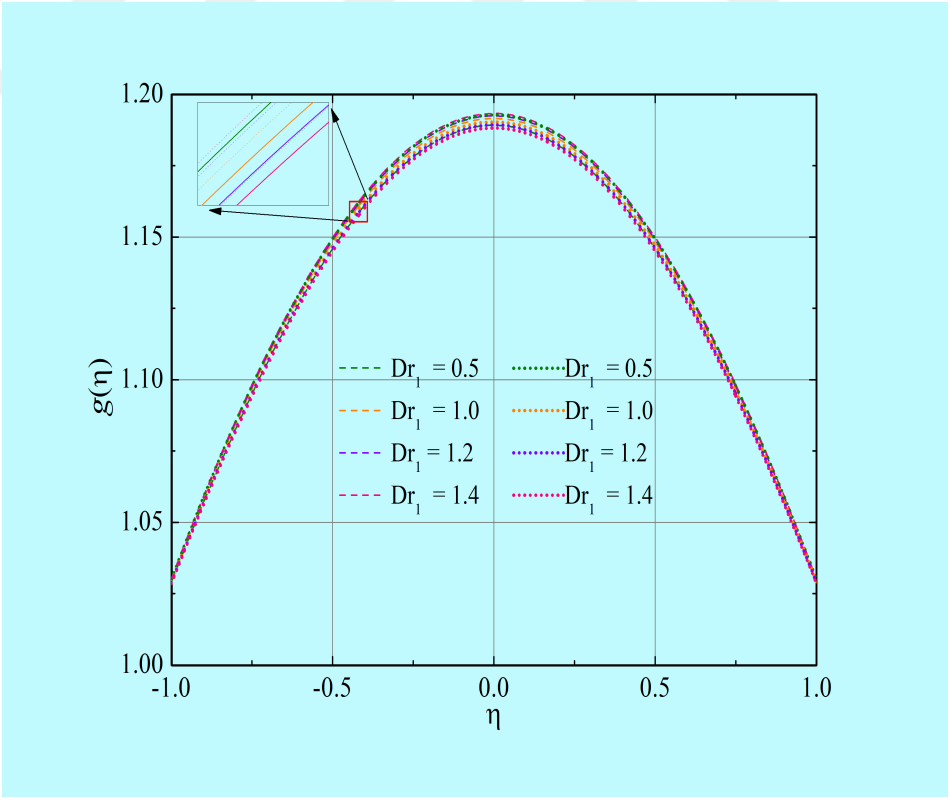


Figure 5.4b : Effect on temperature profile at high Reynolds number.

Figure 5.4 : Impact of Dr_1 parameter on the temperature profiles under low and high Reynolds number conditions in converging and diverging geometries.

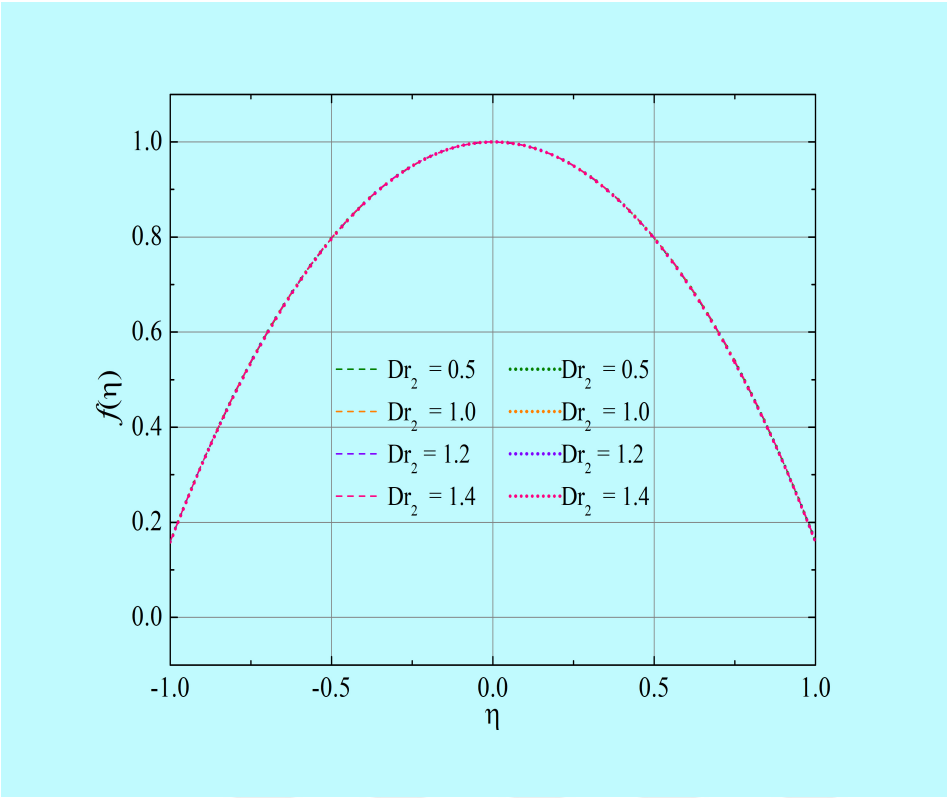


Figure 5.5a : Effect on velocity profile at low Reynolds number.

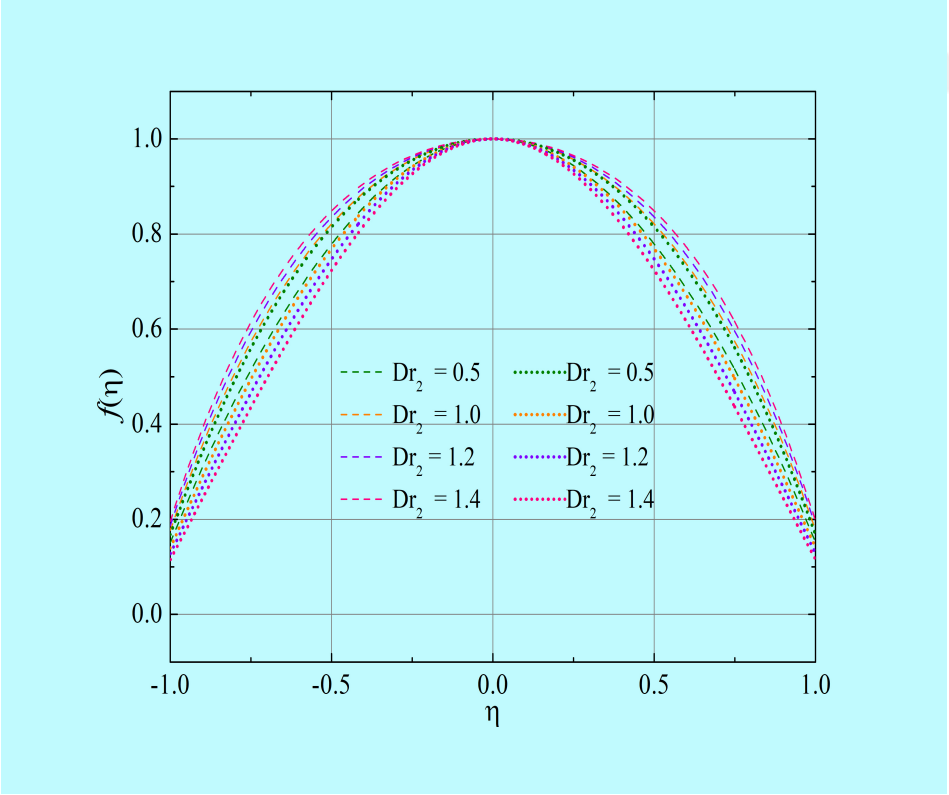


Figure 5.5b : Effect on velocity profile at high Reynolds number.

Figure 5.5 : Impact of Dr_2 parameter on the velocity distributions under low and high Reynolds number conditions in converging and diverging geometries.

Figures 5.5a and 5.5b display the effect of the Forchheimer parameter on velocity distribution at low and high Reynolds numbers, respectively. The analysis is carried out with four different values for the Forchheimer parameter, the same values as the Darcy parameter. Similar to the Darcy parameter, the Forchheimer parameter has no influence on velocity distribution in converging and diverging channels at low Reynolds numbers. However, for high Reynolds numbers, the Forchheimer parameter influences velocity distribution in diverging and converging channels differently. As the Forchheimer parameter increases, velocity values increase in the diverging channel, whereas velocity values decrease in the converging channel. With a comparison of the effect of Forchheimer and Darcy parameters on velocity distribution for high Reynolds numbers, the Forchheimer parameter is observed to have a stronger effect. Figures 5.6a and 5.6b present the effect of the Forchheimer parameter on temperature distribution for low and high Reynolds numbers, respectively. From the figures, it is evident that the Forchheimer parameter has no effect on temperature for low Reynolds numbers. But at high Reynolds numbers, the increase in the Forchheimer parameter results in the rise of temperature in the diverging channel, while the temperature reduces in the converging channel. Similar to the Darcy parameter, the variation of the temperature change happens mostly around the middle of the channel. This variation in velocity and temperature profiles is caused by the influence of the inertial term in the momentum equation.

The non-Newtonian effects of blood are investigated using the second-grade model, and the impact of the non-Newtonian parameter, namely the Deborah number, on the flow is examined, as different Deborah numbers correspond to different viscoelastic properties. Figures 5.7a and 5.7b show the effect of the Deborah number on velocity profiles for Jeffrey-Hamel flow for low and high Reynolds numbers, respectively. In the low Reynolds case, the Deborah number has minimal effect on the velocity values for both channel flow types. As observed in the figures, an increase in the Deborah number reduces the velocity values for both flow types. In the high Reynolds case, the velocity in the divergent channel increases as the Deborah number rises, though this increase is quite small. Compared to the case with a Newtonian fluid, the maximum increase of 0.8% is observed at a Deborah number of 0.3. In the high Reynolds case, a more significant change is observed in the converging channel in comparison with the other three cases. As the Deborah number increases, the velocity decreases. The

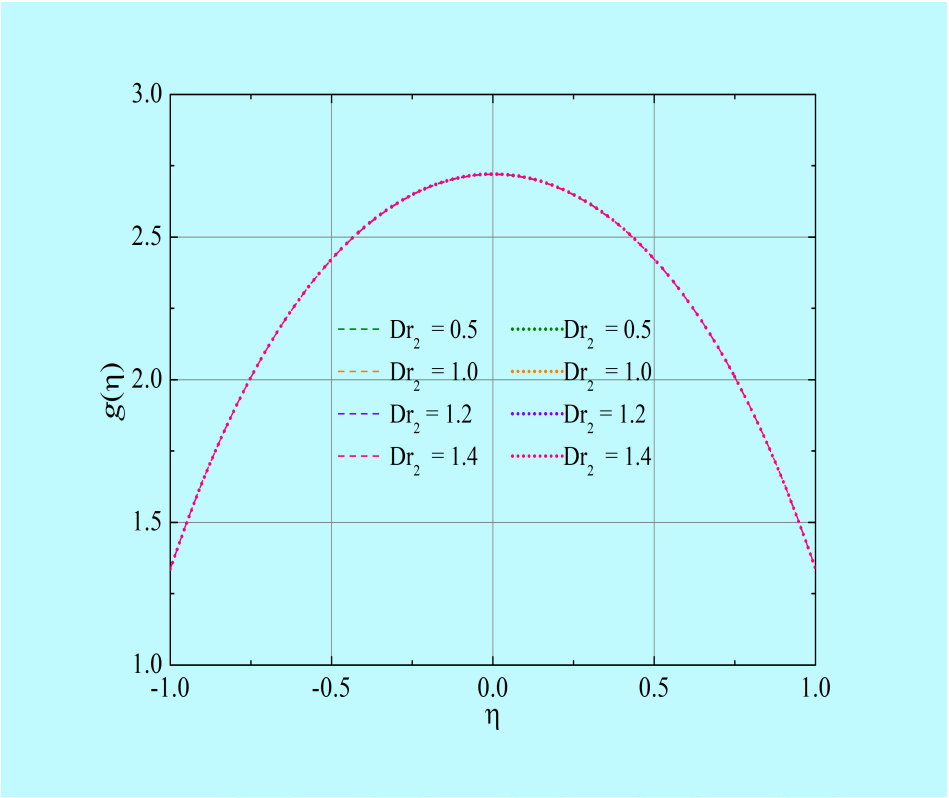


Figure 5.6a : Effect on temperature profile at low Reynolds number.

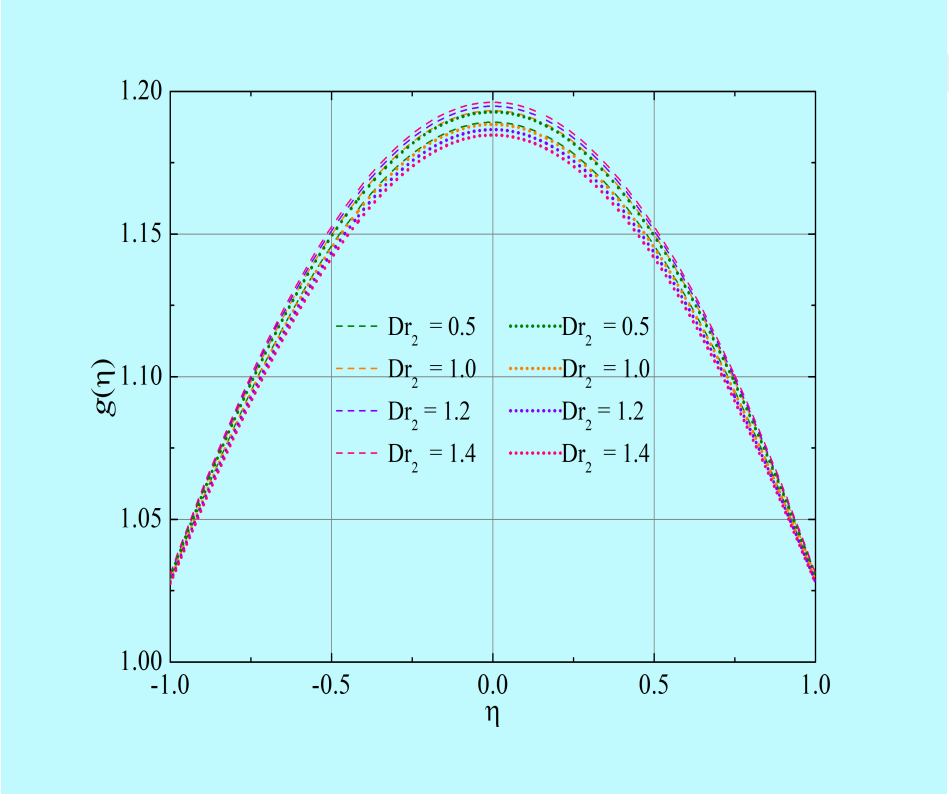


Figure 5.6b : Effect on temperature profile at high Reynolds number.

Figure 5.6 : Impact of Dr_2 parameter on the temperature profiles under low and high Reynolds number conditions in converging and diverging geometries.

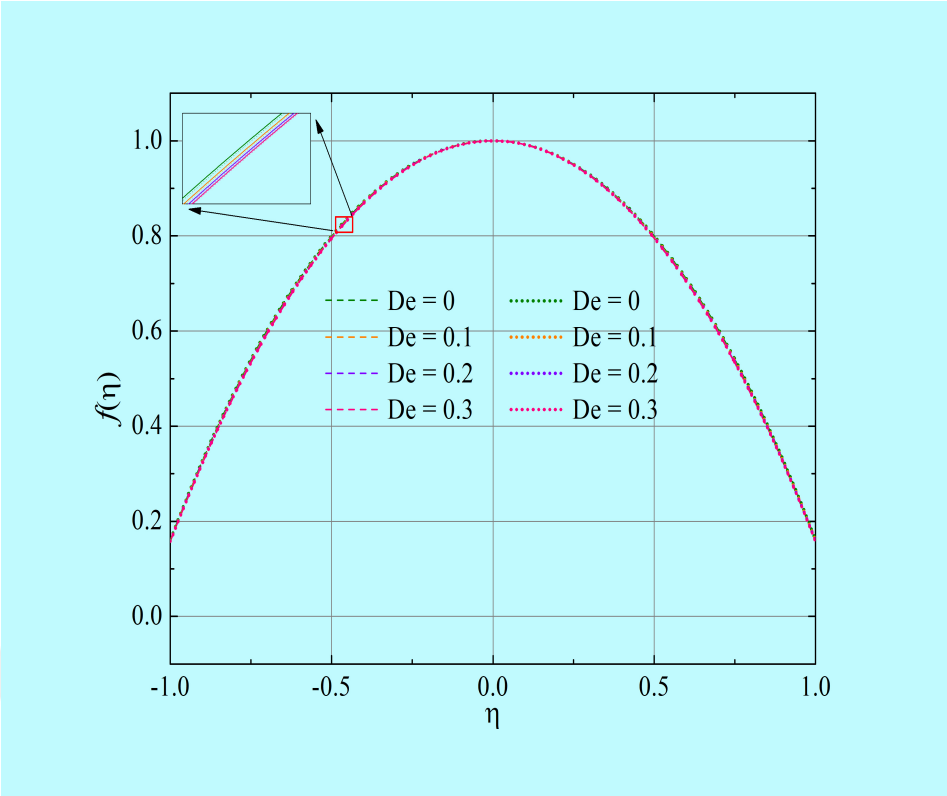


Figure 5.7a : Effect on velocity profile at low Reynolds number.

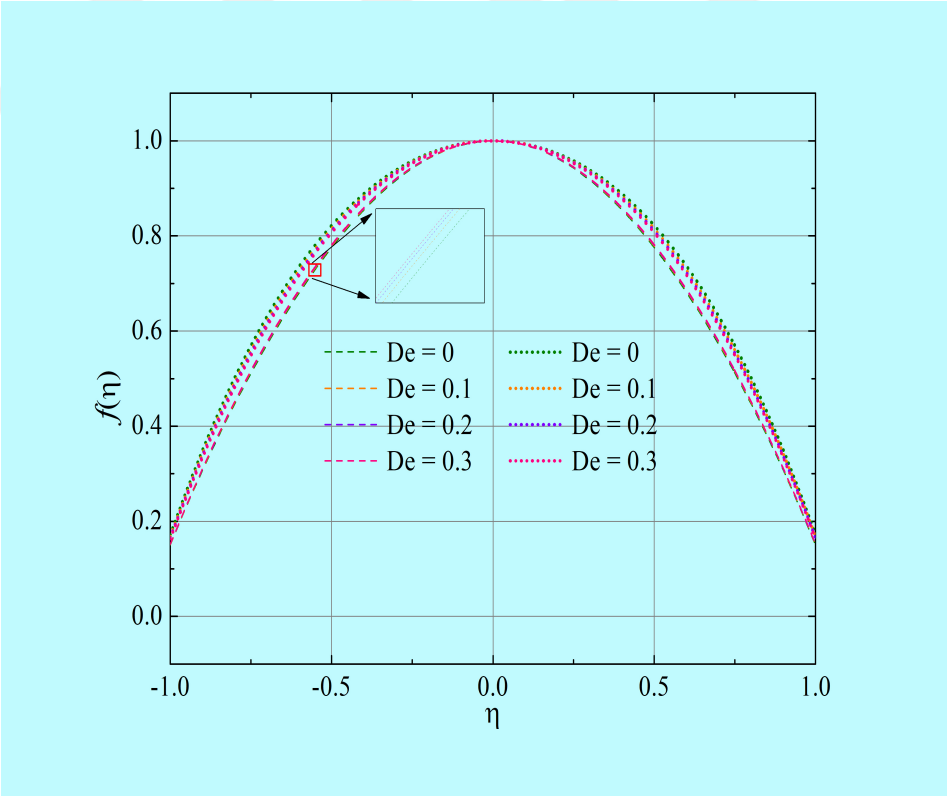


Figure 5.7b : Effect on velocity profile at high Reynolds number.

Figure 5.7 : Impact of Deborah number on the velocity distributions under low and high Reynolds number conditions in converging and diverging geometries.

maximum change is approximately 3% compared to the case with a Newtonian fluid. Based on this information, the use of a Newtonian fluid can be considered applicable over a wide range of Reynolds numbers.

Figures 5.8a and 5.8b illustrate the effect of the Deborah number on the temperature distribution for converging and diverging types of channel flow at low and high Reynolds numbers, respectively. As can be seen from the figures, temperature values are considerably influenced by the Deborah number. However, temperature values do not vary according to the type of channel (converging or diverging channels). As in all other comparisons, the temperatures in the low Reynolds case are higher than in the high Reynolds case. With an increase in the Deborah number, there is an increase in temperature, and this increase is observed in regions close to the center.

Figures 5.9a and 5.9b demonstrate the influence of the slip-velocity parameter on velocity distribution at low and high Reynolds numbers, respectively. The velocity magnitudes near the wall are increased with a greater value of the slip-velocity parameter. This is equivalent to a greater particle density in those regions. For the low Reynolds scenario, quite similar velocity profiles are obtained for both flow types of the channel. For the high Reynolds case, the velocity values inside the convergent channel are larger than those inside the divergent channel. In addition, for both cases, the velocity values increase as the slip-velocity parameter increases. Figures 5.10a and 5.10b display the influence of the slip-velocity parameter on temperature profiles for low and high Reynolds numbers, respectively. For the low Reynolds case, the slip-velocity parameter highly influences temperature values. Higher slip-velocity parameters reduce deformation near the wall, thus dissipating less. Therefore, the temperature gradient as well as the jump-temperature effect in this position reduces. For the low Reynolds case, the temperature reduces with the rise in the slip-velocity parameter. However, for the high Reynolds case, temperature increases with the rise in the slip-velocity parameter. The peak temperature value experiences an increase of 0.15% for a slip-velocity parameter value of 0.3.

Figures 5.11a and 5.11b illustrate the effect of nanoparticle geometry on velocity profiles for two different channel types at low and high Reynolds numbers, respectively. As seen from the figures, the geometry of the nanoparticles has no significant effect at low Reynolds numbers; for both channel types, the velocity profiles

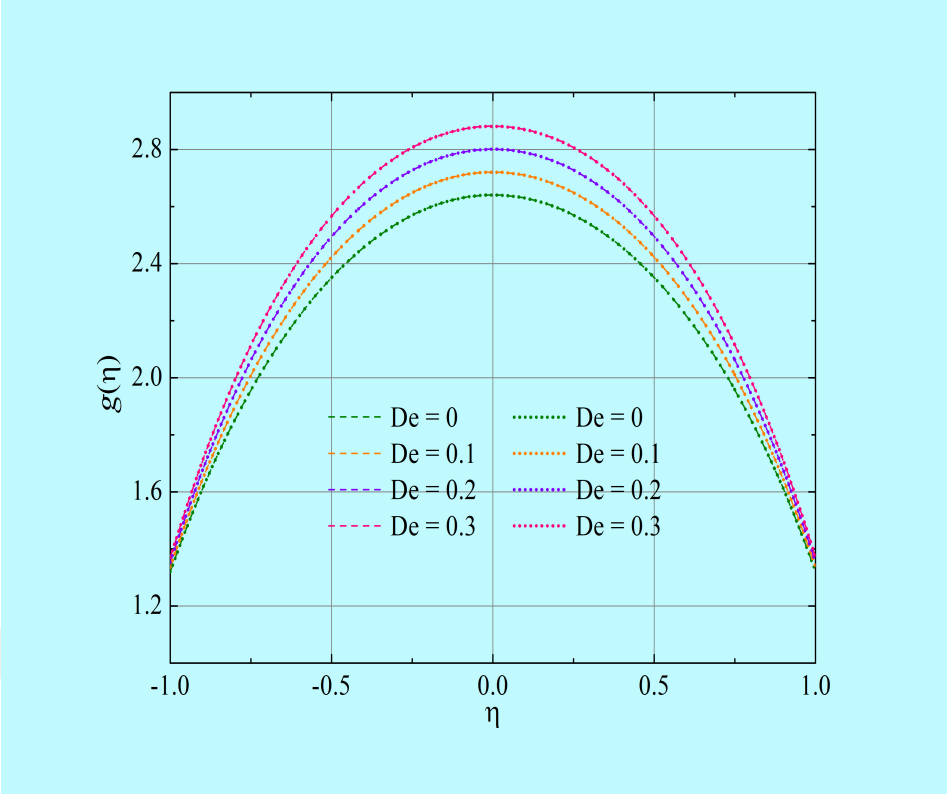


Figure 5.8a : Effect on temperature profile at low Reynolds number.

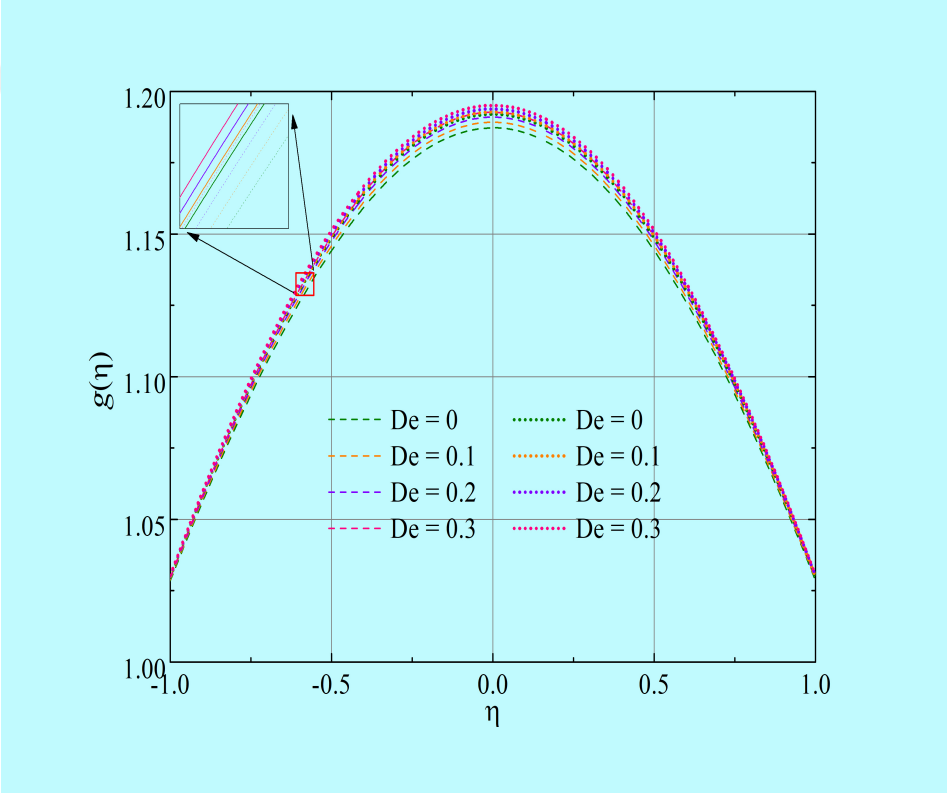


Figure 5.8b : Effect on temperature profile at high Reynolds number.

Figure 5.8 : Impact of Deborah number on the temperature profiles under low and high Reynolds number conditions in converging and diverging geometries.

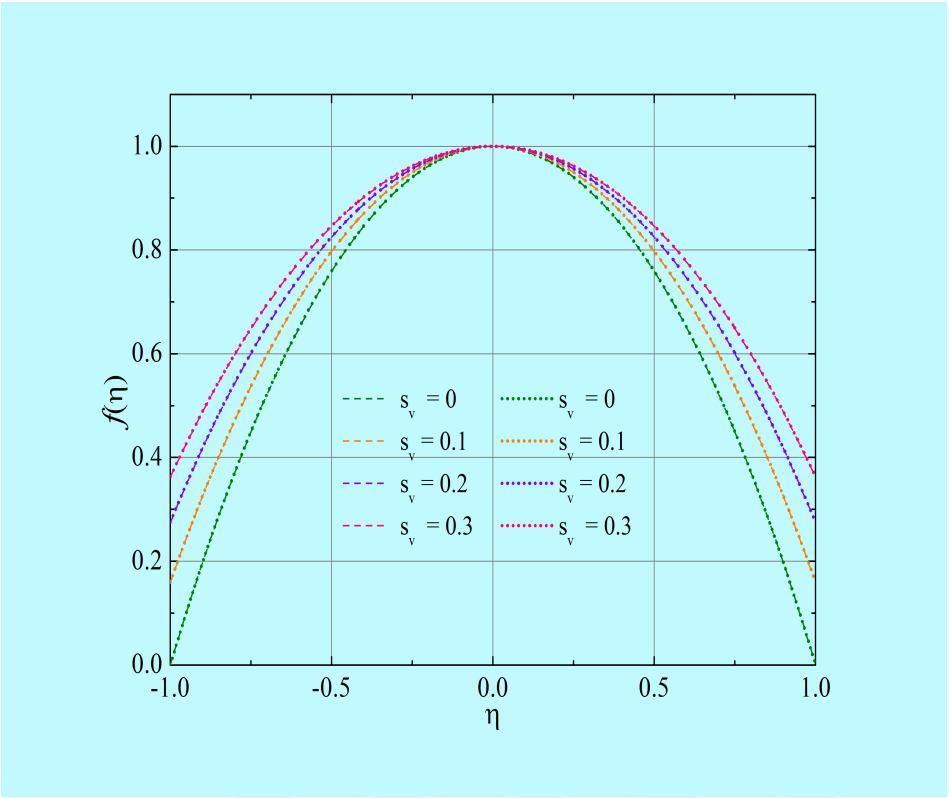


Figure 5.9a : Effect on velocity profile at low Reynolds number.

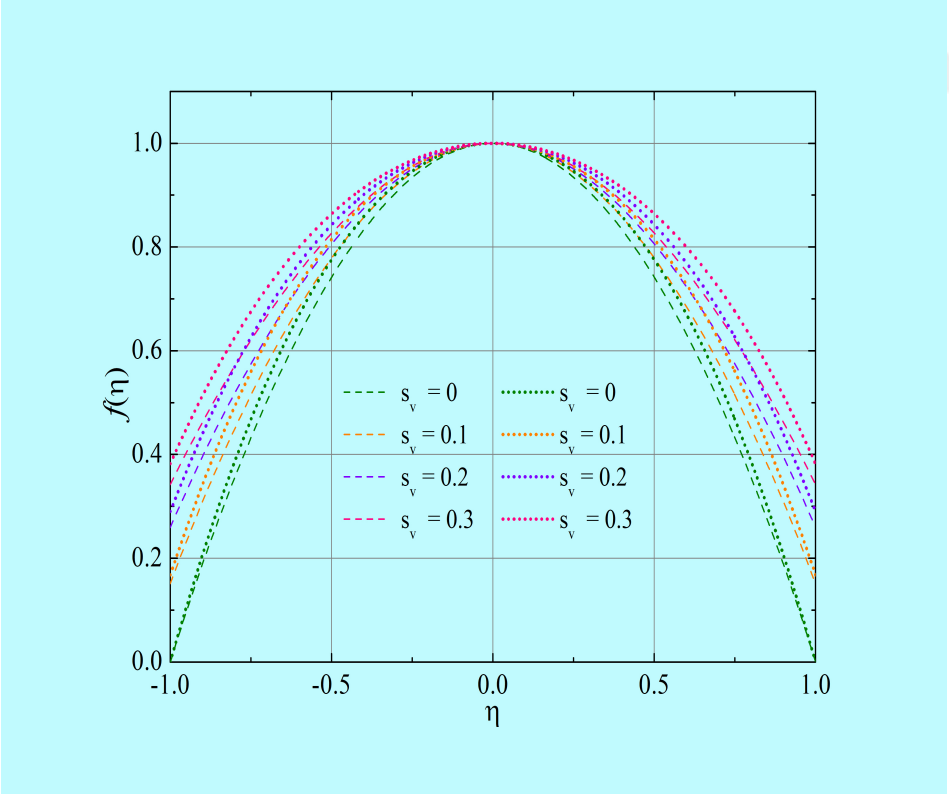


Figure 5.9b : Effect on velocity profile at high Reynolds number.

Figure 5.9 : Impact of s_v coefficient on the velocity distributions under low and high Reynolds number conditions in converging and diverging geometries.

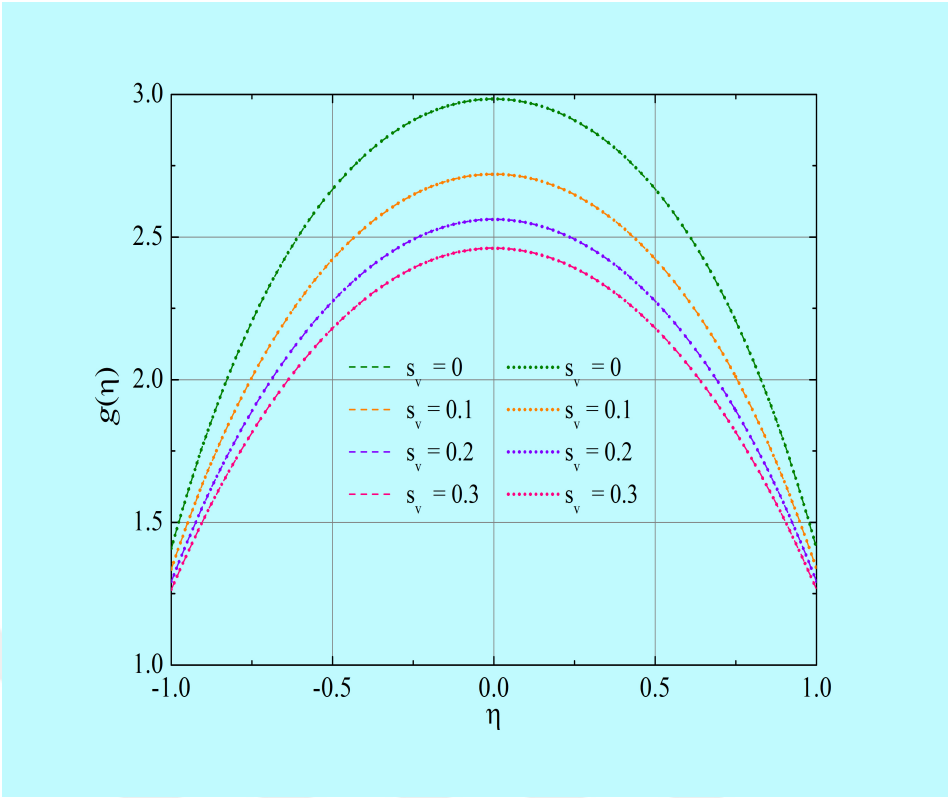


Figure 5.10a : Effect on temperature profile at low Reynolds number.

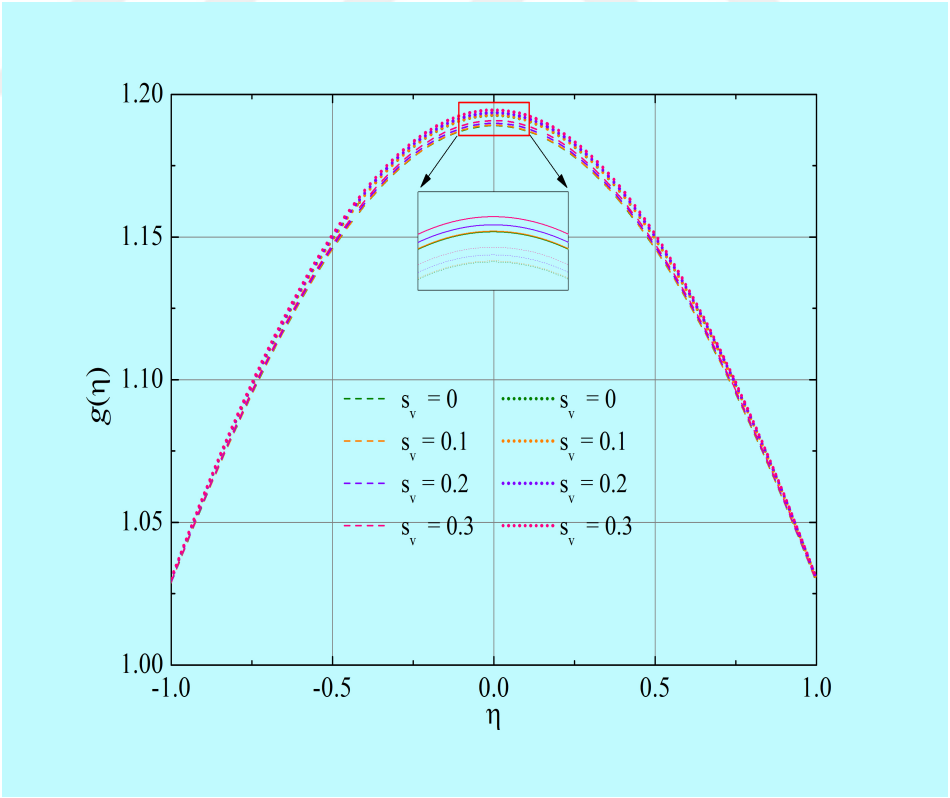


Figure 5.10b : Effect on temperature profile at high Reynolds number.

Figure 5.10 : Impact of s_v coefficient on the temperature profiles under low and high Reynolds number conditions in converging and diverging geometries.

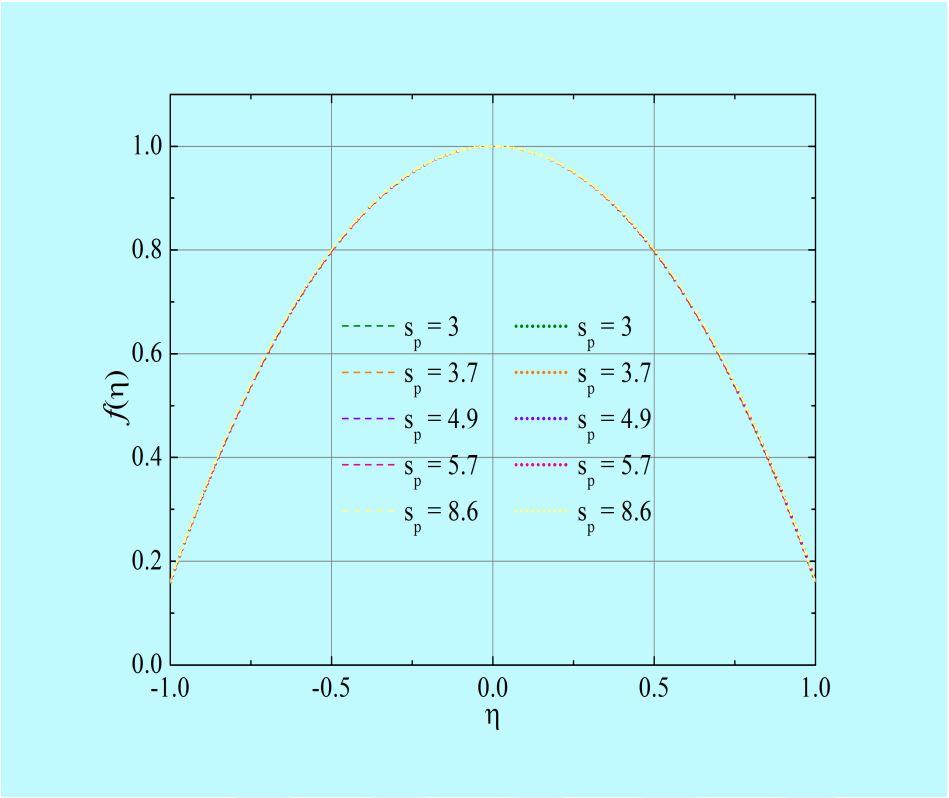


Figure 5.11a : Effect on velocity profile at low Reynolds number.

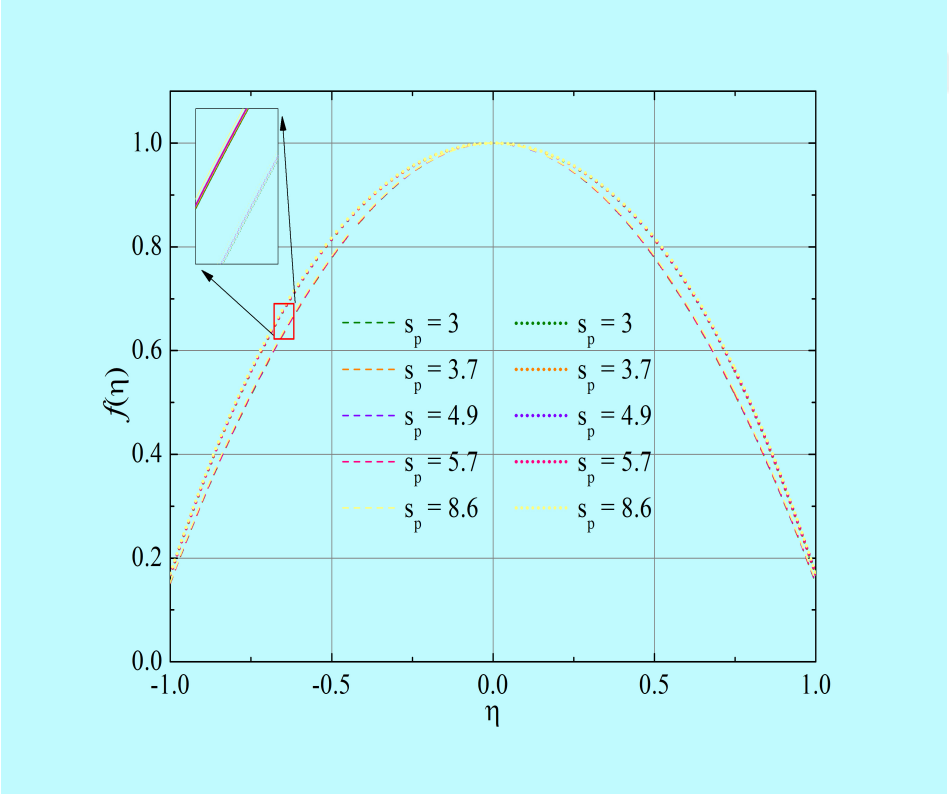


Figure 5.11b : Effect on velocity profile at high Reynolds number.

Figure 5.11 : Impact of s_p on the velocity distributions under low and high Reynolds number conditions in converging and diverging geometries.

remain almost unchanged across all shape parameter values. In the high Reynolds number case, there is a slight difference in velocity profiles between the two channel types. However, in both flow types, the shape parameter does not have a significant impact on the velocity distributions. Figures 5.12a and 5.12b show the effect of the shape parameter on temperature values at low and high Reynolds numbers. In the low Reynolds case, increasing the shape parameter leads to a decrease in temperature values near the centerline region. Nearly identical temperature profiles are obtained for both converging and diverging channels. As the nanoparticle surface area increases, heat transfer improves, resulting in a reduction in temperature values.

Figures 5.13a and 5.13b show the effect of the radiation parameter on temperature values within the channel at low and high Reynolds numbers, respectively. Four different values of the radiation coefficient are examined. As the radiation coefficient increases, the temperature values near the center region decrease. A decrease in the radiation parameter corresponds to an increase in the mean absorption coefficient. An increase in the absorption coefficient leads to a greater amount of absorbed radiation, which in turn results in higher temperature values. In the low Reynolds number case, the temperature profiles do not vary with the type of channel flow. However, in the high Reynolds number case, the temperature values in the converging channel are slightly higher compared to those in the diverging channel.

Figures 5.14a and 5.14b show the effect of the Brinkman number on the temperature values for low and high Reynolds numbers. For the low Reynolds number, the Brinkman number significantly affects the temperature distribution in the channel for both converging and diverging channels. For the same Brinkman number, however, the identical temperature profiles are observed in converging and diverging channels. Similarly, for the high Reynolds number case, the temperature profile is greatly influenced by the Brinkman number. Unlike the low Reynolds number case, for the same Brinkman number, there is a difference in temperature distributions for the converging and diverging channels. The temperature values of the converging channel are higher than those of the diverging channel.

Figures 5.15a and 5.15b illustrate the effect of the jump-temperature parameter on temperature values for low and high Reynolds numbers, respectively. For low Reynolds numbers, the jump-temperature parameter has a strong influence on the

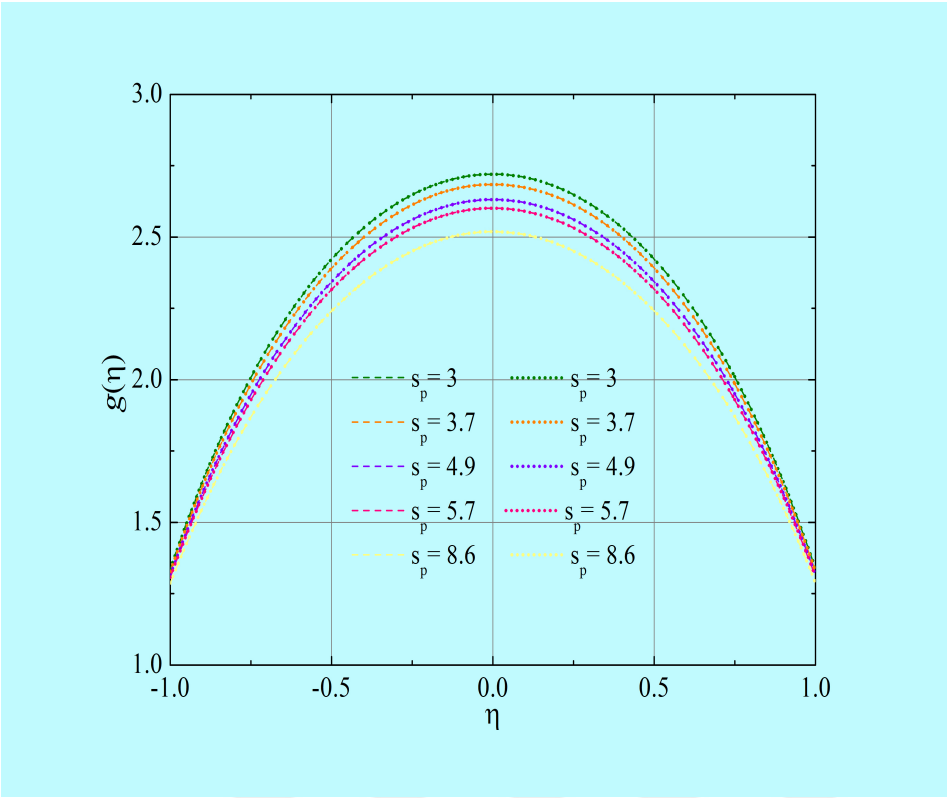


Figure 5.12a : Effect on temperature profile at low Reynolds number.

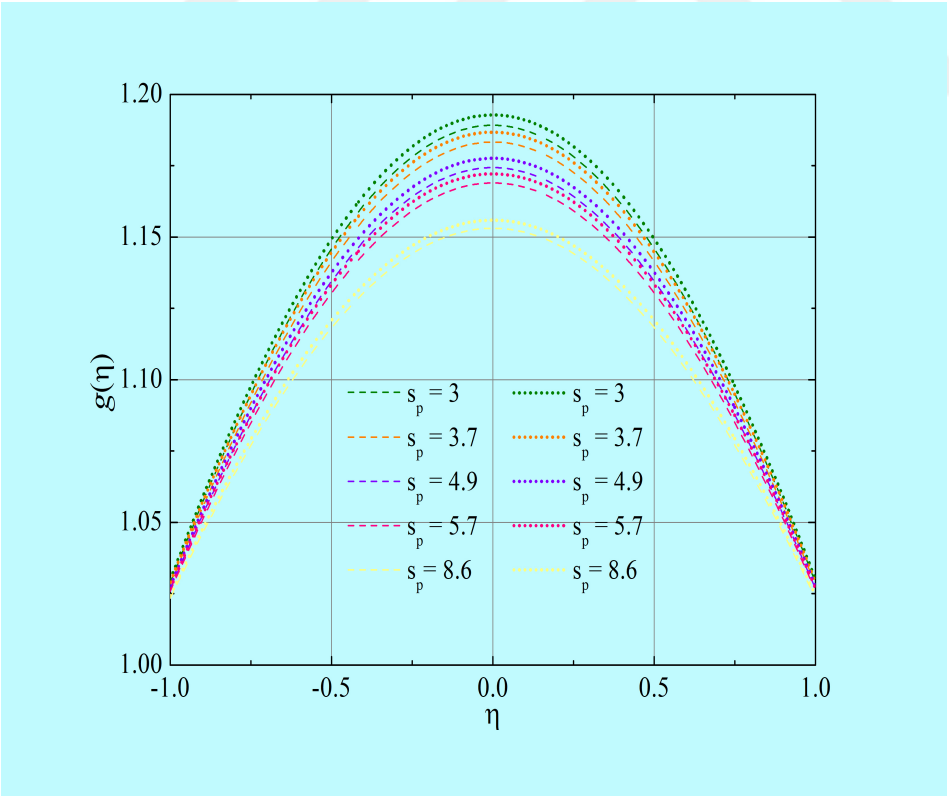


Figure 5.12b : Effect on temperature profile at high Reynolds number.

Figure 5.12 : Impact of s_p on the temperature profiles under low and high Reynolds number conditions in converging and diverging geometries.

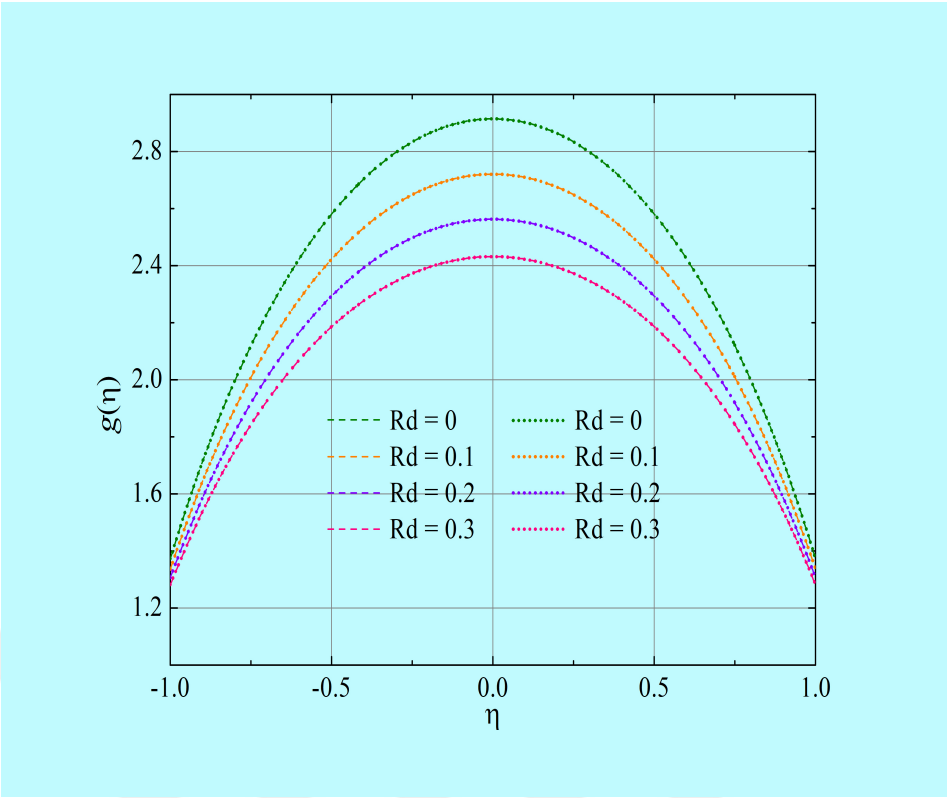


Figure 5.13a : Effect on temperature profile at low Reynolds number.

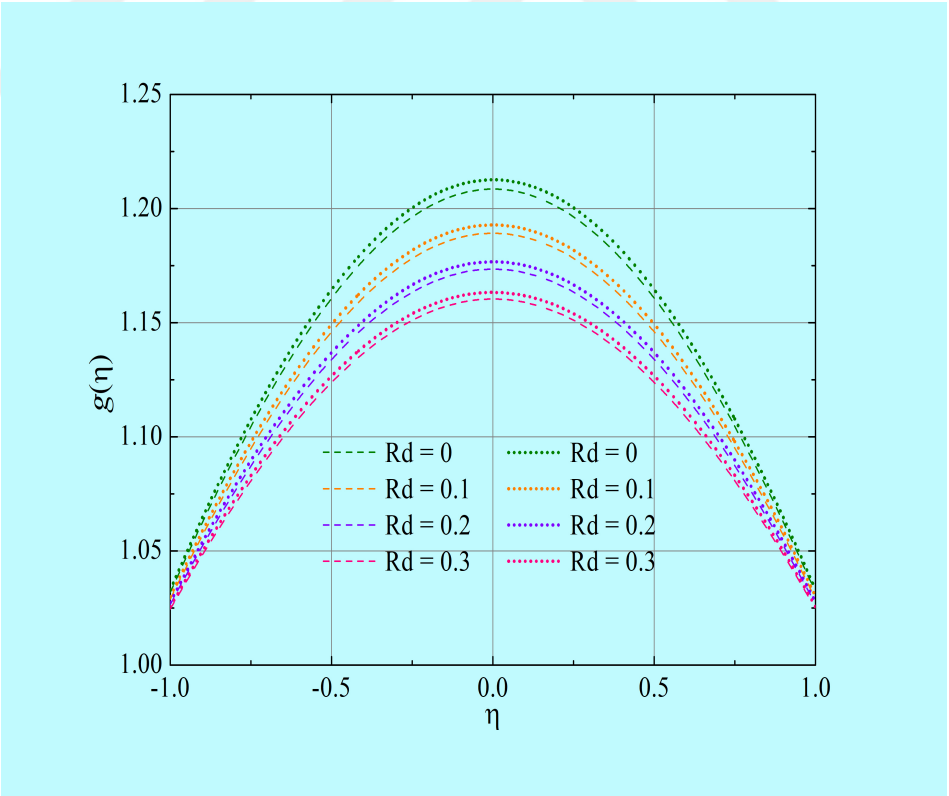


Figure 5.13b : Effect on temperature profile at high Reynolds number.

Figure 5.13 : Impact of Rd parameter on the temperature profiles under low and high Reynolds number conditions in converging and diverging geometries.

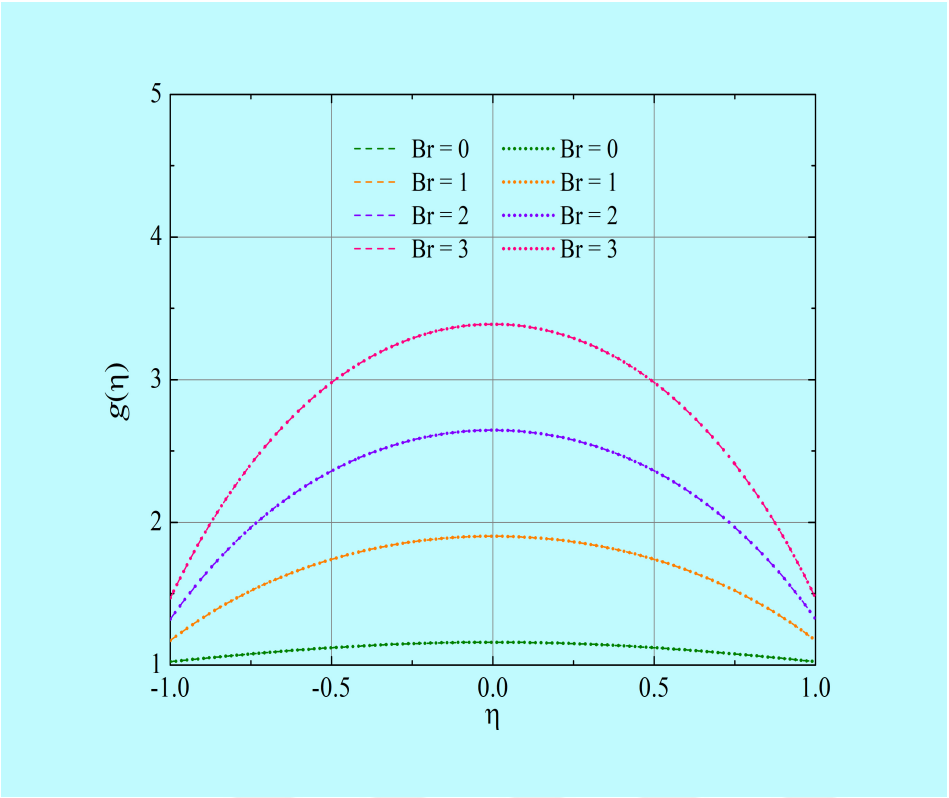


Figure 5.14a : Effect on temperature profile at low Reynolds number.

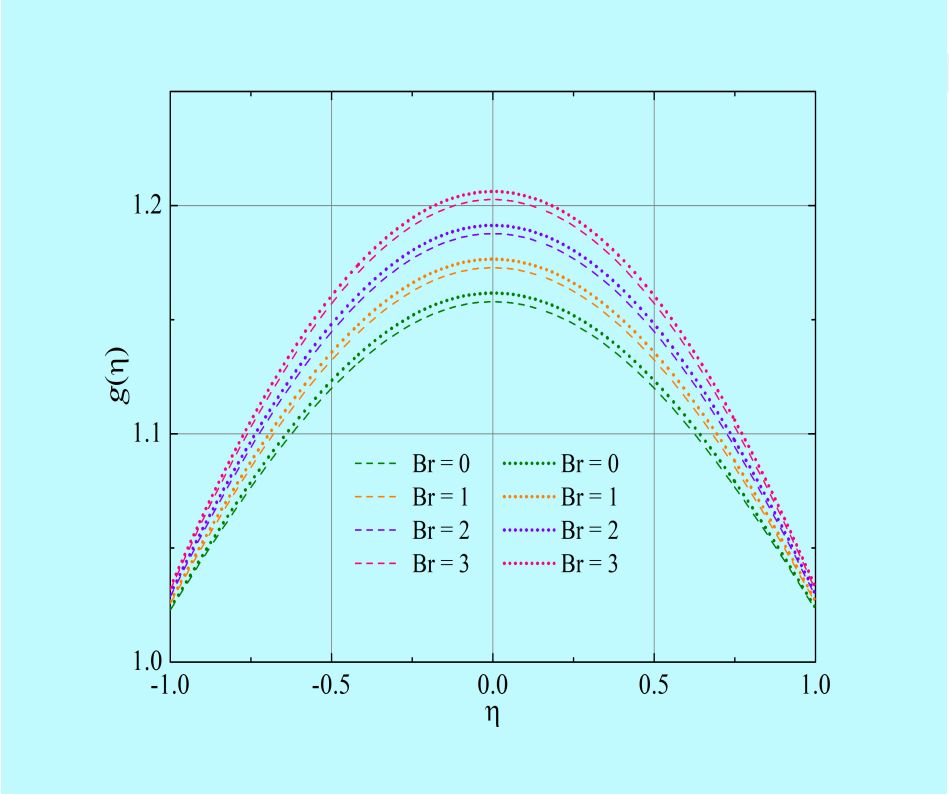


Figure 5.14b : Effect on temperature profile at high Reynolds number.

Figure 5.14 : Impact of Br number on the temperature profiles under low and high Reynolds number conditions in converging and diverging geometries.

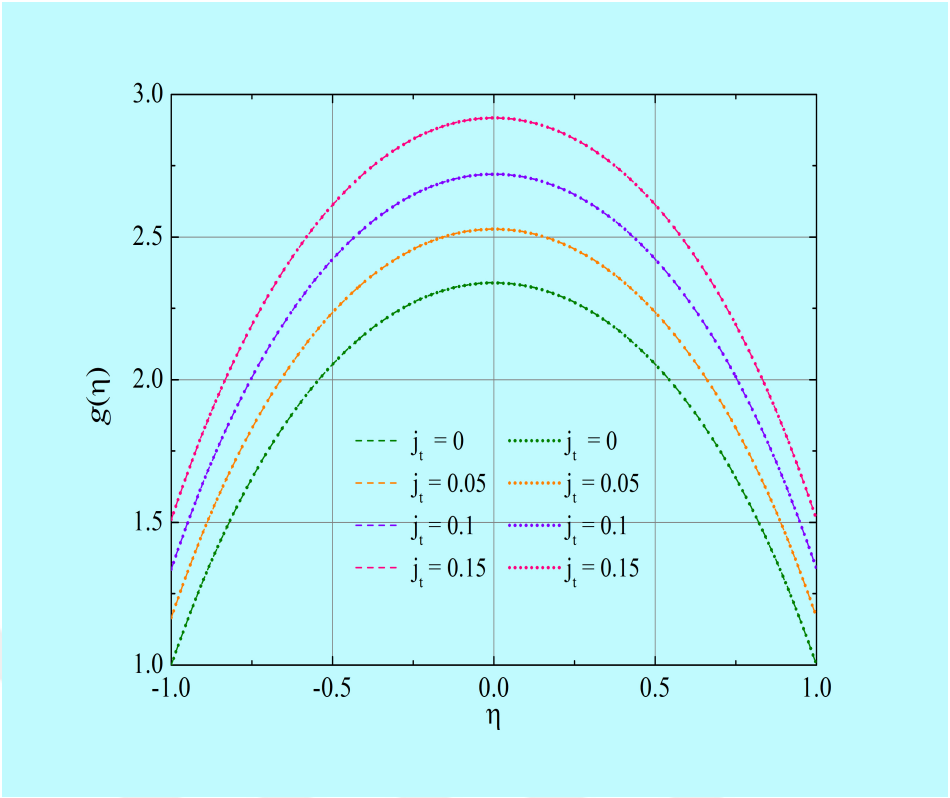


Figure 5.15a : Effect on temperature profile at low Reynolds number.

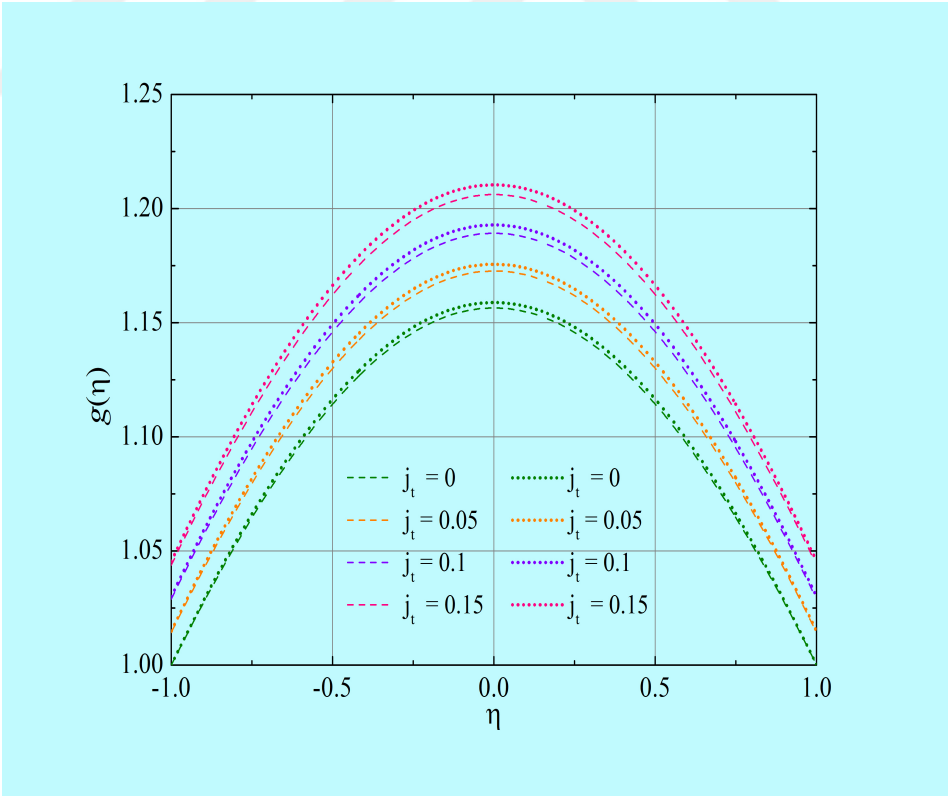


Figure 5.15b : Effect on temperature profile at high Reynolds number.

Figure 5.15 : Impact of j_t coefficient on the temperature profiles under low and high Reynolds number conditions in converging and diverging geometries.

temperature distribution. The profiles are identical for both diverging and converging channels. The same effects as those created by the Brinkman number are observed. In the situation of high Reynolds numbers, temperature values are also influenced significantly by the jump-temperature parameter. Temperature values within the converging channel are nevertheless greater than the temperature values in the diverging channel. In all cases, as the jump-temperature parameter increases, the temperature values also increase.

5.2 Investigation of Skin Friction Coefficient and Nusselt Number

In this section, the effect of Reynolds number, Hartmann number, Darcy parameter, Forchheimer parameter, slip-velocity coefficient, jump-temperature parameter, shape parameter, and nanoparticle volume concentration on the engineering parameters, including skin friction coefficient and Nusselt number, was investigated. Different intervals were considered for each parameter. Due to the importance of high heat transfer for tumor treatment, a broader interval of analyses was performed. Since an excessive increase in skin friction can create undesired phenomena, it is essential to control this parameter, and its trend was also investigated accordingly. During these investigations, which are carried out based on the figures, the parameters studied varied while the other dimensionless numbers and parameters were kept constant. The constant values used are: Re = 50, $\alpha = \pm 5°$, De = 0.1, $\mathrm{Dr}_1 = 0.5$, $\mathrm{Dr}_2 = 0.5$, Ec = 0.1, Ha = 10, Pr = 21, Rd = 0.1, $s_p = 3$, $s_v = 0.1$, $j_t = 0.1$, $\Phi_1 = \Phi_2 = \Phi_3 = 0.02$. In the figures, the converging channel is represented by a dotted line ($\cdots$), and the diverging channel by a dashed line ($---$).

Figure 5.16 illustrates the effect of the Reynolds number on the engineering parameters. The Reynolds number is varied between 0 and 100. Throughout this range, both the Nu and the C_f exhibit analogous trends. For Reynolds numbers between 0 and approximately 10, both parameters decline sharply. For Reynolds numbers from 10 to 50, the decline continues but at a slowing rate. After a Reynolds number of 50, the values are almost constant till 100. The curves thus obtained for both converging and diverging channels are almost identical. The "low Reynolds number case" mentioned symbolizes the region where the engineering parameters decrease sharply, while the "high Reynolds number case" symbolizes the region where they decrease slowly. The following parameter analysis is conducted using a Reynolds number of 50.

Figure 5.17 shows the effect of the Hartmann number on engineering parameters in diverging and converging channels. As can be seen from the figures, with an increase in the Hartmann number, the C_f and the Nu for both channels also increase. The study covers a Hartmann number from 0 to 30. For all, the engineering parameters in the converging channel are higher than those in the diverging channel. In the interval 0–5, C_f and Nu increase steeply, but beyond this interval, the rate of increase is slow.

Figures 5.18 and 5.19 present the influence of the Darcy and Forchheimer parameters on engineering parameters in diverging and converging channels. The Darcy parameter is changed within the range from 0.2 to 2. In the diverging channel, an increase in the Darcy parameter reduces both the Nu and the C_f. Unlike this, in the diverging channel, C_f and Nu increase with an increasing Darcy parameter. The Forchheimer parameter is also increased between 0 and 2. Similar to the Darcy parameter, the increase in the Forchheimer parameter leads to a decrease in engineering parameters in the converging channel, while in the diverging channel, C_f and Nu increase.

Figures 5.20 and 5.21 show the effect of the velocity-slip parameter and jump-temperature parameter on the engineering parameters for the two-channel flows. The velocity-slip parameter is varied between 0 and 0.2. As the slip-velocity parameter increases, the C_f decreases in both the diverging/converging channels. As can be seen from the graphs, the slip-velocity parameter has no significant effect on the Nu, which remains almost constant in the whole range. However, as the slip-velocity increases, a very minor rise in Nu is observed. The jump-temperature parameter has an effect on the Nu only. As the jump-temperature parameter increases, the Nu increases.

Figure 5.22 illustrates the effect of particle geometry on engineering parameters for both converging and diverging channels. Five different shape factors are considered: 3, 3.7, 4.9, 5.7, and 8.6, which correspond to sphere, brick, cylinder, platelet, and blade geometries, respectively. As observed from the figures, an increase in the shape factor slightly increases the C_f. However, the Nu also increases with the shape factor, and this increase is much more significant compared to that of C_f.

Figure 5.23 shows the effect of total volume concentration on the engineering parameters. The range of total volume fraction is 0–0.1. For both channel flow types, as the total volume fraction increases, the C_f and the Nu also increase. The effect of total volume fraction on C_f is more significant than its effect on Nu.

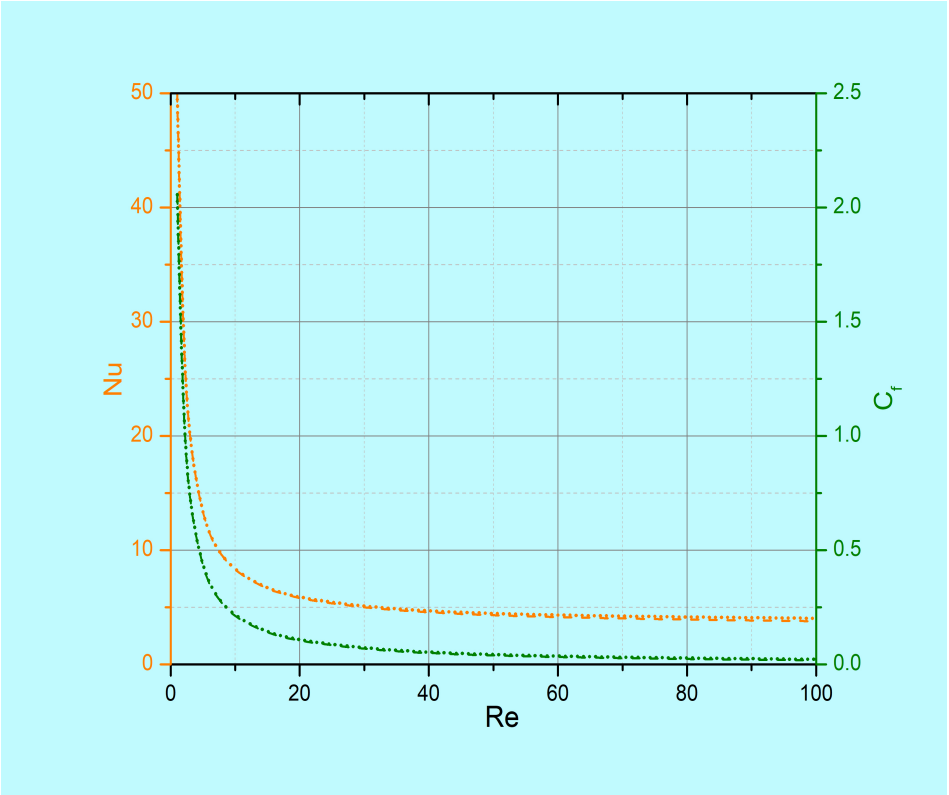


Figure 5.16 : Variation in C_f and Nu as functions of Reynolds number with constant parameter settings.

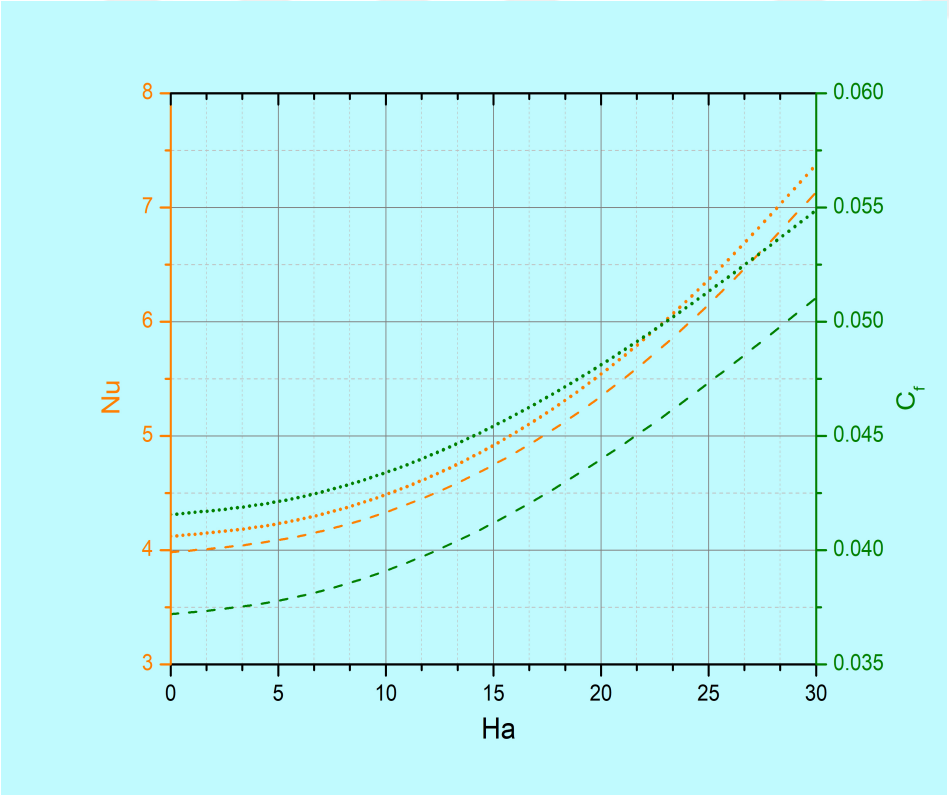


Figure 5.17 : Variation in C_f and Nu as functions of Hartmann number with constant parameter settings.

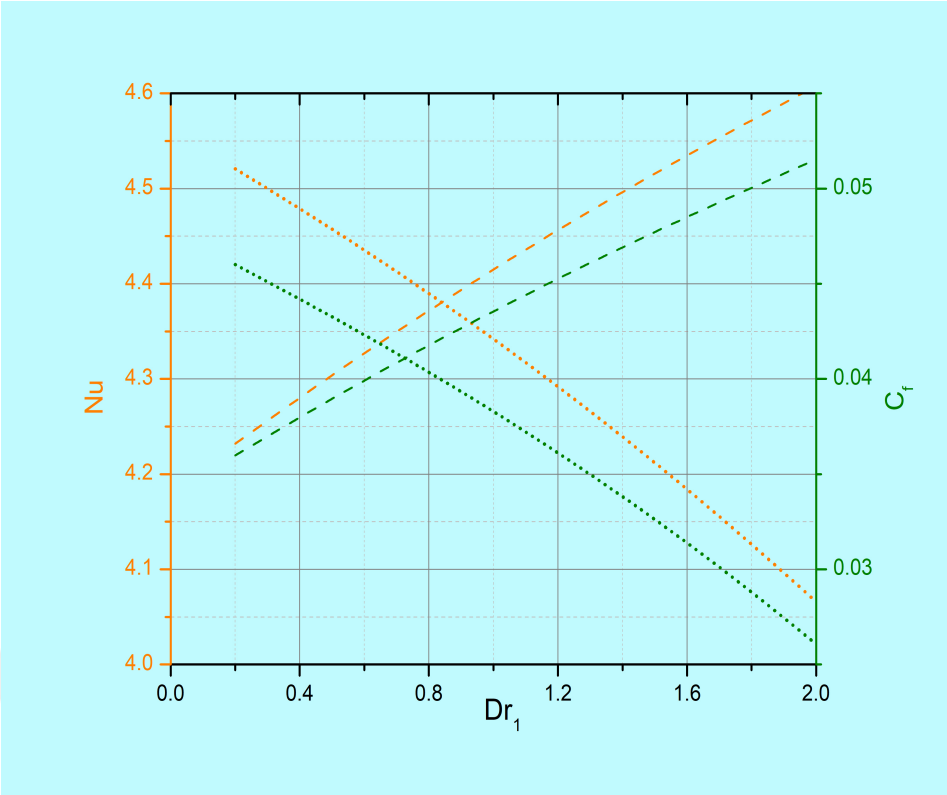


Figure 5.18 : Variation in C_f and Nu as functions of Dr_1 parameter with constant parameter settings.

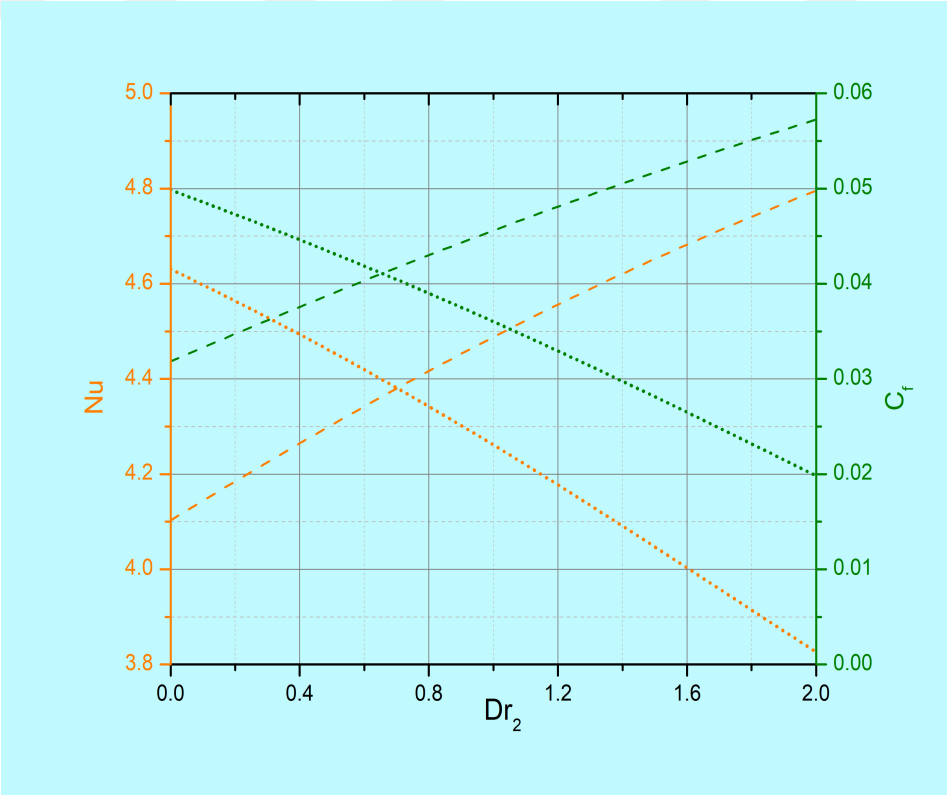


Figure 5.19 : Variation in C_f and Nu as functions of Dr_2 parameter with constant parameter settings.

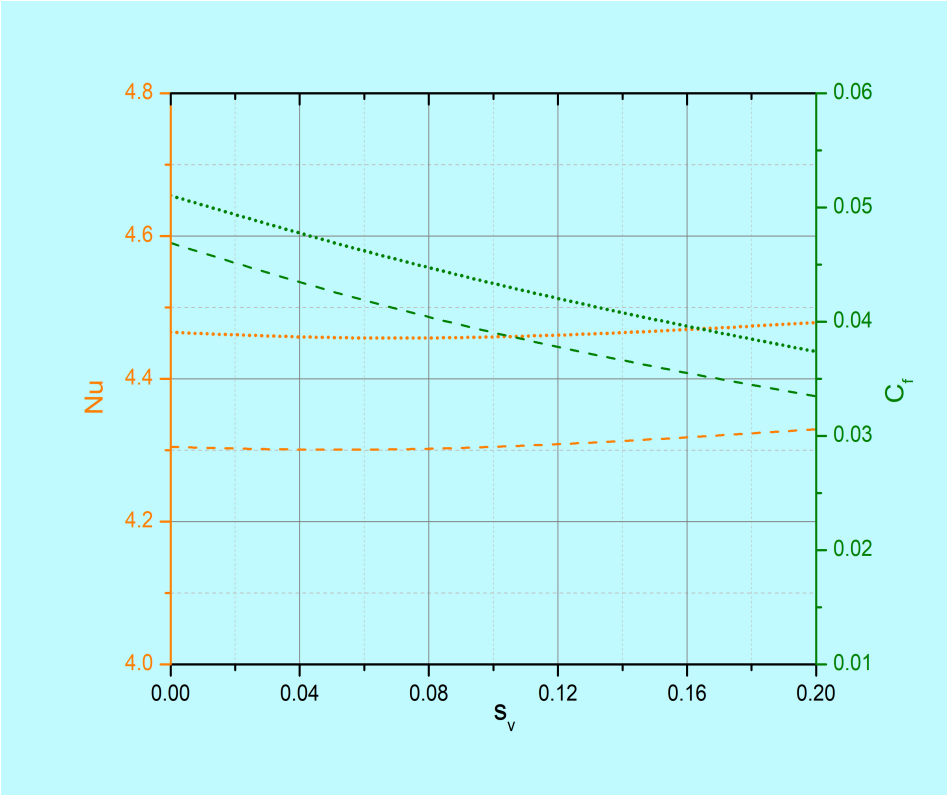


Figure 5.20 : Variation in C_f and Nu as functions of s_v parameter with constant parameter settings.

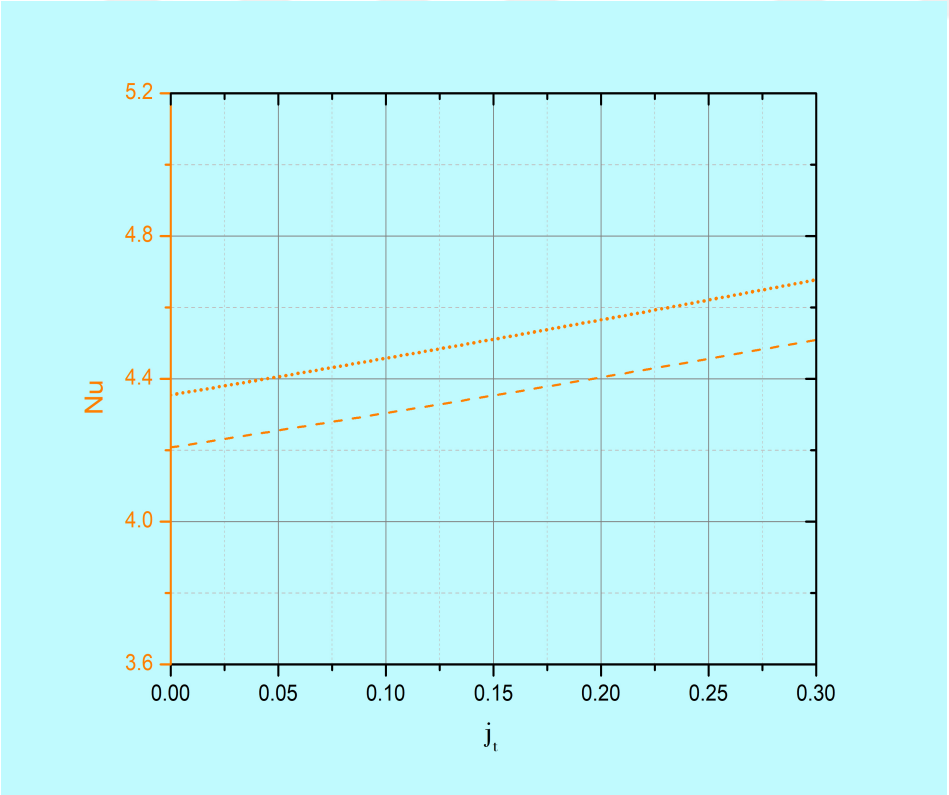


Figure 5.21 : Variation in C_f and Nu as functions of j_t parameter with constant parameter settings.

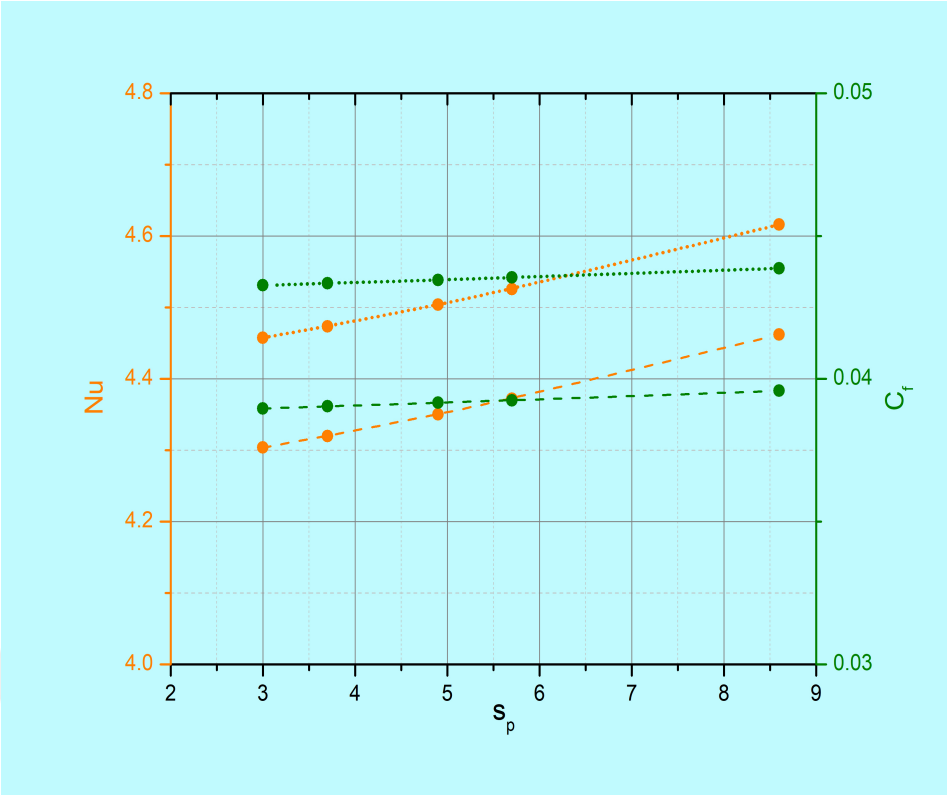


Figure 5.22 : Variation in C_f and Nu as functions of s_p with constant parameter settings.

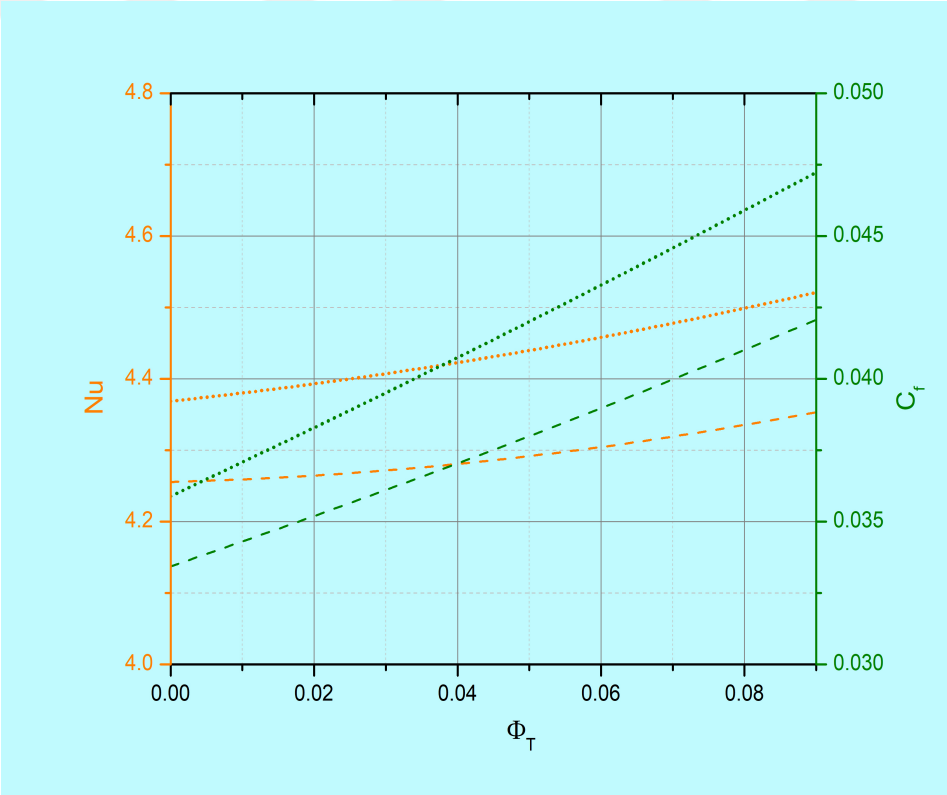


Figure 5.23 : Variation in C_f and Nu as functions of Φ_T with constant parameter settings.

6. CONCLUSIONS AND RECOMMENDATIONS

In this present work, second-grade non-Newtonian fluid flow through converging and diverging channels in a non-Darcy porous medium under the influence of a magnetic medium is investigated. Blood has been selected as the base fluid, and its behavior is modeled by using the second-grade non-Newtonian fluid model. The impact of thermal radiation is taken into account by adopting the Rosseland approximation. The boundary conditions are chosen in accordance with the Jeffrey-Hamel flow configuration. Furthermore, due to their relevance in tumor treatment and drug delivery devices, wall slip conditions are also considered. Besides that, the influence of the nanoparticle shape is examined using five different parameters corresponding to various nanoparticle geometries. Navier-Stokes and energy equations are simplified into PDEs representing the physical configuration. Similarity variables are used to convert such nonlinear PDEs into a system of ODEs. Similarity variables, along with corresponding boundary conditions, are then solved with the function bvp4c, an implementation of the finite difference collocation method. The impact of different physical variables, including the Deborah number, Hartmann number, Darcy parameter, Forchheimer parameter, slip velocity coefficient, jump-temperature parameter, Brinkman number, shape parameter, angle of inclination, and volume concentration, on the velocity and temperature distributions is analyzed. Finally, the effect of these physical parameters on engineering parameters such as the skin friction coefficient (C_f) and the Nusselt number (Nu) is analyzed.

To investigate the effect of the Reynolds number, two different Reynolds numbers are considered. The influence of each physical parameter is examined in both cases. For low Reynolds numbers, the results are found to be very similar for both types of channel flows (converging and diverging). In contrast, for high Reynolds numbers, noticeable differences are observed between the two channel flow types.

The effect of inclination angle on velocity values is very small in the case of low and high Reynolds number cases for both types of channel flow. The velocity rises gradually as the inclination angle rises. The effect of inclination angle on temperature

profiles is more pronounced, particularly under the low Reynolds number condition. As the inclination angle rises, the temperature closer to the center of the channel increases considerably.

The effect of the Deborah number, which characterizes the second-grade non-Newtonian fluid model, is also considered. Different Deborah numbers are linked with different rheological behaviors of blood. While analyzing with a Deborah number of 0.3, it was found that using a second-grade fluid model yields approximately a 3% variation in velocity magnitudes. For both channel flows, a higher Deborah number provides larger temperature values near the middle of the channel and a rise in the mean temperature. The influence of the Deborah number on temperature distributions becomes stronger in the low Reynolds number case than in the high Reynolds number case. Even though the difference is approximately 0.5% in the high Reynolds number case, a 9% difference is reported for the low Reynolds number case. Therefore, under high Reynolds number conditions, it can be concluded that the Newtonian fluid assumption can be adopted while solving the energy equation. However, under low Reynolds numbers, the Newtonian assumption can lead to critical errors.

The effect of the slip-velocity parameter, which impacts the boundary condition at the wall, has been investigated in both channel flow types. In considering the effect of slip-velocity on velocity values, the outcome is a rise in the slip-velocity parameter, lowering the degree of deformation. This then lowers wall shear stress, and therefore, there is a reduction in C_f. Increasing the slip-velocity parameter in the low Reynolds case results in a decrease in temperature values in regions close to the centerline. In the high Reynolds case, increasing the slip-velocity parameter results in an increase in temperature values.

The increase in the surface area of the particles results in an increase in the Nu number, which represents the rate of heat transfer at the wall. The temperature at the wall in the Jeffrey-Hamel flow is less than at the center. The increase in the heat transfer results in a decrease in the average and maximum temperature.

The increase in the radiation coefficient leads to a decrease in the mean absorption coefficient, which results in a reduction in the temperature values.

The increase in the Darcy parameter, Forchheimer parameter, and Hartmann number leads to an increase in the amount of transferred momentum in the diverging channel.

As a result, the skin friction values also increase. This increase is a desired condition for drug delivery. Parameters with a significant effect on temperature values, such as the inclination angle, are important for cancer therapy because heat transfer in a region should be enhanced to combat cancer cells. The increase in the strength of the magnetic medium also causes an increase in temperature values near the center of the channel.

Different non-Newtonian models can be integrated into the study. Apart from Al_2O_3, TiO_2, and Ag, various nanoparticles used in drug delivery and tumor treatment can also be examined in a separate study. In addition to thermal radiation and magnetic fields, various effects can be investigated.

REFERENCES

[1] **Choi, S.U.S. and Eastman, J.A.** (1995). Enhancing thermal conductivity of fluids with nanoparticles, *In ANL/MSD/CP-84938; CONF-951135-29*, Vol. 66.

[2] **Bacha, H.B.**, **Ullah, N.**, **Hamid, A.**, **and Shah, N.A.** (2024). A comprehensive review on nanofluids: Synthesis, cutting-edge applications, and future prospects, *International Journal of Thermofluids*, *22*, 100595, doi : 10.1016/j.ijft.2024.100595.

[3] **Xuan, Y. and Roetzel, W.** (2000). Conceptions for heat transfer correlation of nanofluids, *International Journal of Heat and Mass Transfer*, *43*(19), 3701–3707, doi : 10.1016/s0017-9310(99)00369-5.

[4] **Bilal, S.**, **Shah, I.A.**, **Marzougui, S.**, **and Ali, F.** (2023). Entropy analysis in single phase nanofluid in square enclosure under effectiveness of inclined magnetic field by executing finite element simulations, *Geoenergy Science and Engineering*, *225*, 211483, doi : 10.1016/j.geoen.2023.211483.

[5] **Adnan and Ashraf, W.** (2023). Study of heat transfer in ternary nanofluid between parallel plates influenced by different physical parameters, *Journal of Thermal Analysis and Calorimetry*, *148*(20), 10645–10661, doi : 10.1007/s10973-023-12418-4.

[6] **Buongiorno, J.** (2005). Convective transport in nanofluids, *Journal of Heat Transfer*, *128*(3), 240–250, doi : 10.1115/1.2150834.

[7] **Valinataj-Bahnemiri, P.**, **Ramiar, A.**, **Manavi, S.**, **and Mozaffari, A.** (2015). Heat transfer optimization of two phase modeling of nanofluid in a sinusoidal wavy channel using Artificial Bee Colony technique, *Engineering Science and Technology, an International Journal*, *18*(4), 727–737, doi : 10.1016/j.jestch.2015.05.005.

[8] **Khoshtarash, H.**, **Siavashi, M.**, **Ramezanpour, M.**, **and Blunt, M.J.** (2023). Pore-scale analysis of two-phase nanofluid flow and heat transfer in open-cell metal foams considering Brownian motion, *Applied Thermal Engineering*, *221*, 119847, doi : 10.1016/j.applthermaleng.2022.119847.

[9] **Bianco, V.**, **Chiacchio, F.**, **Manca, O.**, **and Nardini, S.** (2009). Numerical investigation of nanofluids forced convection in circular tubes, *Applied Thermal Engineering*, *29*(17–18), 3632–3642, doi : 10.1016/j.applthermaleng.2009.06.019.

[10] **Göktepe, S.**, **Atalık, K.**, **and Ertürk, H.** (2014). Comparison of single and two-phase models for nanofluid convection at the entrance of a uniformly heated tube, *International Journal of Thermal Sciences*, *80*, 83–92, doi : 10.1016/j.ijthermalsci.2014.01.014.

[11] **Çiçek, O.**, **Baytaş, A.F.**, **and Baytaş, A.C.** (2021). Entropy generation of mixed convection of SWCNT–water nanofluid filled an annulus with a rotating cylinder and porous lining under LTNE, *International Journal of Numerical Methods for Heat & Fluid Flow*, *31*(5), 1588–1617, doi : 10.1108/hff-04-2020-0229.

[12] **Çiçek, O.**, **Baytaş, A.F.**, **and Baytaş, A.C.** (2023). Entropy generation minimization of hybrid nanofluid mixed convection flow in lid-driven square enclosure with heat-generating porous layer on inner walls, *International Journal of Numerical Methods for Heat & Fluid Flow*, doi : 10.1108/hff-05-2023-0281.

[13] **Wang, D.**, **Ali, M.A.**, **Alizadeh, A.**, **Chaturvedi, R.**, **Ali, M.R.**, **and Sohail, M.** (2023). A numerical investigation of a two-phase nanofluid flow with phase change materials in the thermal management of lithium batteries and use of machine learning in the optimization of the horizontal and vertical distances between batteries, *Case Studies in Thermal Engineering*, *41*, 102582, doi : 10.1016/j.csite.2022.102582.

[14] **Liu, M.S.**, **Lin, M.C.C.**, **Tsai, C.**, **and Wang, C.C.** (2006). Enhancement of thermal conductivity with cu for nanofluids using chemical reduction method, *International Journal of Heat and Mass Transfer*, *49*(17–18), 3028–3033, doi : 10.1016/j.ijheatmasstransfer.2006.02.012.

[15] **Syam Sundar, L.**, **Singh, M.K.**, **and Sousa, A.C.** (2013). Investigation of thermal conductivity and viscosity of fe3o4 nanofluid for heat transfer applications, *International Communications in Heat and Mass Transfer*, *44*, 7–14, doi : 10.1016/j.icheatmasstransfer.2013.02.014.

[16] **Kakavandi, A. and Akbari, M.** (2018). Experimental investigation of thermal conductivity of nanofluids containing of hybrid nanoparticles suspended in binary base fluids and propose a new correlation, *International Journal of Heat and Mass Transfer*, *124*, 742–751, doi : 10.1016/j.ijheatmasstransfer.2018.03.103.

[17] **Leong, K.**, **Ku Ahmad, K.**, **Ong, H.C.**, **Ghazali, M.**, **and Baharum, A.** (2017). Synthesis and thermal conductivity characteristic of hybrid nanofluids – a review, *Renewable and Sustainable Energy Reviews*, *75*, 868–878, doi : 10.1016/j.rser.2016.11.068.

[18] **Nazir, A.**, **Qamar, A.**, **Rafique, M.S.**, **Murtaza, G.**, **Arshad, T.**, **Muneeb, A.**, **Jabeen, K.**, **Mujtaba, M.**, **Fayaz, H.**, **and Saleel, C.A.** (2024). Enhanced thermal conductivity of plasma generated zno–mgo based hybrid nanofluids: An experimental study, *Heliyon*, *10*(4), e26396, doi : 10.1016/j.heliyon.2024.e26396.

[19] **Boroomandpour, A.**, **Toghraie, D.**, **and Hashemian, M.** (2020). A comprehensive experimental investigation of thermal conductivity of a ternary hybrid nanofluid containing mwcnts- titania-zinc oxide/water-ethylene glycol (80:20) as well as binary and mono nanofluids, *Synthetic Metals*, *268*, 116501, doi : 10.1016/j.synthmet.2020.116501.

[20] **Adun, H.**, **Kavaz, D.**, **Dagbasi, M.**, **Umar, H.**, **and Wole-Osho, I.** (2021). An experimental investigation of thermal conductivity and dynamic viscosity of al2o3-zno-fe3o4 ternary hybrid nanofluid and development of machine learning model, *Powder Technology*, *394*, 1121–1140, doi : 10.1016/j.powtec.2021.09.039.

[21] **Mousavi, M.**, **Pouranfard, A.**, **and Darvishi, P.** (2024). Experimental study and modeling of thermal and rheological characteristics of water-based cuo/caco3/sio2 ternary hybrid nanofluid, *Colloids and Surfaces A: Physicochemical and Engineering Aspects*, *686*, 133367, doi : 10.1016/j.colsurfa.2024.133367.

[22] **Sheikhpour, M.**, **Arabi, M.**, **Kasaeian, A.**, **Rokn Rabei, A.**, **and Taherian, Z.** (2020). Role of nanofluids in drug delivery and biomedical technology: Methods and applications, *Nanotechnology, Science and Applications*, pp. 47–59.

[23] **Hamad, E.M.**, **Khaffaf, A.**, **Yasin, O.**, **Abu El-Rub, Z.**, **Al-Gharabli, S.**, **Al-Kouz, W.**, **and Chamkha, A.J.** (2021). Review of nanofluids and their biomedical applications, *Journal of Nanofluids*, *10*(4), 463–477, doi : 10.1166/jon.2021.1806.

[24] **Thakare, Y.**, **Dharaskar, S.**, **Unnarkat, A.**, **and S. Sonawane, S.** (2022). *Nanofluid-based drug delivery systems*, p. 303–334. Elsevier, p. 303–334, doi : 10.1016/b978-0-323-90564-0.00005-2.

[25] **Meher, A.**, **Tandi, A.**, **Moharana, S.**, **Chakroborty, S.**, **Mohapatra, S.S.**, **Mondal, A.**, **Dey, S.**, **and Chandra, P.** (2024). Silver nanoparticle for biomedical applications: A review, *Hybrid Advances*, *6*, 100184, doi : 10.1016/j.hybadv.2024.100184.

[26] **Jangid, H.**, **Singh, S.**, **Kashyap, P.**, **Singh, A.**, **and Kumar, G.** (2024). Advancing biomedical applications: an in-depth analysis of silver nanoparticles in antimicrobial, anticancer, and wound healing roles, *Frontiers in Pharmacology*, *15*, doi : 10.3389/fphar.2024.1438227.

[27] **Sriram, M.I.**, **Kanth, S.B.M.**, **Kalishwaralal, K.**, **and Gurunathan, S.** (2010). Antitumor activity of silver nanoparticles in dalton's lymphoma ascites tumor model, *International journal of nanomedicine*, pp. 753–762.

[28] **Tran, G.T.**, **Nguyen, N.T.H.**, **Nguyen, N.T.T.**, **Nguyen, T.T.T.**, **Nguyen, D.T.C.**, **and Tran, T.V.** (2023). Plant extract-mediated synthesis of aluminum oxide nanoparticles for water treatment and biomedical applications: a review, *Environmental Chemistry Letters*, *21*(4), 2417–2439, doi : 10.1007/s10311-023-01607-0.

[29] **Islam, S.**, **Rana, B.**, **Parvez, M.**, **Hossain, M.**, **and Rahman, M.** (2023). Electroosmotic flow in ternary (TiO_2-SiO_2-Al_2O_3) blood-based sutterby nanomaterials with bio-active mixers, *Int. J. Thermofluids*, *18*, 100363, doi : 10.1016/j.ijft.2023.100363.

[30] **Jeffery, G.B.** (1915). L. The two-dimensional steady motion of a viscous fluid, *The London, Edinburgh, and Dublin Philosophical Magazine and Journal of Science*, *29*(172), 455–465, doi : 10.1080/14786440408635327.

[31] **Hamel, G.** (1917). Spiralförmige bewegungen zäher flüssigkeiten., *Jahresbericht der Deutschen Mathematiker-Vereinigung*, *25*, 34–60.

[32] **Noureen and Marwat, D.N.K.** (2022). Double-diffusive convection in jeffery–hamel flow, *Scientific Reports*, *12*(1), doi : 10.1038/s41598-022-12908-9.

[33] **Ahmad, S. and Farooq, M.** (2023). Double-diffusive hamel–jeffrey flow of nanofluid in a convergent/divergent permeable medium under zero mass flux, *Scientific Reports*, *13*(1), doi : 10.1038/s41598-023-27938-0.

[34] **Boudjemline, A.**, **Rehman, S.**, **Hashim**, **and Khedher, N.B.** (2023). Analysis of flow and heat transport between converging channel, *The European Physical Journal Special Topics*, *233*(13–14), 2335–2351, doi : 10.1140/epjs/s11734-023-00806-8.

[35] **Rehman, S.**, **Hashim**, **Hassine, S.B.H.**, **Tag Eldin, E.**, **and Shah, S.O.** (2023). Investigation of entropy production with thermal analysis under soret and dufour effects in mhd flow between convergent and divergent channels, *ACS Omega*, *8*(10), 9121–9136, doi : 10.1021/acsomega.2c05937.

[36] **Millsaps, K. and Pohlhausen, K.** (1953). Thermal distributions in Jeffery-Hamel flows between nonparallel plane walls, *Journal of the Aeronautical Sciences*, *20*(3), 187–196, doi : 10.2514/8.2587.

[37] **Eagles, P.M.** (1966). The stability of a family of Jeffery–Hamel solutions for divergent channel flow, *Journal of Fluid Mechanics*, *24*(1), 191–207, doi : 10.1017/s0022112066000582.

[38] **Uribe, F.J.**, **Díaz-Herrera, E.**, **Bravo, A.**, **and Peralta-Fabi, R.** (1997). On the stability of the Jeffery–Hamel flow, *Physics of Fluids*, *9*(9), 2798–2800, doi : 10.1063/1.869390.

[39] **Moghimi, S.M.**, **Ganji, D.D.**, **Bararnia, H.**, **Hosseini, M.**, **and Jalaal, M.** (2011). Homotopy perturbation method for nonlinear MHD Jeffery–Hamel problem, *Computers & Mathematics with Applications*, *61*(8), 2213–2216, doi : 10.1016/j.camwa.2010.09.018.

[40] **Moradi, A.**, **Alsaedi, A.**, **and Hayat, T.** (2013). Investigation of nanoparticles effect on the Jeffery–Hamel flow, *Arabian Journal for Science and Engineering*, *38*(10), 2845–2853, doi : 10.1007/s13369-012-0472-2.

[41] **Turkyilmazoglu, M.** (2014). Extending the traditional Jeffery-Hamel flow to stretchable convergent/divergent channels, *Computers & Fluids*, *100*, 196–203, doi : 10.1016/j.compfluid.2014.05.016.

[42] **Gerdroodbary, M.B.**, **Takami, M.R.**, **and Ganji, D.D.** (2015). Investigation of thermal radiation on traditional Jeffery–Hamel flow to stretchable

convergent/divergent channels, *Case Studies in Thermal Engineering*, *6*, 28–39, doi : 10.1016/j.csite.2015.04.002.

[43] **Dorrepaal, J.M.** (1993). Slip flow in converging and diverging channels, *Journal of Engineering Mathematics*, *27*(4), 343–356, doi : 10.1007/bf00128760.

[44] **Al-Nimr, M.A.**, **Hammoudeh, V.A.**, **and Hamdan, M.A.** (2010). Effect of velocity-slip boundary conditions on jeffery–hamel flow solutions, *Journal of Applied Mechanics*, *77*(4), doi : 10.1115/1.4000918.

[45] **Mohyud-Din, S.T.**, **Khan, U.**, **Ahmed, N.**, **and Sikander, W.** (2015). A study of velocity and temperature slip effects on flow of water based nanofluids in converging and diverging channels, *International Journal of Applied and Computational Mathematics*, *1*(4), 569–587, doi : 10.1007/s40819-015-0032-z.

[46] **Khan, U.**, **Ahmed, N.**, **and Mohyud-Din, S.T.** (2015). Heat transfer effects on carbon nanotubes suspended nanofluid flow in a channel with non-parallel walls under the effect of velocity slip boundary condition: a numerical study, *Neural Computing and Applications*, *28*(1), 37–46, doi : 10.1007/s00521-015-2035-4.

[47] **Shukla, N.**, **Rana, P.**, **and Pop, I.** (2020). Second law thermodynamic analysis of thermo-magnetic jeffery–hamel dissipative radiative hybrid nanofluid slip flow: existence of multiple solutions, *The European Physical Journal Plus*, *135*(10), doi : 10.1140/epjp/s13360-020-00822-w.

[48] **Sheikholeslami, M.**, **Ganji, D.D.**, **Ashorynejad, H.R.**, **and Rokni, H.B.** (2012). Analytical investigation of jeffery-hamel flow with high magnetic field and nanoparticle by adomian decomposition method, *Applied Mathematics and Mechanics*, *33*(1), 25–36, doi : 10.1007/s10483-012-1531-7.

[49] **Hatami, M. and Ganji, D.** (2014). Mhd nanofluid flow analysis in divergent and convergent channels using wrms and numerical method, *International Journal of Numerical Methods for Heat and Fluid Flow*, *24* (5), 1191–1203, doi : 10.1108/hff-01-2013-0010.

[50] **Alnahdi, A.S.**, **Nasir, S.**, **and Gul, T.** (2023). Couple stress ternary hybrid nanofluid flow in a contraction channel by means of drug delivery function, *Mathematics and Computers in Simulation*, *210*, 103–119, doi : 10.1016/j.matcom.2023.02.021.

[51] **Farzin, A.**, **Etesami, S.A.**, **Quint, J.**, **Memic, A.**, **and Tamayol, A.** (2020). Magnetic nanoparticles in cancer therapy and diagnosis, *Advanced healthcare materials*, *9*(9), 1901058.

[52] **Cairncross, D.**, **Collins, G.M.**, **Rostalas, G.**, **and Ludbrook, J.** (1969). Blood viscosity and erythrocyte sedimentation rate in patients with thrombotic arterial disorders, *Medical Journal of Australia*, *1*(26), 1348–1352, doi : https://doi.org/10.5694/j.1326-5377.1969.tb62400.x.

[53] **Ku, D.N.** (1997). Blood flow in arteries, *Annual review of fluid mechanics*, *29* (1), 399–434.

[54] **Berger, S.A. and Jou, L.D.** (2000). Flows in stenotic vessels, *Annual Review of Fluid Mechanics*, *32*(1), 347–382, doi : 10.1146/annurev.fluid.32.1.347.

[55] **Shibeshi, S.S. and Collins, W.E.** (2005). The rheology of blood flow in a branched arterial system, *Applied Rheology*, *15*(6), 398–405, doi : 10.1515/arh-2005-0020.

[56] **Kannojiya, V.**, **Das, A.K.**, **and Das, P.K.** (2021). Simulation of blood as fluid: A review from rheological aspects, *IEEE Reviews in Biomedical Engineering*, *14*, 327–341, doi : 10.1109/rbme.2020.3011182.

[57] **Ngien, S.K.**, **Rahman, N.A.**, **Lewis, R.W.**, **and Ahmad, K.** (2011). Numerical modelling of multiphase immiscible flow in double-porosity featured groundwater systems, *International Journal for Numerical and Analytical Methods in Geomechanics*, *36*(10), 1330–1349, doi : 10.1002/nag.1055.

[58] **Rahman, N.A.**, **Foong, L.K.**, **Lewis, R.W.**, **and Nazir, R.** (2018). Laboratory investigation of lnapl migration in double-porosity soil under fractured condition using digital image analysis, *Transport in Porous Media*, *125* (3), 521–542, doi : 10.1007/s11242-018-1135-x.

[59] **Aly, A.M.**, **Lewis, R.W.**, **and Alsedias, N.** (2023). Effects of magnetic field and thermal radiation on double diffusion of a solid phase in the two connected circular cylinders suspended by nepcm and porous media, *Journal of Porous Media*, *26*(5), 121–138, doi : 10.1615/jpormedia.2022043412.

[60] **Darcy, H.** (1856). *Les fontaines publiques de Dijon*. Victor Dalmont.

[61] **Forchheimer, P.** (1901). Wasserbewegung durch boden., *Zeitschrift des Vereines Deutscher Ingenieure*, *45*(50), 1782–1788.

[62] **Muskat, M.** (1938). The flow of homogeneous fluids through porous media, *Soil Science*, *46*(2), 169.

[63] **Pal, D. and Mondal, H.** (2012). Hydromagnetic convective diffusion of species in darcy–forchheimer porous medium with non-uniform heat source/sink and variable viscosity, *International Communications in Heat and Mass Transfer*, *39*(7), 913–917, doi : 10.1016/j.icheatmasstransfer.2012.05.012.

[64] **Hayat, T.**, **Muhammad, T.**, **Al-Mezal, S.**, **and Liao, S.** (2016). Darcy-forchheimer flow with variable thermal conductivity and cattaneo-christov heat flux, *International Journal of Numerical Methods for Heat & Fluid Flow*, *26*(8), 2355–2369, doi : 10.1108/hff-08-2015-0333.

[65] **Awais, M.**, **Salahuddin, T.**, **and Muhammad, S.** (2024). Effects of viscous dissipation and activation energy for the mhd eyring-powell fluid flow with darcy-forchheimer and variable fluid properties, *Ain Shams Engineering Journal*, *15*(2), 102422, doi : 10.1016/j.asej.2023.102422.

[66] **Azmi, W.F.W.**, **Mohamad, A.Q.**, **Jiann, L.Y.**, **and Shafie, S.** (2023). Unsteady natural convection flow of blood casson nanofluid (au) in a cylinder: nano-cryosurgery applications, *Scientific Reports*, *13*(1), doi : 10.1038/s41598-023-30129-6.

[67] **Suresh Kumar, Y.**, **Hussain, S.**, **Raghunath, K.**, **Ali, F.**, **Guedri, K.**, **Eldin, S.M.**, **and Khan, M.I.** (2023). Numerical analysis of magnetohydrodynamics casson nanofluid flow with activation energy, hall current and thermal radiation, *Scientific Reports*, *13*(1), doi : 10.1038/s41598-023-28379-5.

[68] **Arif, M.**, **Di Persio, L.**, **Kumam, P.**, **Watthayu, W.**, **and Akgül, A.** (2023). Heat transfer analysis of fractional model of couple stress casson tri-hybrid nanofluid using dissimilar shape nanoparticles in blood with biomedical applications, *Scientific Reports*, *13*(1), doi : 10.1038/s41598-022-25127-z.

[69] **Adnan**, **Khan, U.**, **Ahmed, N.**, **and Mohyud-Din, S.T.** (2016). Thermo-diffusion and diffusion-thermo effects on flow of second grade fluid between two inclined plane walls, *Journal of Molecular Liquids*, *224*, 1074–1082, doi : https://doi.org/10.1016/j.molliq.2016.10.068.

[70] **Sakthi, I.**, **Das, R.**, **and Reddy, P.B.A.** (2023). Entropy generation on mhd flow of second-grade hybrid nanofluid flow over a converging/diverging channel: an application in hyperthermia therapeutic aspects, *The European Physical Journal Special Topics*, *233*(6), 1233–1249, doi : 10.1140/epjs/s11734-023-00947-w.

[71] **Gunay, T.**, **Erdem, D.**, **and Sahin, A.Z.** (2025). Investigation of temperature jump, first and second-order velocity slip effects on blood-based ternary nanofluid flow in convergent/divergent channels, *International Journal of Numerical Methods for Heat & Fluid Flow*, *35*(2), 648–682, doi : 10.1108/hff-10-2024-0772.

[72] **Dogonchi, A. and Ganji, D.** (2016). Investigation of mhd nanofluid flow and heat transfer in a stretching/shrinking convergent/divergent channel considering thermal radiation, *Journal of Molecular Liquids*, *220*, 592–603, doi : 10.1016/j.molliq.2016.05.022.

[73] **Khan, U.**, **Adnan**, **Ahmed, N.**, **Mohyud-Din, S.T.**, **Baleanu, D.**, **Khan, I.**, **and Nisar, K.S.** (2020). A novel hybrid model for cu–al2o3/h2o nanofluid flow and heat transfer in convergent/divergent channels, *Energies*, *13*(7), 1686, doi : 10.3390/en13071686.

[74] **Raptis, A.** (1998). Radiation and free convection flow through a porous medium, *International Communications in Heat and Mass Transfer*, *25* (2), 289–295, doi : 10.1016/s0735-1933(98)00016-5.

[75] **Magyari, E. and Pantokratoras, A.** (2011). Note on the effect of thermal radiation in the linearized rosseland approximation on the heat transfer characteristics of various boundary layer flows,

International Communications in Heat and Mass Transfer, *38*(5), 554–556, doi : 10.1016/j.icheatmasstransfer.2011.03.006.

[76] **Pantokratoras, A. and Fang, T.** (2012). Sakiadis flow with nonlinear rosseland thermal radiation, *Physica Scripta*, *87*(1), 015703, doi : 10.1088/0031-8949/87/01/015703.

[77] **Panton, R.L.** (2024). *Incompressible flow*. John Wiley & Sons.

[78] **Zhang, L.**, **Bhatti, M.M.**, **and Michaelides, E.E.** (2020). Entropy generation in magnetized blood flow through a finite wavy channel under slip conditions, *Journal of Non-Equilibrium Thermodynamics*, *45*(4), 419–429, doi : 10.1515/jnet-2020-0042.

[79] **Akhtar, Y.**, **Ahmad, S.**, **Khalid, F.**, **Junjua, M.u.D.**, **Aryanfar, Y.**, **Hendy, A.S.**, **Tlija, M.**, **and Soliman, A.T.** (2024). Machine learning- a new paradigm in nanoparticle-mediated drug delivery to cancerous tissues through the human cardiovascular system enhanced by magnetic field, *Scientific Reports*, *14*(1), doi : 10.1038/s41598-024-72629-z.

[80] **Roşca, A.V.**, **Roşca, N.C.**, **and Pop, I.** (2020). Mixed convection stagnation point flow of a hybrid nanofluid past a vertical flat plate with a second order velocity model, *International Journal of Numerical Methods for Heat & Fluid Flow*, *31*(1), 75–91.

[81] **Kezzar, M.**, **Ghaffari, A.**, **Dib, A.**, **Usman**, **Sari, M.R.**, **and Muhammad, T.** (2024). Mhd nanofluid flow between porous convergent-divergent channel with velocity slip and nanoparticle aggregation, *Engineering Science and Technology, an International Journal*, *52*, 101679, doi : 10.1016/j.jestch.2024.101679.

[82] **Dinarvand, S.**, **Berrehal, H.**, **Pop, I.**, **and Chamkha, A.J.** (2022). Blood-based hybrid nanofluid flow through converging/diverging channel with multiple slips effect: a development of jeffery-hamel problem, *International Journal of Numerical Methods for Heat & Fluid Flow*, *33* (3), 1144–1160, doi : 10.1108/hff-08-2022-0489.

[83] **Angayarkanni, S. and Philip, J.** (2015). Review on thermal properties of nanofluids: Recent developments, *Advances in Colloid and Interface Science*, *225*, 146–176, doi : 10.1016/j.cis.2015.08.014.

[84] **Sarkar, J.** (2011). A critical review on convective heat transfer correlations of nanofluids, *Renewable and Sustainable Energy Reviews*, *15*(6), 3271–3277, doi : 10.1016/j.rser.2011.04.025.

[85] **Sajid, M.U. and Ali, H.M.** (2018). Thermal conductivity of hybrid nanofluids: A critical review, *International Journal of Heat and Mass Transfer*, *126*, 211–234, doi : 10.1016/j.ijheatmasstransfer.2018.05.021.

[86] **Kleinstreuer, C. and Feng, Y.** (2011). Experimental and theoretical studies of nanofluid thermal conductivity enhancement: a review, *Nanoscale Research Letters*, *6*(1), doi : 10.1186/1556-276x-6-229.

[87] **Hassani, S.**, **Saidur, R.**, **Mekhilef, S.**, **and Hepbasli, A.** (2015). A new correlation for predicting the thermal conductivity of nanofluids; using dimensional analysis, *International Journal of Heat and Mass Transfer*, *90*, 121–130, doi : 10.1016/j.ijheatmasstransfer.2015.06.040.

[88] **Sahoo, R.R. and Kumar, V.** (2020). Development of a new correlation to determine the viscosity of ternary hybrid nanofluid, *International Communications in Heat and Mass Transfer*, *111*, 104451, doi : 10.1016/j.icheatmasstransfer.2019.104451.

[89] **Abbas, M.**, **Khan, N.**, **Hashmi, M.**, **Alotaibi, H.**, **Khan, H.A.**, **Rezapour, S.**, **and Inc, M.** (2024). Importance of thermophoretic particles deposition in ternary hybrid nanofluid with local thermal non-equilibrium conditions: Hamilton–crosser and yamada–ota models, *Case Studies in Thermal Engineering*, *56*, 104229, doi : 10.1016/j.csite.2024.104229.

[90] **Ali, A.**, **Das, S.**, **and Muhammad, T.** (2023). Dynamics of blood conveying copper, gold, and titania nanoparticles through the diverging/converging ciliary micro-vessel: Further analysis of ternary-hybrid nanofluid, *Journal of Molecular Liquids*, *390*, 122959, doi : 10.1016/j.molliq.2023.122959.

[91] **Shahzadi, I.**, **Duraihem, F.Z.**, **Ijaz, S.**, **Raju, C.**, **and Saleem, S.** (2023). Blood stream alternations by mean of electroosmotic forces of fractional ternary nanofluid through the oblique stenosed aneurysmal artery with slip conditions, *International Communications in Heat and Mass Transfer*, *143*, 106679, doi : 10.1016/j.icheatmasstransfer.2023.106679.

[92] **Timofeeva, E.V.**, **Routbort, J.L.**, **and Singh, D.** (2009). Particle shape effects on thermophysical properties of alumina nanofluids, *Journal of Applied Physics*, *106*(1), doi : 10.1063/1.3155999.

[93] **Kierzenka, J. and Shampine, L.F.** (2001). A bvp solver based on residual control and the maltab pse, *ACM Transactions on Mathematical Software*, *27*(3), 299–316, doi : 10.1145/502800.502801.

[94] **Keskin, A.Ü.** (2019). *Boundary Value Problems for Engineers*. Springer.

[95] **Khashi'ie, N.S.**, **Waini, I.**, **Arifin, N.M.**, **and Pop, I.** (2021). Unsteady squeezing flow of cu-al2o3/water hybrid nanofluid in a horizontal channel with magnetic field, *Scientific Reports*, *11*(1), doi : 10.1038/s41598-021-93644-4.

[96] **Shampine, L.F.**, **Gladwell, I.**, **and Thompson, S.** (2003). *Solving ODEs with MATLAB*. Cambridge University Press.

[97] **Siddique, I.**, **Zulqarnain, R.M.**, **Nadeem, M.**, **and Jarad, F.** (2021). Numerical simulation of mhd couette flow of a fuzzy nanofluid through an inclined channel with thermal radiation effect, *Computational Intelligence and Neuroscience*, *2021*(1).

[98] **Jat, K.**, **Sharma, K.**, **Choudhary, P.**, **Soni, P.**, **Ali, R.**, **and Ganesh, M.** (2024). Significance of darcy–forchheimer casson fluid flow past a non-permeable curved stretching sheet with the impacts of heat and mass transfer, *Case Studies in Thermal Engineering*, *61*, 104907, doi : 10.1016/j.csite.2024.104907.

CURRICULUM VITAE

Name SURNAME: Tunahan GÜNAY

EDUCATION:

- **B.Sc.:** 2022, Istanbul Technical University, Faculty of Aeronautics and Astronautics, Department of Aeronautical Engineering

PROFESSIONAL EXPERIENCE AND REWARDS:

- 2023–Present: Research Assistant, Faculty of Aeronautics and Astronautics, Istanbul Technical University
- 2022: Ranked First in the Faculty of Aeronautics and Astronautics, Istanbul Technical University
- 2022: Ranked First in the Aeronautical Engineering Department, Istanbul Technical University

PUBLICATIONS, PRESENTATIONS AND PATENTS ON THE THESIS:

- **Gunay, T.,** Erdem, D., Sahin, A.Z., and Öztop, H.F. (2025). Blood-based non-Newtonian ternary nanofluid flow in converging/diverging channels embedded in a non-Darcy porous medium with slip and jump effects, *International Journal of Numerical Methods for Heat & Fluid Flow,* (under review).
- **Gunay, T.,** Erdem, D., and Sahin, A.Z. (2025). Investigation of temperature jump, first and second-order velocity slip effects on blood-based ternary nanofluid flow in convergent/divergent channels, *International Journal of Numerical Methods for Heat & Fluid Flow,* 35(2), 648–682.

OTHER PUBLICATIONS, PRESENTATIONS AND PATENTS:

- **Gunay, T.,** Gumus, C., and Sahin, A.Z. (2024). The impact of using nanofluid on the performance of solar stills: A comprehensive review, *Process Safety and Environmental Protection,* 189, 1464–1516.